UC San Diego
UC San Diego Electronic Theses and Dissertations

Title

Characterization of the Response of Woven Composites and Additively Manufactured Metals Defects Under Intermediate Loading Rates

Permalink

Author

Buenrostro, Javier

Publication Date

2022

Peer reviewed|Thesis/dissertation

UNIVERSITY OF CALIFORNIA SAN DIEGO

Characterization of the Response of Woven Composites and Additively Manufactured Metals Defects Under Intermediate Loading Rates

A dissertation submitted in partial satisfaction of the
requirements for the degree
Doctor of Philosophy

in

Structural Engineering

by

Javier Buenrostro

Committee in charge:

    Professor Hyonny Kim, Chair
    Professor Jiun-Shyan Chen
    Professor Veronica Eliasson
    Professor Olivia Graeve
    Professor Machel Morrison

2022

The dissertation of Javier Buenrostro is approved, and it is acceptable in quality and form for publication on microfilm and electronically.

University of California San Diego

2022

DEDICATION

I would like to dedicate my doctoral dissertation to my parents. Thank you for your endless love and support. Gracias por todo.

EPIGRAPH

No hay que llegar primero,
pero hay que saber llegar
—Vicente Fernádez

TABLE OF CONTENTS

vii

LIST OF FIGURES

x

xi

LIST OF TABLES

ACKNOWLEDGEMENTS

level of education.

Lastly, I would like to thank my family for the endless support and constant encouragement. Los quiero mucho. Gracias por todo.

TECHNICAL ACKNOWLEDGEMENTS

VITA

2016   B. S. in Structural Engineering, University of California San Diego

2018   M. S. in Structural Engineering, University of California San Diego

2022   Ph. D. in Structural Engineering, University of California San Diego

PUBLICATIONS

Buenrostro, Javier, Kim, Hyonny (2022). Experimental Characterization of the In-Plane Shear Response of Woven Polymer Matrix Composites Under Intermediate Strain Rates. In Proceedings of the American Society for Composites Thirty-Seventh Technical Conference on Composite Materials.

Buenrostro, Javier, Kim, Hyonny, Goldberg, Robert K., Ricks, Trenton M. (2021). Hybrid Experimental and Numerical Characterization of the 3D Response of Woven Polymer Matrix Composites. In Proceedings of the American Society for Composites Thirty-Sixth Technical Conference on Composite Materials.

Jackson, Karen E., Goldberg , Robert K., Ricks, Trenton M., Haluza, Rudy T., Buenrostro, Javier, "Application of a Developmental Composite Material Model to Predict the Crush Response of Two Energy Absorbers", *NASA TM*,

ABSTRACT OF THE DISSERTATION

Characterization of the Response of Woven Composites and Additively Manufactured Metals Defects Under Intermediate Loading Rates

by

Javier Buenrostro

Doctor of Philosophy in Structural Engineering

University of California San Diego, 2022

Professor Hyonny Kim, Chair

The increased used of complex geometries in aerospace and automotive applications has been possible due to recent advancements in material manufacturing methods. Materials such as woven polymer matrix composites and additively manufactured (AM) metals offer benefits in weight and part reduction compared to traditional aerospace materials. The need for the experimental and numerical characterization of the nonlinear behavior in advanced composites and defects in laser powder bed fusion (LPBF) metals under intermediate loading rate is needed to better use such materials in aerospace and automotive applications which are subjected to impact or crash events. The establishment of comprehensive material databases is both

labor intensive and costly. The need for an efficient methodology to characterize the rate-dependent behavior is therefore needed.

To address this problem, experimental characterization of the in-plane shear response of two balanced plain weave carbon fiber composites is studied using test methods based on a v-notch shear specimen and a shear fixture designed using a combination of the ASTM D7078M and a modified Arcan fixture. Additionally, specimen preparation for digital image correlation (DIC) with Phantom high speed cameras is discussed. Results from 2D DIC and measured force values are used to obtain experimental stress-strain curves. Comparison between quasi-static and intermediate rates mechanical behavior show increase in strength and modulus for both plain weave carbon fabrics.

Additionally, a hybrid experimental and numerical characterization methodology is developed for woven polymer matrix composites that uses models from Micromechanics Analysis Code with Generalized Method of Cells (MAC/GMC) with experimental stress-strain curves. Validation of this methodology is performed through coupon verification in finite element analysis (FEA) software LS-DYNA for two woven materials using a tabular plasticity material model, MAT213. Additionally, validation studies of an adhesively bonded composite wingbox structure subjected low velocity impact is simulated and compared with experimental tests.

Lastly, experimental investigation of the combined effects of heat treatment on AM steel metals with fusion defects is performed through uniaxial tension experiments at various loading rates. High-speed camera images of mechanical tests seek to determine how heat treatment affects the material response and failure. Optical microscopy images are used to observe the failure mechanisms of specimens with internal defects.

Chapter 1

Introduction

1.1   Motivation

Advanced composite materials have grown increasingly popular in aerospace and automotive industries. This is because composites allow for a decrease in the structural weight while increasing the stiffness and strength. Many applications that were previously reserved for metals are now being replaced by composite materials. Composites allow for complex geometry and reduction of parts needed to assemble structures. Similarily, another manufacturing method that is seeing increasing use is laser powder bed fusion (LPBF) additive manufacturing. This technology can achieve highly complex metallic parts without part-specific tooling by using the fast-moving high energy laser beam to selectively fuse metal powders layer by layer [1]. They are increasingly being used in aerospace and biomedical industries. The need for systematic understanding of processing effects and loading rates on material response of AM metals is of interest to understand process induced defects and the effect that processing parameters such as secondary heat treatment have on fusion defects.

Existing composite material databases such as those created through NCAMP,

the National Center for Advanced Materials Performance, which works with the Federal Aviation Administraion (FAA) and industry partners to qualify material systems and populate a shared materials database that can be viewed publicly provide pointwise material properties. Issues with the current material models used for simulating the impact response of composite materials is that many of them are limited to use with two-dimensional shell elements, where the through thickness response of the material under impact is often significant. To begin to address these major issues, a new composite material model for use in LS-DYNA has been developed and implemented by groups from both industry and academia [2, 3]. In this model, the input consists of material stress-strain curves in the various normal and shear coordinate directions. This approach ensures that the full material response, including nonlinearities in the stress-strain behavior, will be appropriately captured.

Applications and characterization of MAT213 include ballistic impact and low-velocity crush of unidirectional composites [2, 4]. Studies using MAT213 have used full sets [2, 4] of data, legacy data sets [5] sparse hybrid data sets [6] for a unidirectional composite, T800/F3900. Previous experimental characterization and applications of MAT213 have focused on unidirectional thermoset composite materials. With the desire to also analyze woven fabric composite materials, new problems can arise and require experimental and numerical investigation in order to expand the range of applicability of MAT213 to fabric composites in aerospace structures.

1.2 Objectives

The objectives of this research is to provide experimental techniques to extract rate-dependent inputs for tabulated material models. This research focuses on experimental coupon studies of woven polymer matrix composites and additively manufactured metals under intermediate loading rates. Additionally, this work aims to develop a hybrid experimental-numerical methodology to efficiently characterize the

rate-dependent stress-strain curves of new materials for State of the Art in composite material model, MAT213. MAT213 has been experimentally characterized and modeled with finite element method (FEM) using a unidirectional polymer matrix composite with both solid and shell elements. For fabrics it has been applied using shell elements using legacy material databases [5]. To validate this methodology by investigation two weave architectures and fiber volume fractions.

1.3   Literature Review

1.3.1   Characterization of Woven Composite Materials

Composite materials are heterogeneous materials that typically consist of a reinforcing fiber and binding matrix. The damage initiation and evolution of these materials are architecture dependent. Where the response of the composite with different reinforcement or matrix can cause brittle or ductile response. Another classification of composites is based on the reinforcing material such as discontinuous, continuous fibers, and wovens [7]. Additionally, response of the composite material is dependent on the constituents and exhibit mechanics properties that are directional dependent.

Woven composite materials offer increased tailor-ability and drapability. Weaves are made by interlacing two or more orthogonal sets of yarns on a loom [8]. Weaves are classified by the pattern of interlacing with common 2D orthogonal weaves used for polymer matrix composites such as plain, twill and satin weaves [8] Important properties to consider when using 2D weaves include tow size, yarn paths, cross-sectional shapes, pattern, and cross over points[8].

Generally, effective material properties of a composite material are obtain using standardized tests. ASTM D3039 [9] gives guidelines on testing composite laminates in tension to obtain effective modulus, tensile strength and Poisson's ratio. ASTM

D3410 [10] and D695M [11] provide guidelines for compression testing. Issues with using D695M are that two separate specimens are required, a tabbed specimen to obtain the strength and untabbed specimen to obtain modulus. This makes it difficult to model and obtain experimental stress-strain curves from a single specimen. For shear, tests such as the ASTM D5379, ASTM D7078M, and ASTM D3518 are used to determine shear stress-strain response.

Digital Image Correlation (DIC), a popular experimental method for mechanical strain measurement from quasi-static to high strain rate [2, 12, 13, 14, 15], has been used to obtain experimental stress-strain curves for MAT213. The benefits of using DIC over traditional methods such as strain gages are that measurements are noncontact and full field. This is very important when taking measurements of textile or woven materials since local stain variations can exist at length scales smaller than the gages. Setup for 2D-DIC only requires white light and a camera, while 3D DIC requires two cameras. DIC has been used to characterize the in-plane response and found non-homogeneous strain fields and out-of-plane displacements of triaxially braided textile materials [13, 16].

Modeling of the constitutive response of woven composites can be done with varying levels of fidelity, as shown in Figure 1.1. Explicitly modeling the individual fibers is computationally expensive, especially, if trying to model large scale structures. Micromecahnics approaches that used detailed computed tomography (CT) data have been used to model the representative volumetric (RVE) or repeating unit cell (RUC) of woven composites [17]. It is computationally expensive to simulate each individual fiber, therefore, homogenization of tows is commonly done to efficiently model the homogenized tow geometry and allow for interaction with matrix. Computer design tools such as TexGen and WiseTex generate weave geometry patterns generation for use in FEA software such as Abaqus [18, 19]. These meso-scale structures can be analyzed using FEA with period boundary condition(PBC) definitions. Multiscale approaches use homogenized meso-scale geometric parameters to incorporated weave

geometric structure while while reducing the computational cost of modeling such as Generalized Method of Cells (GMC), a 3D micromechanics framework, commonly used for woven and textile composite materials that have a periodic structure [7]. Multi-scale modeling approaches have used these subcell-based approaches to model unidirectional, woven and triaxially braided composites to look at effects caused by matrix nonlinearities and fiber tow architectures [20, 21, 22].

Additionally, composites can be modeled using a smeared homogeneous approach that treats the material at the macro-scale as a single continuum, whereas, micromechanics approaches treat the tows and matrix as separate continuum. Classical Laminate Plate Theory (CLPT) is used to describe the laminate response of homogeneous anisotropic materials, which works well for the elastic response of unidirectional composites with ply orientations [23]. Simple methods of modeling the weave by neglecting the continuity of the fibers and using an assembly of cross plies based on CLPT commonly is referred to as the mosaic model [24]. These are computationally efficient, however, do not include microstructual parameter undulation angle that are present in woven materials. Expansion of the mosaic model was extended to include the undulation angle, also referred to as crimp angle using the Bridging model for satin weaves [24].

Progressive damage modeling of composites involves constitutive laws combined with continuum damage mechanics to match the experimental response in both fiber and matrix-dominated material directions. In finite element softwares such as Abaqus or LS-DYNA progressive damage models commonly use elastic orthotropic continua with different failure criteria for damage initiation such as Hashin, Chang-Chang, or Tsai-Wu [25, 26]. To model the tensile response of composites along the fiber direction, elastic constitutive equations are sufficient due to the brittle behavior of the fibers. However, when loaded in a matrix-dominated loading direction such as shear or compression, nonlinear constitutive models are needed. Material nonlinearity has been used in constitutive laws that describe the deformation, damage
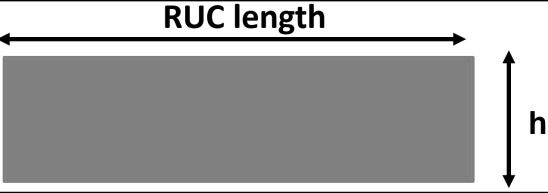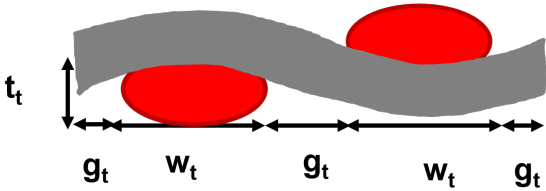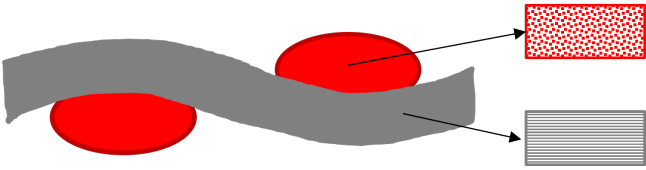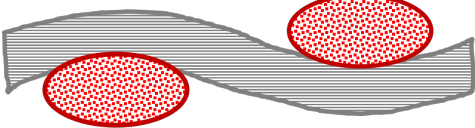
Fully Homogenized Weave	RUC length h
Homogenized Fiber Tows Weave	t_t g_t w_t g_t w_t g_t
Multi-scale Weave	
Explicit Microstructure Weave	

Figure 1.1: Weave modeling techniques. Where t_t is the tow thickness, g_t is the tow gap and h is the weave thickness. Adapted from [21].

and failure mechanics to model composites under high strain rate or high temperature applications [7].

The Tsai-Wu failure criterion allows one to model failure in anisotropic composite materials with different strengths in tension and compression. It is a popular stress-based failure criterion and describes a surface in the six-dimensional stress space based upon the input of failure stresses in the principle material directions and follows the general form [27]

$$
1 = \begin{pmatrix} F_1 \\ F_2 \\ F_3 \\ F_4 \\ F_5 \\ F_6 \end{pmatrix}^T \begin{pmatrix} \sigma_{11} \\ \sigma_{22} \\ \sigma_{33} \\ \sigma_{12} \\ \sigma_{23} \\ \sigma_{13} \end{pmatrix} + \begin{pmatrix} \sigma_{11} \\ \sigma_{22} \\ \sigma_{33} \\ \sigma_{12} \\ \sigma_{23} \\ \sigma_{31} \end{pmatrix}^T \begin{bmatrix} F_{11} & F_{12} & F_{13} & F_{14} & F_{15} & F_{16} \\ F_{21} & F_{22} & F_{23} & F_{24} & F_{25} & F_{26} \\ F_{31} & F_{32} & F_{33} & F_{34} & F_{35} & F_{36} \\ F_{41} & F_{42} & F_{43} & F_{44} & F_{45} & F_{46} \\ F_{51} & F_{52} & F_{53} & F_{54} & F_{55} & F_{56} \\ F_{61} & F_{62} & F_{63} & F_{64} & F_{65} & F_{66} \end{bmatrix} \begin{pmatrix} \sigma_{11} \\ \sigma_{22} \\ \sigma_{33} \\ \sigma_{12} \\ \sigma_{23} \\ \sigma_{31} \end{pmatrix} \tag{1.1}
$$

where the linear stress term, σ_{ij}, takes into account the differences between positive and negative failure stress, while the quadratic stress terms, $\sigma_{ij}\sigma_{ij}$, describe an ellipsoid in stress space [27].

Delamination is a common damage mechanism that occurs within composite laminates. The initiation and growth may occur during regular maintenance at low velocities or at high velocities which can lead failure. Delamination is typically modeled using fracture mechanics methods such as virtual crack VCTT, J-integral and cohesive zone method to characterized the response [28, 29]. Delamination is experimentally characterized using double cantilever beam (DBC) and end-notched flexure (ENF) mechanical tests following ASTM standards ASTM D5528-13 and D7905 [30, 31], respectively. A "pre-crack" or "starter crack" is a manufactured defect used in these standards to help with crack initiation and growth which work well for continuous laminated composites. In reality, delamintaion in structures is not purely mode I or mode II, but instead are a mixture of modes. Specimens that

are used to characteriztion the mix mode behavior include crack lap shear, edge delamination tension, Arcan, asymmetric DCB, and mixed mode bending [32, 33].

1.3.2 Laser Powder Bed Fusion Materials

Additive manufacturing (AM), in particular laser powder bed fusion (LPBF) has grown increasingly popular for building of complex parts used in aerospace engines, space structures and human implants. AM is defined as a process of joining materials to make parts from 3D model data, usually layer upon layer, as opposed to subtractive manufacturing and formative manufacturing methodologies [34]. LPBF is an additive manufacturing process that consists of thermally bonding selective regions of compacted mixed powders, ASTM F2792 [1]. LPBF builds layer by layer using a thermal energy source, typically a laser or electron beam, to selectively sinter or melt a thin layer of powder to the build plate in an enclosed chamber with argon or nitrogen gas, to avoid surface oxidization [35]. Benefits of using LPBF over traditional manufacturing methods in metallurgy such as cast and forging is that no molds are need and significantly less material is wasted due to machining. Typical powders used in metal LPBF consist of mixing of different elements such iron, nickel, chromium, and molybdenum. In addition to elements, binding materials and lubricants are added to help with part building. The typical size of the metal powders for LPBF metals is 30 μm [36]. Despite advances in AM technologies, the lack of process repeatability and stability remain an issue. Common defects in LPBF include porosity, balling, surface defects, residual stresses, microstructural impurities, and geometric defects [35]. There are no standard methods for characterization of these materials which means that material properties can vary depending on machine, manufacturing parameters and powders.

Porosity is important because it has significant effect on the formation of cracks and mechanical properties [37]. Process parameters such as laser power, scan speed

and scan spacing have been observed to affect the porosity in LPBF [38]. Low laser power causes the formation of droplets and bad connection between substrates, whereas too high laser power causes distortions and irregularities that appear due to big melt pool volumes and recoil pressure aspects [38]. The development of pores is also influenced by the scan speed in which faster scan speeds leads a short time between melting and solidification of the powders and this allows for less gas being trapped to form pores [39]. Slower scan speeds increase the time between melting and solidification. To improve the porosity, heat treatment (HT) of the build part has been performed to reduce porosity [35]. Characterization of LPBF is done using scanning electron microscopes (SEM) to give insight into the microstructure grain boundaries [40, 41, 42]. Additionally, as build AM parts usually have rough surfaces and include support material that is used to build parts. Machining is often needed to obtain final part finished geometry.

In-situ monitoring of the AM process has been seen to give insight into residual stresses that develop due to temperature or profile tracking using imaging and thermal image [35]. Due to the high energy and rapid cooling, LPBF AM parts develop residual stresses due to large thermal gradients near the laser spot [43]. In Wu et al. [42], DIC was used to quantitatively measure surface-level residual stresses which was used in conjunction with neutron diffraction to asses the effects of scanning pattern, laser power and scan speed on 316L stainless steel manufactured using LPBF. DIC has also been used to measure mechanical response of metals to characterize the response ranging from quasi-static to dynamic high strains [44].

1.3.3   Dynamic Testing at Intermediate Loading Rates

Material characterization techniques depend on the desired strain rates where servohydraulic and screw machines are used to obtain material responses at $10^{-4}\text{s}^{-1}-10^{-1}\text{s}^{-1}$, Figure 1.2 [44, 45].

9
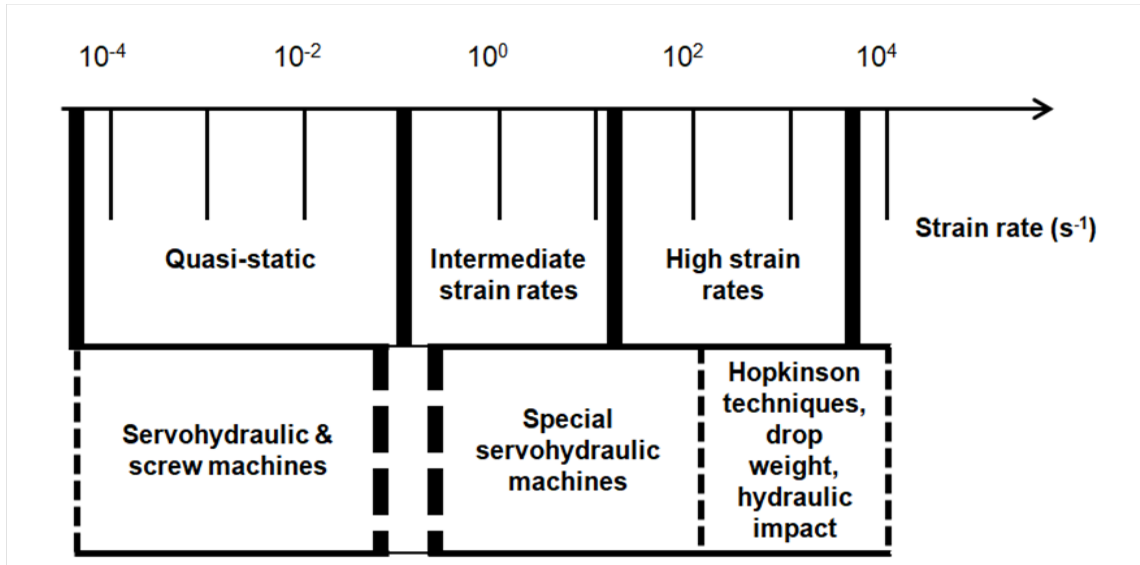
Figure 1.2: Dynamic testing testing techniques at various strain rates. Adapted from
[45, 46]

Similarities between composites and AM metals is that they are dependent on the
manufacturing process. Properties of composites can vary depending on the manu-
facturing process. Manufacturing of pre-impregnated (prepreg) composites produce
better quality parts with higher fiber volume fractions compared to manual "wet"
layup techniques. The mechanical response of composite materials is more complex
than metals or rubber due to its heterogeneous microstructure and anisotropy mak-
ing its behavior unique to the loading direction. Additionally, the repeating unit cell
(RUC) architecture needs to be considered for woven and textile composites [47].
At high speeds the matrix dominates the behavior of the composite and viscoplastic
phenomena become important [48]. Previous work on the strain rate sensitivity of
epoxy resin in tension and shear under quasi-static and high strain rates has shown
that the response of resins in tension transition from ductile to brittle between low
and intermediate rates, while in shear the resin response remains ductile for all rates
[48]. Experimental data at high strain rates can be adapted to advanced polymer

viscoplastic constitutive models that capture the physical phenomenon which occur at high strain rates [49]. In combination with the viscoplastic matrix modeling the mechanical properties of the composite laminate can be iteratively matched with the experimentally measured response using micromechanics analysis [50].

In polymer matrix composites the tensile and compressive loading response in the fiber direction remains linear with negligible plasticity [51]. However, in transverse compression or shear the mechanical response is known to behave nonlinearly and inelasticly [23]. The experimental methodology needed to characterize the viscoplastic behavior of polymer matrix composites is difficult to achieve due to the high manufacturing and labor costs. To efficiently capture the material response, Vogner and Kyriakides [52] developed a biaxial test system with a hydraulic actuator to facilitate combined transverse compression and shear of a unidirectional AS4/PEEK for 10^{-5}s^{-1} to 10^{-1}s^{-1} strain rates to capture the nonlinear and rate dependent response. Similarly, Koerber et al [53] looked at the transverse compression and in-plane shear of IM7/8552 unidirectional carbon/epoxy, using a servo hydraulic test machine for quasi-static rates and Split Hopkinson Bar (SHB) for high rates. In the work of Fitoussi, [54] an optimized experimental methodology was developed for a sheet moulding compound (SMC) and a carbon/epoxy woven laminate using servo-hydraulic testing for moderate strain rates. This procedure aimed to optimized and isolate the inertial effects that are attributed to the testing machine. However, to accurately predict the response of PMC under intermediate loading conditions one cannot always capture the rate effect. Machine limitations govern the max speeds load frame can achieve.

Typically, servo hydraulic load frame machines are used to characterize the mechanical behavior of polymer matrix composites at quasi-static loading. Under high-speed loading issues arise due to inertia and damping effects that are associated with the testing machine. To obtain mechanical properties of materials at any rates higher than quasi-static, dynamic tests are needed. These tests are typically done

using Hopkinson pressure bars to record the dynamic compression stress-strain response of materials [55, 56, 57]. The benefit of using a Hopkinson Bar becomes apparent when strain rates are high enough that inertia effects are non-negligible. The Hopkinson Bar technique is a well established method for determining material properties of rubbers, plastics, metals, rocks, and adhesive joints [44, 45, 58, 59]. Measurements are achieved using strain gages typically applied on rods to measure the force the bar which the specimen is loaded with.

While the measured response of PMC at high strain rates has been achieved primarily on unidirectional composites, the meso-scale behavior of woven materials is not widely available. The macro-mechanical response of triaxially braided composites under shear, tension and compression were investigated [13, 60]. Variation in the fiber architecture length scale affects the coupon size particularly for material systems with large tow sizes and thus large repeating unit cells (RUCs). The shear response in woven polymer matrix composites in literature has shown inconsistencies [46]. Variations in test methods and specimen design contribute to the inconsistency. ASTM D3510 is a popular standard method due to its simple geometry to determine an in-plane shear property by using +/- 45 degree off-axis specimens loaded in tension to measure axial and transverse strain which is then used to calculate engineering shear stress vs. shear strain. In Brown et al [61], characterization of the rate response in E-glass/polypropylene composites were investigated following specimens from ASTM D3510 combined with a drop weight tower. The study found an increase in the shear strength with a decrease in shear modulus. Drawbacks with off-axis specimens are non-uniform states of shear stress that develop and specimens can be susceptible to buckling in compression.

Other popular shear tests include ASTM D5379 Iosipescu beam [62], ASTM D7078M v-notched rail shear [63] and Arcan shear fixtures [64, 65, 66]. Benefits of using notched specimens are that it allows for stress localization which helps to avoid failure in the gripping areas. Additionally, v-notch rail fixtures have a large notched

width which is important to capture the macro-scale response of woven materials that have wide tows. Disadvantages with the fixtures used in Iosipescu and rail shear are that at higher loading rates the mass of the fixture plays an important factor and would require large energy to achieve higher loading rates. Special actuators are needed to be able to produce fast enough stroke rates using ASTM 7078M fixture [54]. Benefits of using Arcan fixtures compared to standard v-notch fixtures is that it allows for biaxial states of stress to be produced uniform tension or combined shear loadings. Various designs exist for Arcan with less bulky modified Arcan fixtures that allows the possibly to run experiments at faster loading rates [65].

1.4 Novel Contribution

Previous experimental and numerical works for Tabulated Orthotropic Composite Plasticity, MAT213, have focused on a uni-directional fiber architecture, specifically T700/F3900[3, 2]. Challenges with characterization of the full range of dynamic experiments is that it is labor intensive and costly. Additional challenges with woven composite, is that the experimental characterization of the dynamic response is dependent on the specimen design in which specimen geometry and testing method need to be considered. What has not been done is the experimental characterization and modeling woven fiber architecture composites using rate dependent data for MAT213. This work will provide experimental and numerical techniques and methodology to define rate dependent inputs for MAT213. This work also contributes to the understanding of MAT213 capabilities to model woven materials. The following methodology to validate MAT213 as a suitable material model for low-velocity impact of adhesive bonded composite structures. A combination of experimental and numerical stress-strain curves are used to generate input to MAT213 which is then verified through single element and mulit-element coupon simulations. Validation of methodology for low-velocity impact is then performed using a pendulum impactor to induce damage into an adhesively bonded rectangular composite wing-box. Lastly, validation of material characterization methodology for woven composites is performed by characterization of an additional woven composite.

Chapter 2

Background

2.1 Digital Image Correlation

DIC is a popular and flexible experimental technique that measures full-field surface displacements using a sequence of captured images. DIC calculates displacements and strains by comparing digital images captured before deformation (reference) and after deformation. Important applications of DIC include model validation and material identification [67]. Advantages of DIC include simple setup and specimen preparation, an environment that only requires white or natural light, and a wide range of measurement sensitivity and resolution. 2D DIC only requires one fixed camera and is limited to in-plane measurements on flat surfaces. For curved specimens, 2D DIC is not recommended due to large out of plane errors [68] and 3D DIC is needed. 3D DIC requires two cameras that are used for stereovision. Background for 2D DIC is summarized below and a comprehensive review of DIC can be found in [15, 69].

DIC analysis is dependent on the quality of speckles, camera lighting, and camera resolution. To create these speckles, typically, a white base coat is first applied to the surface of the specimen. In thid study surface preparation is done using fine

grit sandpaper followed by cleaning with isoproplyn before applying the white paint. It is desirable to have randomly distributed speckles 3-7 pixels in size [68]. There are various ways to obtain speckle sizes from spray paint cans, sharpie "dots", or airbrush. It is preferred to have speckles that are roughly the same size to avoid aliasing. Example speckles sizes for these various techniques are shown in the Figure 2.1.

(a)   (b)
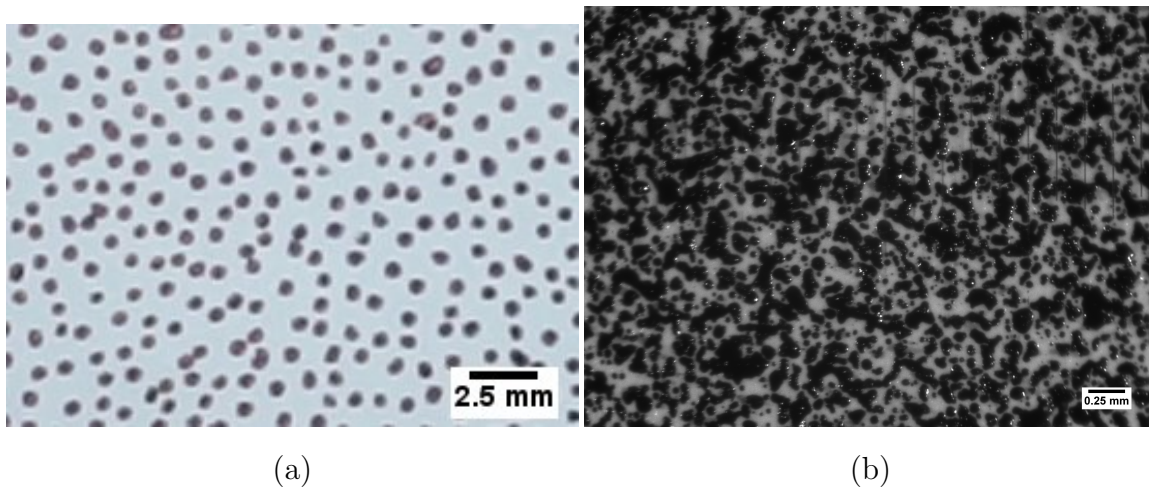
Figure 2.1: Speckle types using (a) a Sharpie marker pen (b) an airbrush with a 0.3 mm nozzle.

These images are processed through a DIC algorithm that determines displacements by correlating subsets of the undeformed reference image with the deformed images as illustrated in Figure 2.2a. This standard DIC approach is acceptable when displacements are small and not much material plasticity is observed. For large displacements, incremental DIC is used in which the the DIC algorithm correlates two subsequent images and adds any previous calculated displacements. Better correlation can be achieved when using incremental DIC for large deformation problems, however, it should be noted that there is higher inherent error when using incremental

16

compared to standard DIC, since errors accumulate at every correlation step.

DIC uses the pixel intensities to calculate displacements. An assumption in DIC is that pixel intensities, $g(x, y)$ and $f(x, y)$, from the target picture and the corresponding reference picture are approximately equal, Equation 2.1

$$g(x, y) = f(x + u, y + v). \tag{2.1}$$

DIC softwares look for a group of neighboring pixels called a subset or facet. It is desirable that these subsets be unique to improve correlation. Hence why speckles need to have a random pattern. The size of the subset is defined by the quality and size of the speckle pattern. The minimum number of pixels in a speckle needed to avoided aliasing is 3 [70]. The lower limit of the subset is determined by both the camera resolution and speckle size. Speckles should be non-repetitive, isotropic and high contract. Additionally, since images are discrete, reconstruction of subset information is done through interpolation functions to obtain continuous functions within the subset. To ensure a continuous displacement field across the DIC area of interest (AOI) shape functions for displacement fields, μ and ν, are assigned to each subset. These shape functions are functions of x and y pixel locations and s is a vector which maps deformed and undeformed shapes. The shape functions for a sum of squared differences (SSD) correlation function are shown in Equation 2.2. Where the first two terms in Equation 2.2 corresponds to the rigid body translation and the remaining terms correspond to the complex deformaion fields. Removing rigid body displacements is necessary for using DIC displacement calculations, however, when calculating strain, rigid body translations are naturally removed.

$$\begin{bmatrix} \mu(x, y, s) \\ \nu(x, y, s) \end{bmatrix} = \begin{bmatrix} x \\ y \end{bmatrix} + \begin{bmatrix} u \\ v \end{bmatrix} + \begin{bmatrix} \frac{\partial u}{\partial x} & \frac{\partial u}{\partial y} \\ \frac{\partial v}{\partial x} & \frac{\partial v}{\partial y} \end{bmatrix} \begin{bmatrix} \Delta x \\ \Delta y \end{bmatrix} + \begin{bmatrix} \frac{\partial^2 u}{\partial x \partial y} \\ \frac{\partial^2 v}{\partial x \partial y} \end{bmatrix} \Delta x \Delta y + \\ \begin{bmatrix} \frac{\partial^2 u}{\partial^2 lx} & \frac{\partial^2 u}{\partial^2 ly} \\ \frac{\partial^2 v}{\partial^2 lx} & \frac{\partial^2 v}{\partial^2 ly} \end{bmatrix} \begin{bmatrix} (\Delta x)^2 \\ (\Delta y)^2 \end{bmatrix} \tag{2.2}$$

17
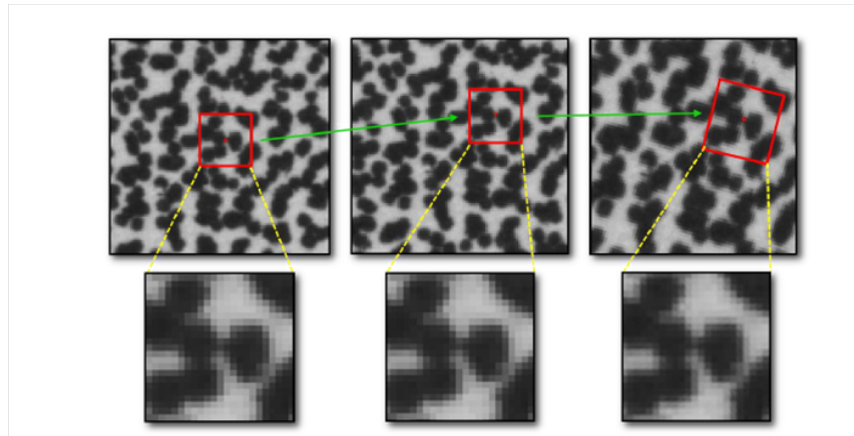
(a)
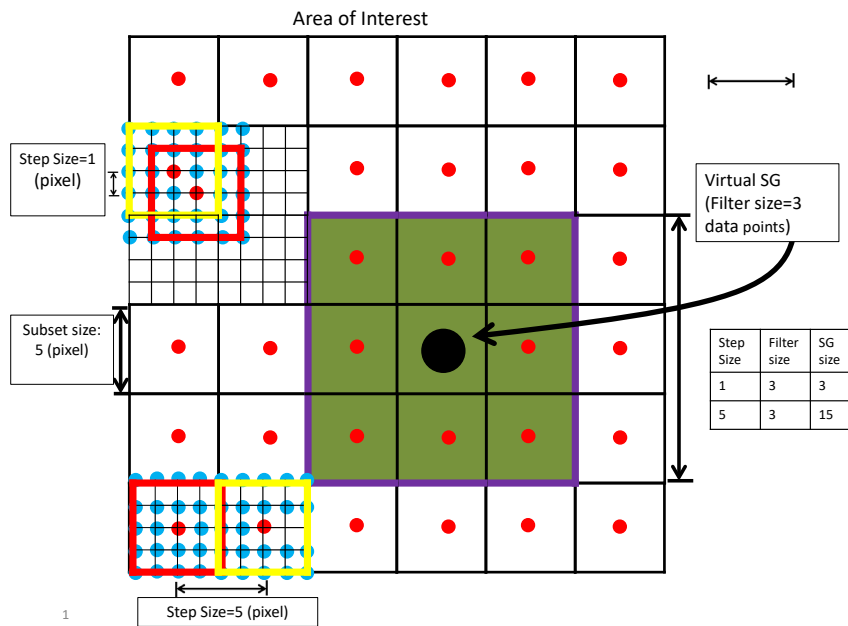
(b)

Figure 2.2: Digital image correlation principles of (a) subset displacement tracking, used in Correlated Solutions and (b) virtual strain gage size example calcaulation showing pixels as blue dots, subset centers as red dots, subset regions in red rectangles, virtual strain gage in purple rectangles, and step size in yellow rectangles [71].

Correlation functions that are used to compared deformed images calculate a correlation coefficient. When this coefficient is high, correlated subsets match each other. While a low correlation coefficient means that the subsets are dissimilar. A simple correlation function is the sum square differences (SSD) as shown in Equation 2.3

$$\chi^2 = \sum_i (G_i - F_i)^2. \tag{2.3}$$

Here χ is the function to minimize and i is the pixel in the subset. The correlation coefficient is given as $1 - \chi^2$ which is a percentage. F and G are the reference and deformed images, respectively.

More robust correlation functions that takes into account image contrast differences include the normalized sum of squared differences (NSSD) and zero normalized sum of squared differences (ZNSSD). For small shifts in the image NSSD will result in lower correlation coefficients. When using ZNSSD results will be the same even if there is a shift or a difference of contrast between images during the tests by compensating for the average grey values within the subset. The ZNSSD correlation function is shown in Equation 2.4

$$\chi^2 = \sum_i \left[\frac{\sum \bar{F}_i \bar{G}_i}{\sum \bar{G}_i^2} G_i - \bar{G}_i \frac{\sum \bar{F}_i \bar{G}_i}{\sum \bar{G}_i^2} - \left(F_i - \bar{F} \right) \right], \tag{2.4}$$

where,

$$\bar{F} = \frac{\sum_i^n F_i}{n} \text{and } \bar{G} = \frac{\sum_i^n G_i}{n}. \tag{2.5}$$

Lastly, to obtain strains from DIC displacement data an additional step is needed to calculate strain which uses the spatial derivative of a collection of displacement data points. The area of a given strain point in DIC is called the virtual strain gage (VSG) which is a function of the subset size, step size and number of data points used in the strain window. The size of the VSG can be calculated using Equation 2.6 [72]. Since strain is calculated by takuing the derivative of the displacement data,

19

there are increased computational errors and noise that arise. Increasing the strain filter results in a smoother strain fields at the cost of lower resolution [72].

$$\text{VSG} = [(\text{Strain Window} - 1) \times \text{Step}] + \text{Subset} \qquad (2.6)$$

For the experiments presented in this dissertation, VIC 2D-6 software, which is commercially available and developed by Correlated Solutions, was used for all analysis.

2.2   Generalized Method of Cells

Method of cells (MOC) was originally developed to model fiber reinforced composites having double and triple periodicity. MOC uses subcell kinematics formulations to derive the continuum stress-strain response as opposed to micromechnics models that rely on empirical assumptions for the stress strain relation. A common representation of a fiber reinforced composite is using a 2 by 2 rectangular repeating unit cell (RUC) with the fiber shown in which is used as the building block which the continuum response of the entire period material can be constructed [7]. Restrictions of MOC are that only rectangular arrays with at most two different fiber spacings can be analyzed and the use of an RUC with only four subcells precludes the possibility of including inter-facial regions between the fiber and matrix phase, as well as the consideration of complex fiber shapes or fiber architectures[7].

Generalized MOC (GMC) eliminates these restrictions by employing an RUC that can be divided into an arbitrary number of subcells for multiphase periodic materials. Static equilibrium of the materials in the subcells is required to ensure that continuity of displacements and tractions between neighboring subcells within the RUC, as well as neighboring RUCs, is satisfied on an average basis. $(\mathbf{x}) = (x_1, x_2, x_3)$, is the center location of a subcell with respect to the fixed global coordinate. The local coordinate system, $\bar{x}_1^{(\alpha)}, \bar{x}_2^{(\beta)}$, and $\bar{x}_3^{(\gamma)})$ are introduced, whose origin is located at the center of

each subcell $(\alpha\beta\gamma)$. The neighboring coordinates $(\hat{\alpha}\beta\gamma)$ in the x_1-direction, where $\hat{\alpha}$ is defined to have the following form:

$$\hat{\alpha} = \begin{cases} \alpha + 1 & \alpha < N_\alpha \\ 1 & \alpha = N_\alpha \end{cases} \tag{2.7}$$

This ensures that for $\alpha < N_\alpha$ that the neighboring subcell in the x_1-direction is labeled $(\alpha + 1, \beta, \gamma)$ within the RUC, whereas for $(\alpha = N_\alpha)$ the neighboring subcell is within the next RUC, whose subcell is labeled $(1, \beta, \gamma)$. Similarly, $\hat{\beta}$ and $\hat{\gamma}$ are defined:

$$\hat{\beta} = \begin{cases} \beta + 1 & \beta < N_\beta \\ 1 & \beta = N_\beta \end{cases} \tag{2.8}$$

$$\hat{\gamma} = \begin{cases} \gamma + 1 & \gamma < N_\gamma \\ 1 & \gamma = N_\gamma \end{cases} \tag{2.9}$$

GMC uses a linear expansion of displacements at each subcell which is described as follows

$$u_i^{\beta\gamma} = w_i^{\alpha\beta\gamma}(\mathbf{x}) + \bar{x}_1^{(\alpha)}\phi_i^{\alpha\beta\gamma} + \bar{x}_2^{(\beta)}\chi_i^{\alpha\beta\gamma} + \bar{x}_3^{(\gamma)}\psi_i^{\alpha\beta\gamma} \; i = 1, 2, 3 \tag{2.10}$$

where $w_i^{\alpha\beta\gamma}$ are the displacement at the center of the of the subcell and $\phi_i^{\alpha\beta\gamma}$, $\chi_i^{\alpha\beta\gamma}$, $\psi_i^{\alpha\beta\gamma}$ are the microvariables for the first order expansion about the local coordinates. Infinitesimal strain theory is used to relate the small strain tensor to the displacement field by

$$\varepsilon_{ij}^{(\alpha\beta\gamma)} = \frac{1}{2}(\partial_i u_j^{(\alpha\beta\gamma)} + \partial_j u_i^{(\alpha\beta\gamma)}) \; i, j = 1, 2, 3 \tag{2.11}$$

Where $\partial_1 = \partial/\partial\bar{x}_1^{(\alpha)}$, $\partial_2 = \partial/\partial\bar{x}_2^{(\beta)}$, and $\partial_3 = \partial/\partial\bar{x}_3^{(\gamma)}$.

Therefore, each strain component can be computed in terms of the micro-variables. Due to the first order expansion of the displacement field the strain in the subcell is constant, which is referred to as the average strains. To solve for the micro-variables, a set of inter-facial boundary conditions for continuity of traction and displacement must be established. For each subcell the neighboring subcell must have an equivalent set of displacement components at the interface,

$$
\begin{aligned}
\bar{\varepsilon}_{11}^{(\alpha\beta\gamma)} &= \phi_1^{(\alpha\beta\gamma)} \\
\bar{\varepsilon}_{22}^{(\alpha\beta\gamma)} &= \chi_2^{(\alpha\beta\gamma)} \\
\bar{\varepsilon}_{33}^{(\alpha\beta\gamma)} &= \psi_3^{(\alpha\beta\gamma)} \\
\bar{\gamma}_{23}^{(\alpha\beta\gamma)} &= 2\bar{\varepsilon}_{23}^{(\alpha\beta\gamma)} = \chi_3^{(\alpha\beta\gamma)} + \psi_2^{(\alpha\beta\gamma)} \\
\bar{\gamma}_{13}^{(\alpha\beta\gamma)} &= 2\bar{\varepsilon}_{13}^{(\alpha\beta\gamma)} = \phi_3^{(\alpha\beta\gamma)} + \psi_1^{(\alpha\beta\gamma)} \\
\bar{\gamma}_{12}^{(\alpha\beta\gamma)} &= 2\bar{\varepsilon}_{12}^{(\alpha\beta\gamma)} = \phi_2^{(\alpha\beta\gamma)} + \chi_2^{(\alpha\beta\gamma)}.
\end{aligned}
\tag{2.12}
$$

Thus, the average strains and stresses in the composites RUC can be written as

$$
\bar{\varepsilon}_{ij} = \frac{1}{d}\frac{1}{h}\frac{1}{l} \sum_{\alpha=1}^{n_\alpha} \sum_{\beta=1}^{n_\beta} \sum_{\gamma=1}^{n_\gamma} \varepsilon_{ij}^{(\alpha\beta\gamma)} d_\alpha h_\beta l_\gamma
\tag{2.13}
$$

$$
\bar{\sigma}_{ij} = \frac{1}{d}\frac{1}{h}\frac{1}{l} \sum_{\alpha=1}^{n_\alpha} \sum_{\beta=1}^{n_\beta} \sum_{\gamma=1}^{n_\gamma} \sigma_{ij}^{(\alpha\beta\gamma)} d_\alpha h_\beta l_\gamma
\tag{2.14}
$$

Assuming an elasto-plastic temperature dependent constitutive model, the macroscopic stress-strain constitutive relation can be determined using the average subcell stresses,

$$
\bar{\sigma} = C^* : (\bar{\varepsilon} - \varepsilon^I - \varepsilon^T).
\tag{2.15}
$$

Where C^* is the effective elastic stiffness tensor of the multiphase composite in terms of elastic stiffness $C^{\alpha\beta\gamma}$ of the constituents.

GMC has been used to investigate the behavior of metal matrix and polymer matrix woven composites [20, 73, 74, 75]. To account for the lack of inherent shear coupling in GMC when performing homogenization of a woven repeating unit cell for polymer matrix composites, a two step homogenization procedure in which homogenization in the through thickness is performed first then in-plane homogenization to allow for normal shear coupling [20]. For micromechanics analysis throughout the dissertation, a plain weave RUC with subcell size of $5 \times 5 \times 4$, is used (see Figure 2.3a [21]), which takes advantage of homogenized subcells through the thickness then homogenization in-plane as represented in Figure 2.3b. For the plain weave RUC from [21], the relationship between the fiber volume fraction in the tow can be related to the RUC level fiber volume fraction as shown in Equation 2.16.

$$V_{f,RUC} = \frac{8\left(\frac{w_t g_t t_t}{2}\right) + 4\left(w_t^2 t_t\right)}{(2g_t + 2g_t)(2g_t + 2g_t)t_t} V_{f,tow} \tag{2.16}$$

Which can be simplified to

$$V_{f,RUC} = \frac{w_t}{(w_t + g_t)} V_{f,tow} \tag{2.17}$$

Where w_t is the tow width and t_t are the fiber tow bundle width and thickness. Additionally, it should be noted that the tow cross-sectional shape is a simplified rectangle.

Figure 2.3: Plain weave configuration (a) 3-representation (MAC/GMC Manual) and (b) in-plane homogenization. Adapted from [21]

2.3 Tabulated Composite Plasticity Material

The MAT 213 material model is designed to predict the elastic and inelastic behavior of polymer matrix composite materials under impact loads. The material constitutive model can be segmented into three parts: deformation, damage, and failure model. It is currently designed for use with solid elements and thin shell elements. The full description of the formulation of the deformation model can be found in [2, 3, 76]. The minimum material tests needed for input are 12 curves which includes tension and compression in all three principle material directions (PMD), shear curves in the principle material planes (PMP) and 45 deg off-axis curves in the three PMP. The tabular composite plasticity model for the stresses is driven by elastic strains and the constitutive relationship is written in rate form by decomposition of total strain rate into elastic and plastic components as follows

$$\dot{\sigma} = C : (\dot{\varepsilon^e}) = C : (\dot{\varepsilon^t} - \dot{\varepsilon^p}) \tag{2.18}$$

24

where $\dot{\sigma}$ is the Cauchy stress rate tensor, $\dot{\varepsilon}^t$ is the total strain rate tensor, $\dot{\varepsilon}^p$ is the plastic strain rate tensor, $\dot{\varepsilon}^e$ is the elastic strain rate tensor, and C is the orthotropic elastic stiffness tensor shown in Equation 2.19

$$\mathbf{C} = \mathbf{S}^{-1} = \begin{bmatrix} \frac{1}{E_{11}} & -\frac{\nu_{21}}{E_{22}} & -\frac{\nu_{31}}{E_{33}} & 0 & 0 & 0 \\ -\frac{\nu_{12}}{E_{11}} & \frac{1}{E_{22}} & -\frac{\nu_{32}}{E_{33}} & 0 & 0 & 0 \\ -\frac{\nu_{13}}{E_{11}} & \frac{\nu 23}{E_{22}} & \frac{1}{E_{33}} & 0 & 0 & 0 \\ 0 & 0 & 0 & \frac{1}{G_{12}} & 0 & 0 \\ 0 & 0 & 0 & 0 & \frac{1}{G_{23}} & 0 \\ 0 & 0 & 0 & 0 & 0 & \frac{1}{G_{13}} \end{bmatrix}^{-1} \tag{2.19}$$

For the deformation model, a general quadratic three-dimensional orthotropic yield function is used based on the Tsai-Wu failure model and is specified as follows

$$f(\sigma) = a + f^T \sigma + \sigma^T F \sigma^T \tag{2.20}$$

$$f(\sigma) = a + \begin{pmatrix} F_1 \\ F_2 \\ F_3 \\ 0 \\ 0 \\ 0 \end{pmatrix}^T \begin{pmatrix} \sigma_{xx} \\ \sigma_{yy} \\ \sigma_{zz} \\ \sigma_{xy} \\ \sigma_{yz} \\ \sigma_{zx} \end{pmatrix} + \begin{pmatrix} \sigma_{xx} \\ \sigma_{yy} \\ \sigma_{zz} \\ \sigma_{xy} \\ \sigma_{yz} \\ \sigma_{zx} \end{pmatrix}^T \begin{bmatrix} F_{11} & F_{12} & F_{13} & 0 & 0 & 0 \\ F_{12} & F_{22} & F_{23} & 0 & 0 & 0 \\ F_{13} & F_{23} & F_{33} & 0 & 0 & 0 \\ 0 & 0 & 0 & F_{44} & 0 & 0 \\ 0 & 0 & 0 & 0 & F_{44} & 0 \\ 0 & 0 & 0 & 0 & 0 & F_{44} \end{bmatrix} \begin{pmatrix} \sigma_{xx} \\ \sigma_{yy} \\ \sigma_{zz} \\ \sigma_{xy} \\ \sigma_{yz} \\ \sigma_{zx} \end{pmatrix}^T \tag{2.21}$$

where 1, 2, and 3 refer to the PMD. The yield function coefficients corresponding to the stress solely in the PMD allowing for distinguishing between tensile and compressive states of loading. The a-term is -1 for unity at zero. A positive value of $f(\sigma)$ indicates a plastic state and negative indicates an elastic state. In the yield function, σ_{ij} represents the stresses, F_{ij} and F_k are coefficients that vary based on the current values of the yield stresses in the various coordinate directions. The coefficients of the yield function can be computed based on the values of the current yield stresses

in the various normal and shear directions as follows

$$
\begin{aligned}
&F_1 = \frac{1}{\sigma_{11}^T} - \frac{1}{\sigma_{11}^C} && F_{11} = \frac{1}{\sigma_{11}^T \sigma_{11}^C} && F_{44} = \frac{1}{\sigma_{12}^2} \\
&F_2 = \frac{1}{\sigma_{22}^T} - \frac{1}{\sigma_{22}^C} && F_{22} = \frac{1}{\sigma_{22}^T \sigma_{22}^C} && F_{55} = \frac{1}{\sigma_{23}^2} \\
&F_3 = \frac{1}{\sigma_{33}^T} - \frac{1}{\sigma_{33}^C} && F_{33} = \frac{1}{\sigma_{33}^T \sigma_{33}^C} && F_{66} = \frac{1}{\sigma_{13}^2}
\end{aligned}
\tag{2.22}
$$

where the superscript T indicates the tensile yield stress and superscript C indicates compression yield stress which allows the tabular plasticity model to handle asymmetric yield surface evolution. This allows for different behavior in tension and compression. The coefficients are a result of assuming a state of uniaxial stress in a given PMD or PMP and solving for the unique set of values which satisfy the yield function [3].

A non-associative flow rule is used to compute the evolution of the components of plastic strain. The plastic potential for the flow rule as follows

$$
\dot{\varepsilon}^p = d\lambda \frac{\partial h}{\partial \sigma} \tag{2.23}
$$

$$
h^2 = \sigma^T \mathbf{H} \sigma \tag{2.24}
$$

with

$$
\begin{aligned}
h^2 = {}& H_{11}\sigma^2{}_{11} + H_{22}\sigma^2{}_{22} + H_{33}\sigma^2{}_{33} + 2H_{12}\sigma_{11}\sigma_{22} + 2H_{23}\sigma_{22}\sigma_{33} + 2\sigma_{33}\sigma_{11} \\
&+ H_{44}\sigma^2{}_{12} + 55\sigma^2{}_{23} + H_{66}\sigma^2{}_{13} + H_{44}\sigma^2{}_{21} + 55\sigma^2{}_{32} + H_{66}\sigma^2{}_{31}
\end{aligned}
\tag{2.25}
$$

where the H_{ij} terms are the independent flow rule coefficients assumed to be constant and σ_{ij} are the current stress values. In order to ensure convexity of the yield surface,

the flow rule coefficients must satisfy the following conditions [3].

$$H_{11} \geq 0$$
$$H_{22} \geq 0$$
$$H_{33} \geq 0$$
$$H_{44} \geq 0$$
$$H_{55} \geq 0 \quad (2.26)$$
$$H_{66} \geq 0$$
$$H_{11}H_{22} - H_{12}^2 \geq 0$$
$$H_{33}H_{22} - H_{23}^2 \geq 0$$
$$H_{11}H_{33} - H_{31}^2 \geq 0$$

Previous MAT213 works [2, 3, 4], have characterized the flow rule coefficients through optimization routines or using off-axis curves similar to [77] which used an associative flow rule. The plastic potential function is used in the flow law with the normality hypothesis of classical plasticity is assumed to apply where λ is the scalar plasticity multiplier [78]. The plastic strains can then be defined in terms of the plastic multiplier to relate constant the flow coefficients with plastic strains through Poisson ratios as follows [3]

$$\sigma_{xx} \neq 0 \quad \sigma_{yy} \neq 0 \qquad\qquad \sigma_{zz} \neq 0$$
$$\nu_{12}^p = \frac{\dot{\epsilon}_{yy}^p}{\dot{\epsilon}_{xx}^p} = \frac{H_{12}}{H_{11}} \quad \nu_{21}^p = \frac{\dot{\epsilon}_{xx}^p}{\dot{\epsilon}_{yy}^p} = \frac{H_{12}}{H_{22}} \qquad \nu_{32}^p = \frac{\dot{\epsilon}_{yy}^p}{\dot{\epsilon}_{zz}^p} = \frac{H_{23}}{H_{33}} \quad (2.27)$$
$$\nu_{13}^p = \frac{\dot{\epsilon}_{zz}^p}{\dot{\epsilon}_{xx}^p} = \frac{H_{13}}{H_{11}} \quad \nu_{23}^p = \frac{\dot{\epsilon}_{zz}^p}{\dot{\epsilon}_{yy}^p} = \frac{H_{23}}{H_{22}} \qquad \nu_{31}^p = \frac{\dot{\epsilon}_{xx}^p}{\dot{\epsilon}_{zz}^p} = \frac{H_{13}}{H_{33}}$$

The damage model is used to relate the true stress state to the effective stress state [79]. The effective stress is generated by assuming that it is due to both damage and plasticity. The relationship between the true and effective is described using the damaged tensor in Equation 2.28.

27

$$
\begin{pmatrix} \sigma_{xx} \\ \sigma_{yy} \\ \sigma_{zz} \\ \sigma_{xy} \\ \sigma_{yz} \\ \sigma_{zx} \end{pmatrix} = \begin{bmatrix} M_{11} & M_{12} & M_{13} & M_{14} & M_{15} & M_{16} \\ M_{21} & M_{22} & M_{23} & M_{24} & M_{25} & M_{26} \\ M_{31} & M_{32} & M_{33} & M_{34} & M_{35} & M_{36} \\ M_{41} & M_{42} & M_{43} & M_{44} & M_{45} & M_{46} \\ M_{51} & M_{52} & M_{53} & M_{54} & M_{55} & M_{56} \\ M_{61} & M_{62} & M_{63} & M_{64} & M_{65} & M_{66} \end{bmatrix} \begin{pmatrix} \sigma_{xx}^{eff} \\ \sigma_{yy}^{eff} \\ \sigma_{zz}^{eff} \\ \sigma_{xy}^{eff} \\ \sigma_{yz}^{eff} \\ \sigma_{zx}^{eff} \end{pmatrix}
\tag{2.28}
$$

where σ_{ij} is the true stress and σ_{ij}^{eff} is the effective stress. The full damage tensor shown in Equation 2.28 can lead to multi-axial stress states in the effective stress space with uni-direction state in true space. Therefore, a semi-coupled directionally dependent damage tensor shown in Equation 2.29 is used

$$
\begin{pmatrix} \sigma_{xx} \\ \sigma_{yy} \\ \sigma_{zz} \\ \sigma_{xy} \\ \sigma_{yz} \\ \sigma_{zx} \end{pmatrix} = \begin{bmatrix} M_{11} & 0 & 0 & 0 & 0 & 0 \\ 0 & M_{22} & 0 & 0 & 0 & 0 \\ 0 & 0 & M_{33} & 0 & 0 & 0 \\ 0 & 0 & 0 & M_{44} & 0 & 0 \\ 0 & 0 & 0 & 0 & M_{55} & 0 \\ 0 & 0 & 0 & 0 & 0 & M_{66} \end{bmatrix} \begin{pmatrix} \sigma_{xx}^{eff} \\ \sigma_{yy}^{eff} \\ \sigma_{zz}^{eff} \\ \sigma_{xy}^{eff} \\ \sigma_{yz}^{eff} \\ \sigma_{zx}^{eff} \end{pmatrix}^{T}
\tag{2.29}
$$

where M_{ii} in the damage tensor are the damage parameters which are tracked as a function of plastic strain. The experimental characterization of these damage parameters are difficult to perform and obtain. Previous works [79], have performed low-cycle coupled and uncoupled damage coupon experiments loaded in transverse compression and in-plane shear for a unidirectional composite. When experimental data is available, pre-peak damage can be accounted for. However, when data is not available, the post-peak damage can be calibrated to better match higher level experiments such as impact or crash tests. The addition of the post-peak curve is synthetic and is used for numerical stability [80].

Chapter 3

Composite Material Experiments

Experiments were performed with a polymer matrix composite (PMC) manu-factured using Vacuum Assisted Resin Transfer Molding (VARTM). Two balanced plain weave carbon fabrics, a 3k tow Hexforce 282 from Hexcel and a 12k tow T700 from Toray, are infused using SC-780, a low viscosity two-part epoxy provided by Kaneka (formally Applied Polymeric). Before infusing, the pot of mixed two-part epoxy was cycled under vacuum to reduce the presence of voids. After infusing, plates were cured overnight at room temperature, and then post-cured for 6-hours at 71-77 degrees Celsius. For the 3k material $[0]_{10}$, $[0]_{20}$, and $[0]_{32}$ layup plates were manufactured to get a 2.02 mm, 3.89 mm and 6.15 mm overall thickness. Similarly, the 12k material was manufactured with a $[0]_6$, $[0]_{12}$, and $[0]_{20}$ layup resulting in plates with 2.0 mm, 3.7 mm, and 6.7 mm overall thickness.

Normal engineering stress, σ_{xx}, is calculated using Equation 3.1.

$$\sigma_{xx} = \frac{F}{A} \tag{3.1}$$

Where F is the axial force and A is the cross section area. Engineering stress is used for in-plane tension and in-plane compression stress-strain curves. For in-plane shear, engineering shear stress is calculated following Equation 3.2.

$$\tau_{xy} = \frac{V}{A} \tag{3.2}$$

For short beam shear experiments transverse shear is calculated using beam theory of a simply supported three-point bending beam with a load at the mid-length [12]. It is assumed that the axial strain distribution through the beam thickness behaves linearly. The normal bending stress, σ_b also behaves linearly with axial stress equal to zero along the neutral axis at $x = \pm L/4$.

$$\sigma_b = \frac{Mz}{I_y} \tag{3.3}$$

Where $M = PL/8$ is the bending moment, at $x = \pm L/4$, I_Y is the second moment of area of a rectangular beam cross section about the y-axis, and z is the distance from the neutral axis. The through thickness shear stress follows a nonuniform distribution as shown in Equation 3.4 [12]

$$\tau_{xz} = \frac{3P}{4A} \left(1 - \left(\frac{2z}{h} \right)^2 \right) \tag{3.4}$$

where A is the beam cross section and P is the load applied at mid-length. The maximum transverse shear is used for SBS which occurs at $z = 0$. This reduces Equation 3.4 to

$$\tau_{xz,MAX} = \frac{3}{4} \left(\frac{P}{A} \right) \tag{3.5}$$

3.1 Quasi-static Coupon

3.1.1 Specimen Design

In-plane tension specimens were trimmed from the 2 mm thick plate using a wet tile saw following geometry recommendations in ASTM D3039 [9]. Tabbing

was done to help reduce failure near the test frame grips. Rectangular tabs are cut from a 1.6 mm (1/16 inch) thick fiberglass FR4 sheets using a wet tile saw. Tab lengths of 25.4 mm are used for the 3k material and 38.1 mm for the 12k material. Aeropoxy ES6228, a structural paste adhesive, was used to bond the tabs to the composite specimens. Surface preparation of the bond area was done to minimize poor bonding. Tab bonding of a large plate using a spacer that was cut to the specimen gage length was used to help align the straight tabs. The resulting gage length was 152.4 mm (6 inches) for the 3k material and 177.8 mm (7 inches) for the 12k material. A shorter length for the 3k was used due to the smaller sized repeating unit cell compared to the 12k tow material. After bonding, specimens were cut to a length of 8 inches for 3k, and 10 inches for 12k. Tabs were sanded to get a 10-degree taper to the outer surface of the tab. This was done to reduce stress concentrations in the gripping area. Drawings of the tensions specimen are shown in Figure 3.2. An image before applying the DIC speckle of both the 3k and 12k materials is shown in Figures 3.1a and 3.1b. Reflective tape for the laser extensometer is place on the edges of the tension specimen area of interest.

In plane compression specimens were designed following ASTM 695M [10]. This standard is used to determine compressive strength and modulus using two separate specimens. Tabbed and untabbed specimens for strength and modulus, respectively. Tabbed specimens with an enlarger gage section, compared to the strength specimens in ASTM D695M [10] as shown in Figure 3.3 below, were designed based on ASTM D695M[10]. For the design of the specimens the gage section was then enlarged to allow for at least 1.5 RUCs for both 3k and 12k material and the thickness, about 4 mm, of the specimen was also increased to prevent buckling. Testing was performed using a Wyoming test fixture and representative images of compression specimens in fixture are shown in Figures 3.1c and 3.1d. Tabbing material was changed from FR4 fiberglass to carbon, same material as specimen being tested, with a 2 mm thickness. Debonding between tab and specimen were observed in initial studies.

31

(a) 3k, tension

(b) 12k, tension

(c) 3k, compression

(d) 12k, compression

(e) 3k, short beam shear

(f) 12k, short beam shear

(g) 3k, v-notch shear

(h) 3k, v-notch shear
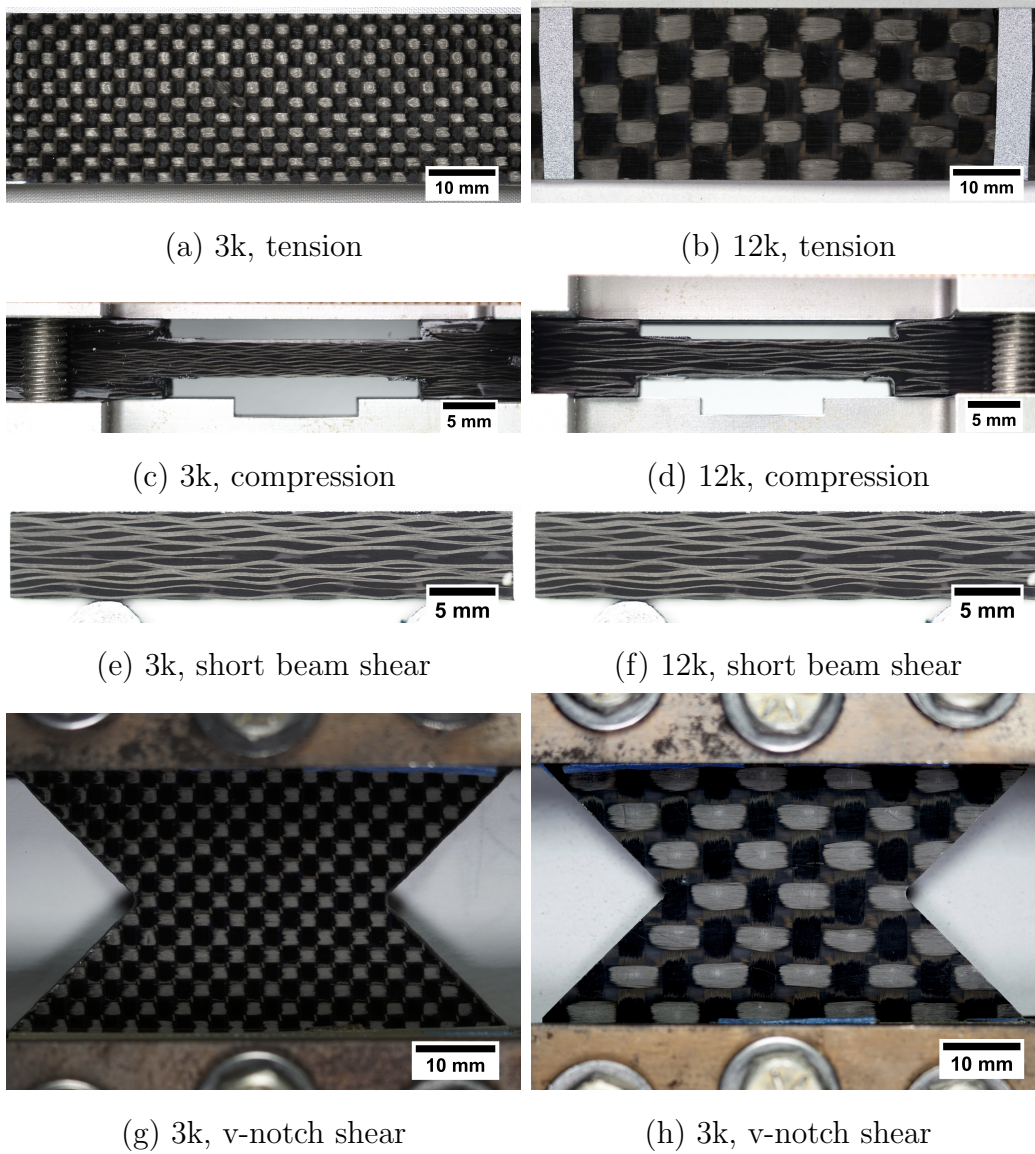
Figure 3.1: Pre-test images showing specimen gage section.
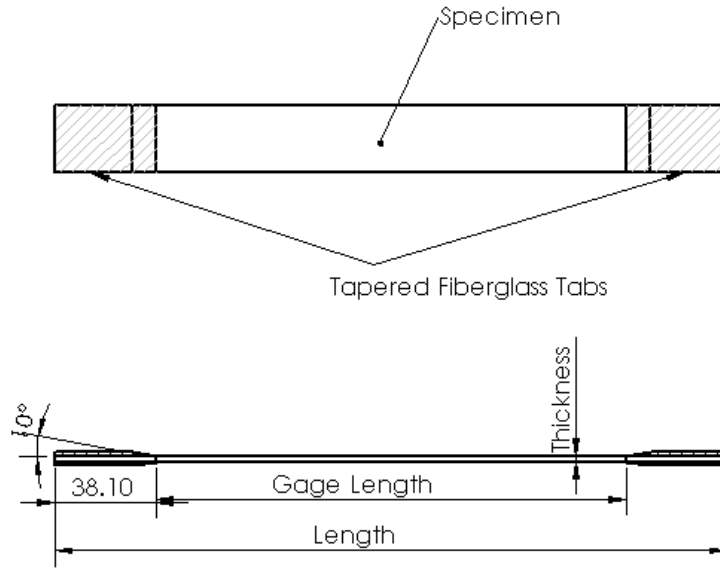
Figure 3.2: Tension specimen geometry diagram.

Surface preparation and adding an inverted taper to the tab was done to create a stronger bond and to lower stress concentrations near the boundaries similar to what has been done for adhesively bonded joints [81, 82]. Additionally, a small milling machine (Little Milling Shop HiTorque) was used to achieve straight and parallel specimen ends. This helps to remove any eccentricity that can be introduced if loading is not applied evenly. For compression experiments, a 0.5 mm/sec loading rate was applied. The MTS controller captured axial force, crosshead displacement and two analog input channels for linear strain gage reading and an ESPER trigger box voltage, respectively. In total four specimens were tested with strain gages for calibration. One for each loading direction and material. For the remaining specimens, only DIC was used.

In-plane v-notch rail shear specimens were designed following ASTM D7078M [63]. Using the 2 mm thick plate, shear specimens were water-jet cut to get the
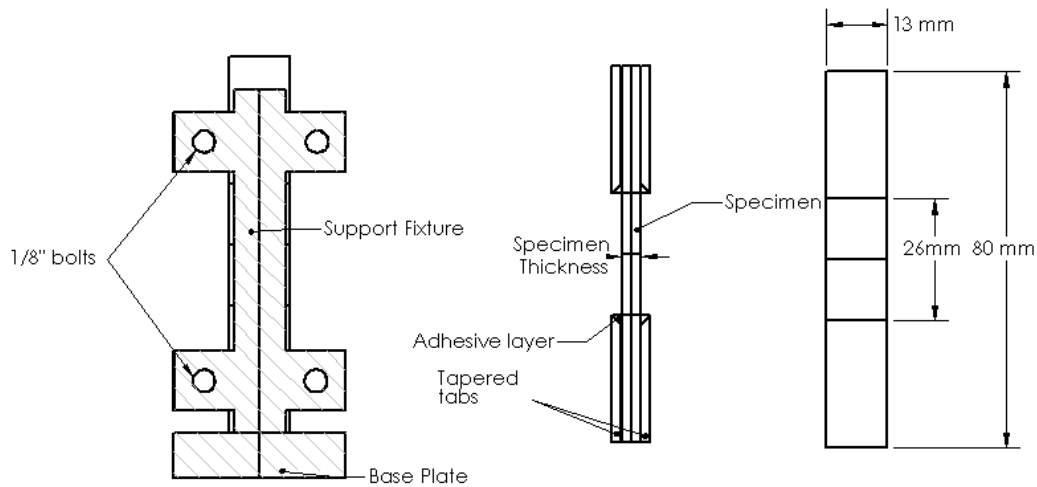
Figure 3.3: Compression specimen and fixture.

90-degree notched geometry, as shown in Figure 3.1g and 3.1h, for the 3k and 12k material, respectively. Specimens are machined with notch tips in the warp direction, as illustrated in Figure 3.4a. Next, alignment tools were used in combination with the hardened steel test fixture halves, Figure 3.4c, to match drill holes with a 6.35 mm (1/4 inches) carbide drill bit. Fiberglass FR4 rectangular tabs were placed behind the specimen to avoid damage when drilling and used as reusable fixture tabbing spacers when testing.

Rectangular short beam shear specimens following ASTM D2344 [83], for interlaminar shear strength, are cut from the thicker composite plates to nominal dimensions of 38.1 mm x 12.7 mm using a wet tile saw. Compression and SBS specimens were then polished with fine grit sandpaper to remove imperfections from the tile saw. The polished surface is critical for optical microscope images and DIC speckle application. Images of representative short beam shear specimens are shown in Figures 3.1e and 3.1f. The 3k material was noted to have more visible voids than the 12k material. Dimensions of the specimen design for the short beam shear are shown in Figure 3.5.

34

Figure 3.4: V-notch rail shear (a) specimen geometry, (b) quasi-static experiments fixture diagram and (c) fixture half.
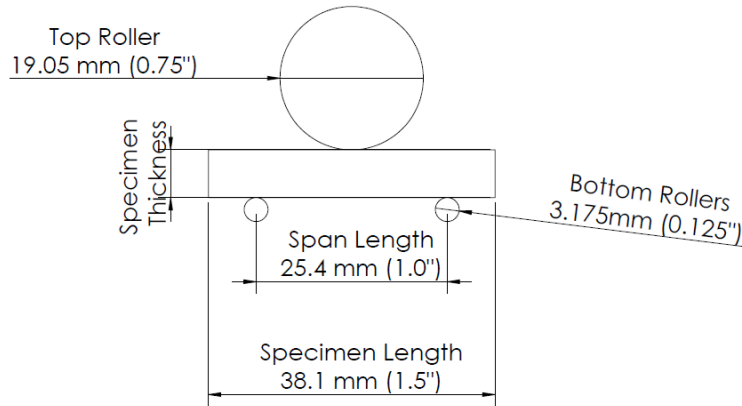
Figure 3.5: Short beam shear fixture supports diagram

3.1.2   Experimental setup

Experimental testing was performed using MTS hydraulic load frames with load capacity of 22 kip (100 kN) and 55 kip (245 kN) in displacement control loading at room temperature conditions. Composite tension experiments were performed using the 55 kip load frame, while the 22 kip load frame was used for compression and shear experiments. For all experiments axial force, axial displacement, and time data was collected. For in-plane tension reflective tape was placed on the surface to measure local displacement with a laser extensometer which served as calibration for tension DIC measurements. Additionally, for tension specimens, proper alignment of the grips was performed before testing. Additionally, center lines were marked on both ends of the specimen to help with gripping and a digital level was used to ensure the specimen was not misaligned after gripping. The loading rate of tension specimens was set to 1 mm/s. Similarly, the laser extensometer was used to measure fixture displacements which was compared with speckled areas on the fixture within the short beam shear (SBS) image field of view (FOV). For short beam shear experiments, the recommended 3.18 mm diameter bottom rollers from ASTM D2344 were used. It was

found through initial studies that using a 19.05 mm top roller reduced compressive failure near the contact point. Previous works, [12], have similarly used a larger roller than the ASTM recommendation. Figure 3.5 shows a diagram of the roller supports, span length, and specimen length. The loading rate for short beam shear experiments was set to 1 mm/s.

Quasi-static in-plane shear experiments were tested using a custom bolted hardened steel fixture, Figure 3.1c, based on ASTM D7078M and an Arcan shear fixture. The same additively manufactured tools used for alignment that were used to drill holes were used to assemble the fixture. To help alleviate stress at bolt holes, FR4 tabs with the shear fixture hole patterns were attached, not bonded, to the specimen and were used for specimen alignment. Steel gripping plates were marked in the center to help with alignment. Bolts connecting fixture halves to the gripping plates were not torqued up, making these pin connections. In-plane shear specimens were loaded at 2 mm/s.

Initial experiments captured images using a Sony α6000 camera in video mode, 1920 px $\times$ 1080 px at 60 frames per second (fps). To reduced this large data set images are then down sampled to 1 fps. Sony camera has the capabilities to capture high resolution still images at 6000 px $\times$ 4000 px. To take advantage of the high resolution images an Esper Triggerbox is used for quasi-static room temperature experiments. Figure 3.6a below shows a representative diagram of the experimental setup. Using Esper's Triggerbox Controller 1.6 software with the settings shown in the Figure A.1, which has two output channels turned on and is used for 2D DIC. One of the channels is connected to a camera to trigger the image capture. The second output channels from the Esper box is connected to the MTS controller to time synchronize force measurements. It is recommend to use a data acquisition sampling frequency of 120 Hz. This creates a more defined pulse in the data as shown in Figure 3.6. Sampling at a low frequency (i.e., 1-10 Hz.) makes it difficult to distinguish pulses. For 3D DIC an additional output channel would need to be

turn on to trigger two cameras and feed into the data acquisition.

Before deciding on an appropriate speckle size, images of the FOV were captured. Once the FOV is decided and measured, a calibration scale is then determined. ImageJ , an open source image processing software, was used to determine the mm/px conversion for calibration of the FOV Additionally, ImageJ is used to measure a rectangular AOI to know available pixels for DIC. Global AOI were analyzed to understand the global behavior of the coupon, while local AOI were used to extract average strain values for stress-strain curves. These AOIs used for DIC analysis of woven composite experimental tests are shown in Figure 3.7.

Commercial VIC2D-6 Software is used for all analysis and allows for control of the calibration scale, correlation criteria and interpolation functions. ZNSSD correlation function with an 8th order interpolation function with the subset, step and strain window size used for quasi-static experiments summarized in Table 3.1. Subset values suggested from VIC2D software were used or subsets close to suggested values were used. Adjustments to these were done to allow for an appropriate VSG that is dependent on the subset, step and filter size. The VSG is calculated using Equation 2.6. Next, VIC target software is used to create an appropriate target file for the specific experiment based on the FOV and AOI. Targets were printed on white printer paper, then glued onto clear flat plastic. Printed target spacing was also measured to verify calibration target was not scaled by printer settings.
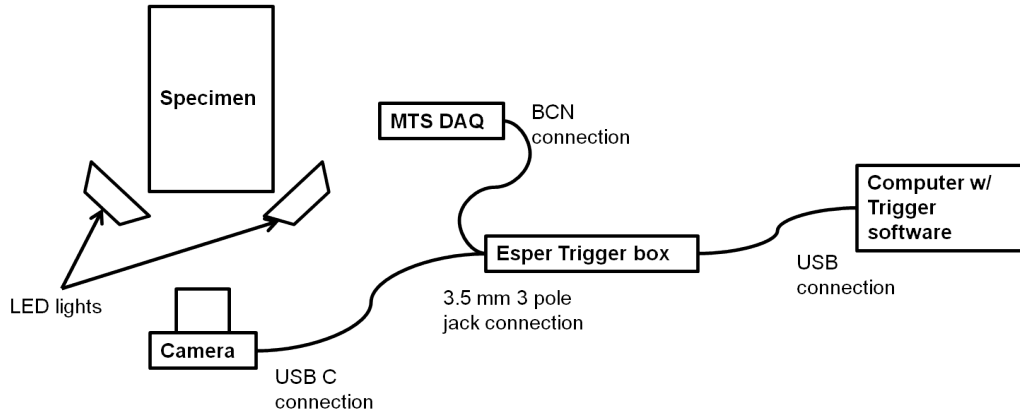
(a)
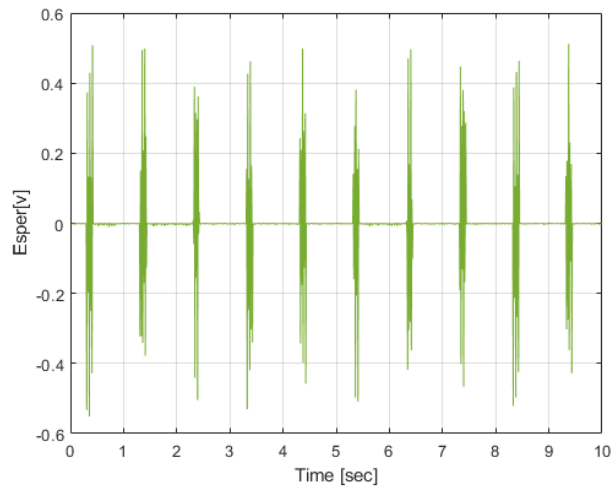
(b)

Figure 3.6: (a) Experimental setup using Esper Triggerbox with MTS load frame for time synchronization and (b) example MTS analog input reading from Esper trigger box with a sample rate of 120 Hz.
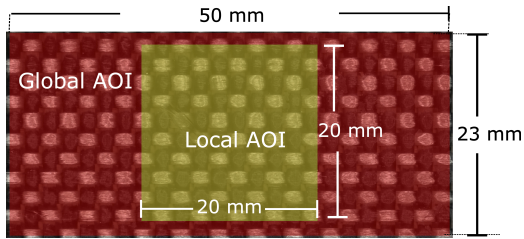
(a) 3k, tension
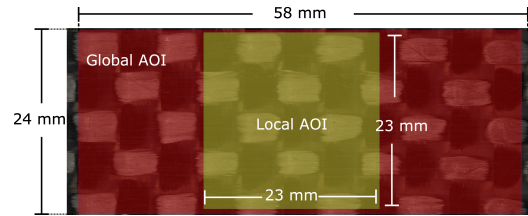
(b) 12k, tension
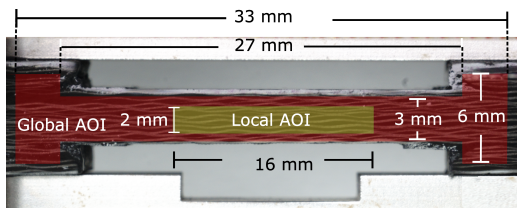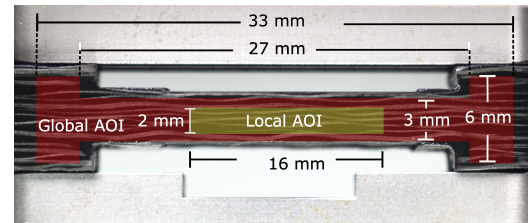
(c) 3k, compression

(d) 12k, compression
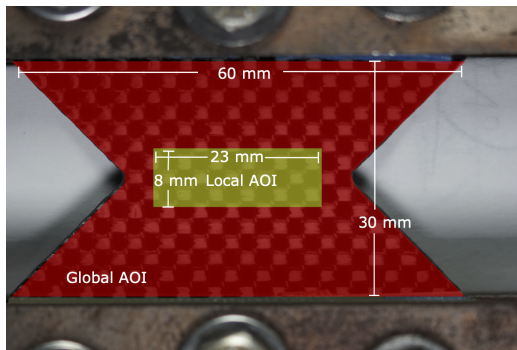
(e) 3k, v-notch shear
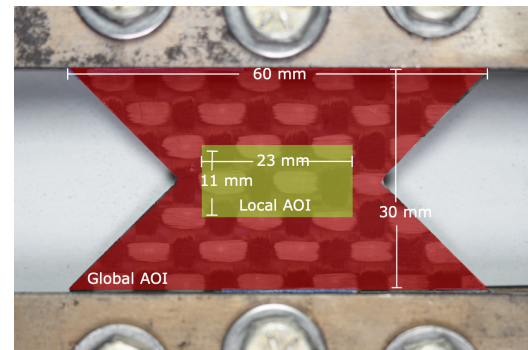
(f) 12k, v-notch shear

Figure 3.7: Diagrams of DIC areas of interest (AOI) used for analysis for 3k and 12k materials.
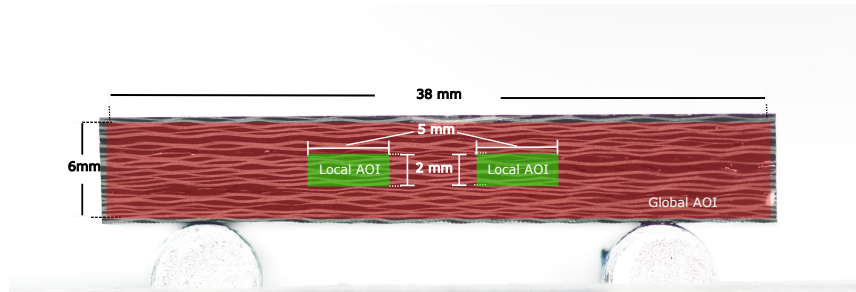
(a)
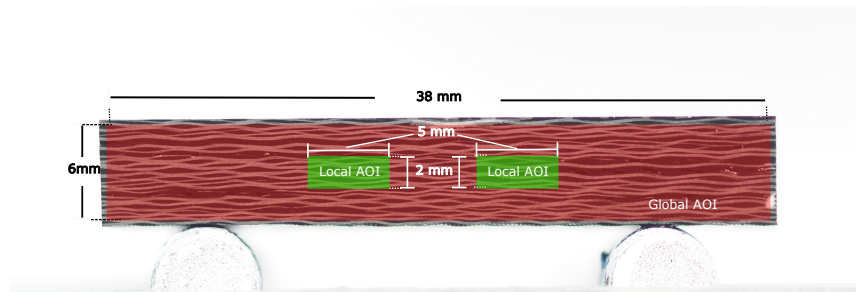
(b)

Figure 3.8: Diagrams of DIC areas of interest used for analysis for (a) short beam shear 3k, (b) short beam shear 12k

Table 3.1: DIC parameters for quasi-static experiments using Sony α 6000 camera with VIC-2D 6 software.

Specimen	Tension	Compression	Rail shear	Short beam shear
Scale Factor	0.013	0.009	0.0127	0.009
Subset Size (px)	49	31	35	37
Step Size (px)	3	3	3	5
Strain Filter (px)	9	9	5	5
VSG (mm)	0.95	0.55	0.60	0.55

3.1.3 Results

In-plane tension and in-plane shear experiments measured strain quantities using a DIC virtual strain gage (VSG) size of 1 mm. Whereas, short beam shear, compression and v-notch shear experiments used a smaller VSG size of between 0.55 to 0.6 mm. Summary of the test matrix is shown in Table 3.2 and representative contours of DIC experiments are shown in Figures 3.9 and 3.10 for the 3k and 12k materials, respectively. Modulus and strength values of the 3k material are summarized and compared with similar material architectures in the Tables A.1 and A.2 in the Appendix.

Results of experimental DIC stress-strain curves for tension used the average of a rectangular area, as shown in Figures 3.9a and 3.10a, of 20×20 mm^2 and 23×23 mm^2 for the 3k and 12k materials, respectively. This corresponds to roughly 5×5 RUCs for the 3k and 2×2 RUCs for the 12k material. The stress-strain curve for the 3k material behaved mostly linearly to failure (see experimental data plotted in Figure 3.11a) and inhomogeneous strain fields became more prominent at higher load levels, which is clearly visible in Figures 3.9a and 3.10a for both materials. The 12k material, however, developed inhomogeneous strain fields at lower loads compared with the 3k material, which led to more nonlinearity in the stress-strain response leading up to failure, as shown in Figure 3.11b. As shown in Figures 3.9a and 3.10a

42

(a) tension, ϵ_{xx}

(b) compression, ϵ_{xx}

(c) v-notch shear, γ_{xy}

(d) short beam shear, γ_{xz}

Figure 3.9: DIC contour plots for 3k tow (a) in-plane tension, (b) in-plane compression, (c) in-plane shear, and (c) short beam shear experiments.

(a) tension, ϵ_{xx}

(b) compression, ϵ_{xx}

(c) v-notch shear, γ_{xy}

(d) short beam shear, γ_{xz}

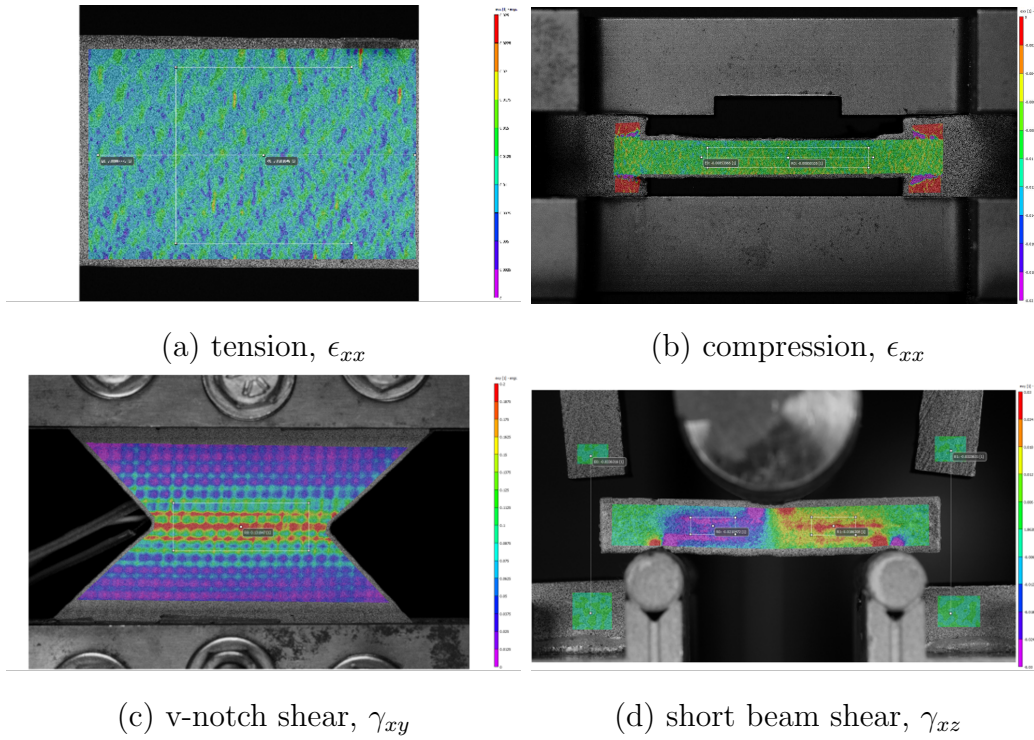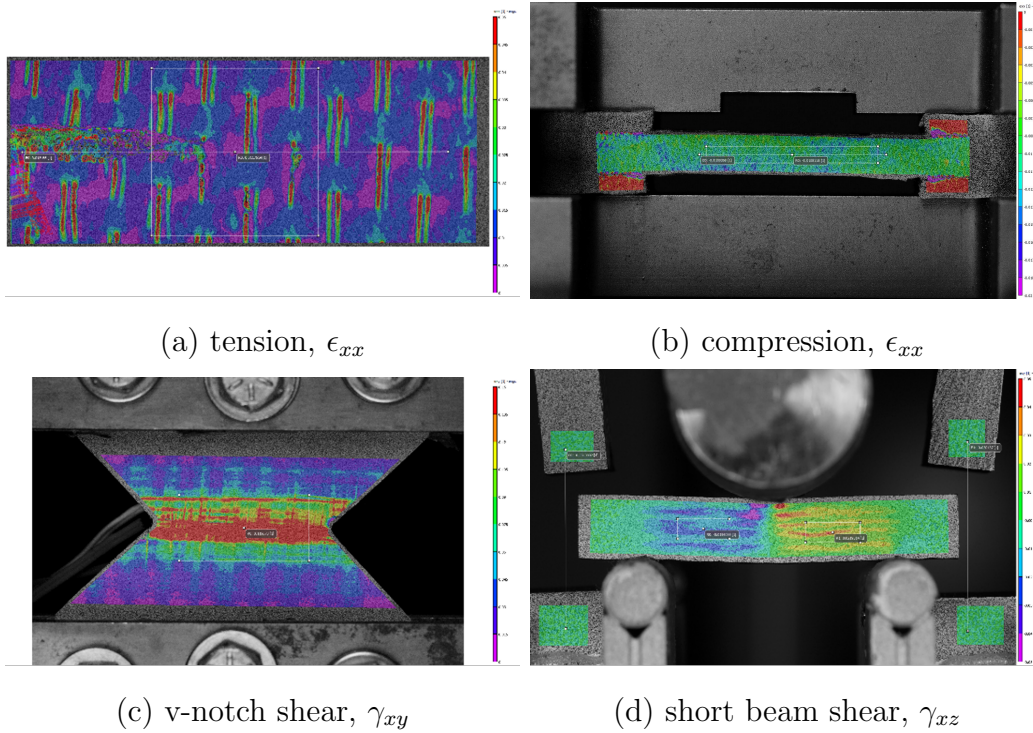Figure 3.10: DIC contour plots for 12k tow (a) in-plane tension, (b) in-plane compression, (c) in-plane shear, and (c) short beam shear experiments.

Table 3.2: Test matrix summary of quasi-static room temperature experiments.

Material	Specimen	Specimen Number
3k	In-plane tension, 2 direction	4
3k	In-plane compression, 1-direction	5
3k	In-plane compression, 2-direction	5
3k	In-plane shear, 12-plane	4
3k	Short beam shear, 13-plane	2
3k	Short beam shear, 23-plane	6
12k	In-plane tension, 1 direction	3
12k	In-plane tension, 2 direction	3
12k	In-plane compression, 1-direction	5
12k	In-plane compression, 2-direction	5
12k	In-plane shear, 12-plane	3
12k	Short beam shear, 13-plane	6
12k	Short beam shear, 23-plane	6

areas of high strain were observed in tows that were orthogonal to the direction of the load (horizontal direction in Figures 3.9a and 3.10a), which then formed into cracks and led to tow splitting. Additionally, the strain history of the local AOI for 12k tension is shown in Figure 3.13 which shows the initiation of transverse tows leading to the inhomogeneous strain fields seen in the DIC contour, Figure 3.10a. Figure 3.13 shows that the initiation of damage in the tows perpendicular to the load is seen to progressively increase until damage in the tows in the direction of the load initiates which leads to failure and DIC losing correlation accuracy.

Further investigation in to the local AOI of the tension experiments was done through the use of line slices to analyze the in-plane strain components evolution over time. Figure 3.14 show contours of the in-plane strain components plotted along the local AOI position as a function of time on the vertical axis. The strain in the axial direction behaves constant still image correlation is lost along the line. It can be seen from the contours that the presence of large shear strain are observed developed at around around frame 50. At the global scale this is when the fill
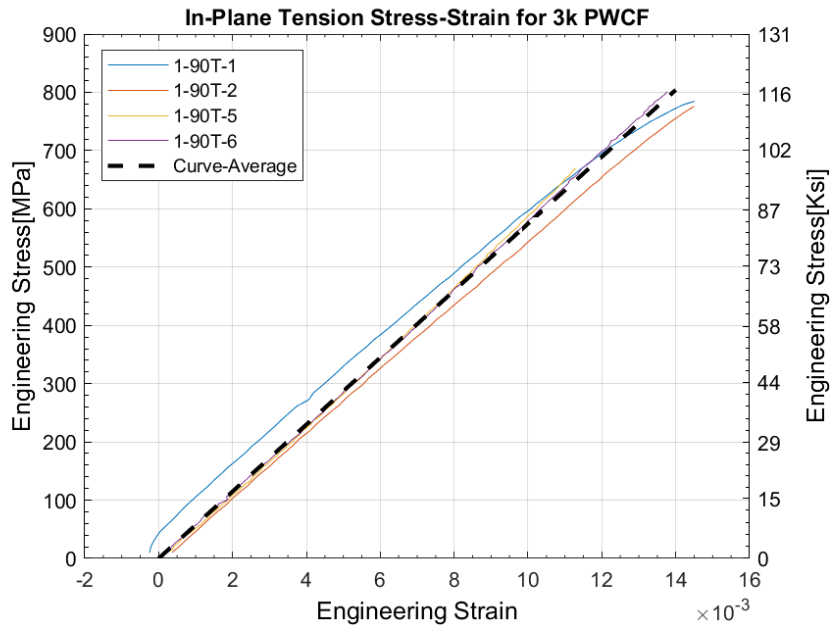
(a)
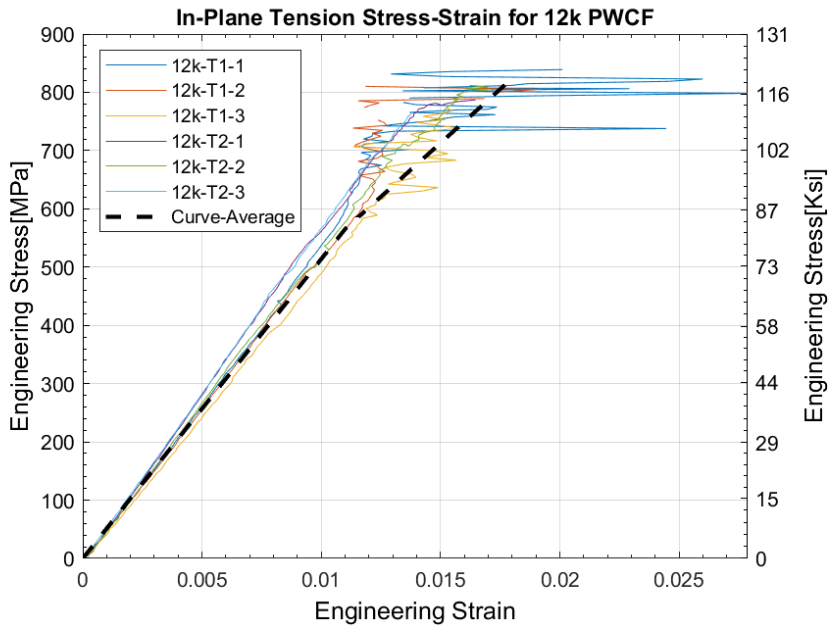
(b)

Figure 3.11: Tension stress strain for (a) 3k and (b) 12k PWCF

46

(a)

(b)
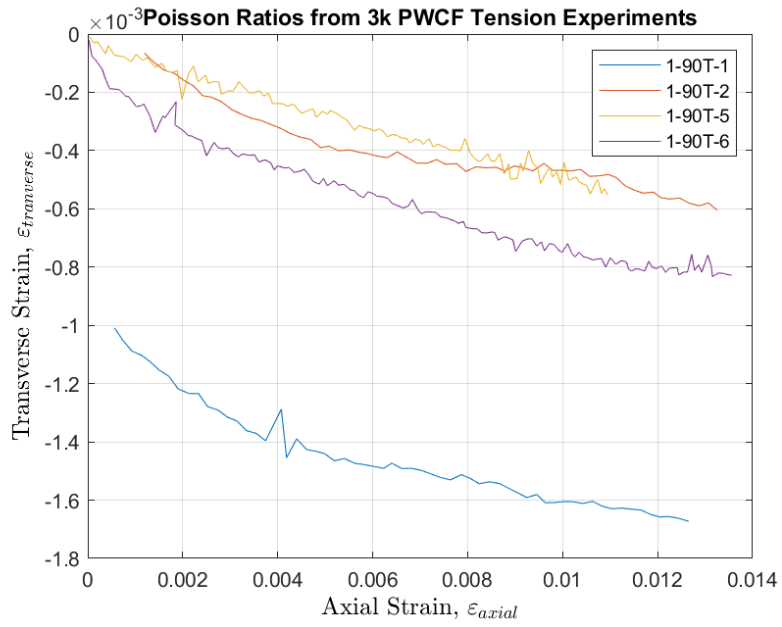
Figure 3.12: Possion's strain curves for from tension experiments for (a) 3k PWCF and (b) 12k PWCF

47
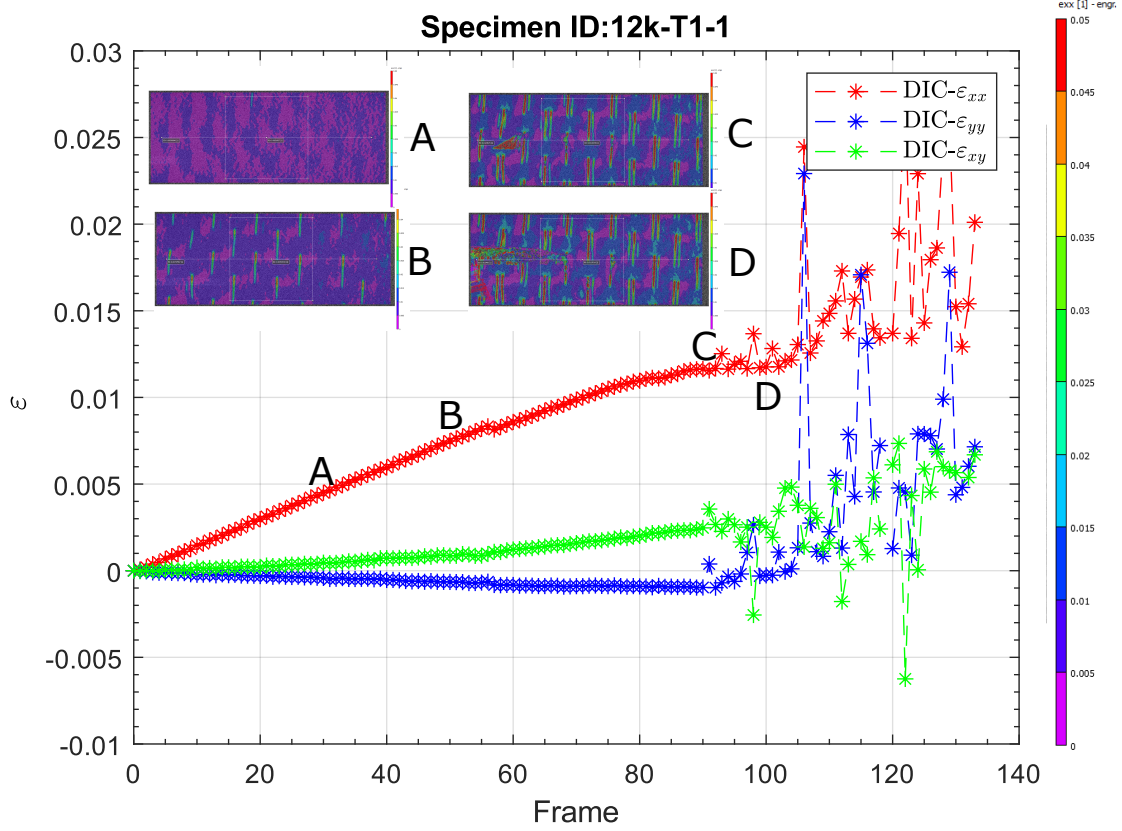
Figure 3.13: In-plane tension DIC strain history for 12k material

tows have progressively grown through the coupon, which is seen in Figure 3.13. Locally, meso-scale tow damage leads to large shear strains, Figure 3.14. With the accumulation of damage in the tow is observed to that shear strains localize in the warp fiber tow undulation zones and near the center of the fill fiber tow. Lastly, the normalized strain components along the lines slices at the time where the shear strain component begins to lose correlation is plotted in Figure 3.15. Two peaks are seen in the shear strain which are separated approximately the length of the 12k RUC. The axial and tranverse normalized strains remain low compared to the shear strains seen in Figure 3.15

For in-plane compression specimens, the AOI consists of an area of 2 mm in the thickness direction by 16 mm in the loading direction for both 3k and 12k materials. This corresponds to approximately 10 RUCs × 4 RUCs and 6 RUCs × 1.5 RUCs for the 3k and 12k materials, respectively. The material is observed to behave linearly in the stress-strain response, Figure 3.16 and homogeneous from DIC contours Figures 3.9b and 3.10b. The local area of interest is used to analyze the through thickness strain response. Figures 3.17a and 3.17b show the portion of the axial and transverse strain from the DIC local AOI. The linear portion from Figure 3.17b is used to determine through thickness Poisson's ratios, ν_{13} and ν_{23}.
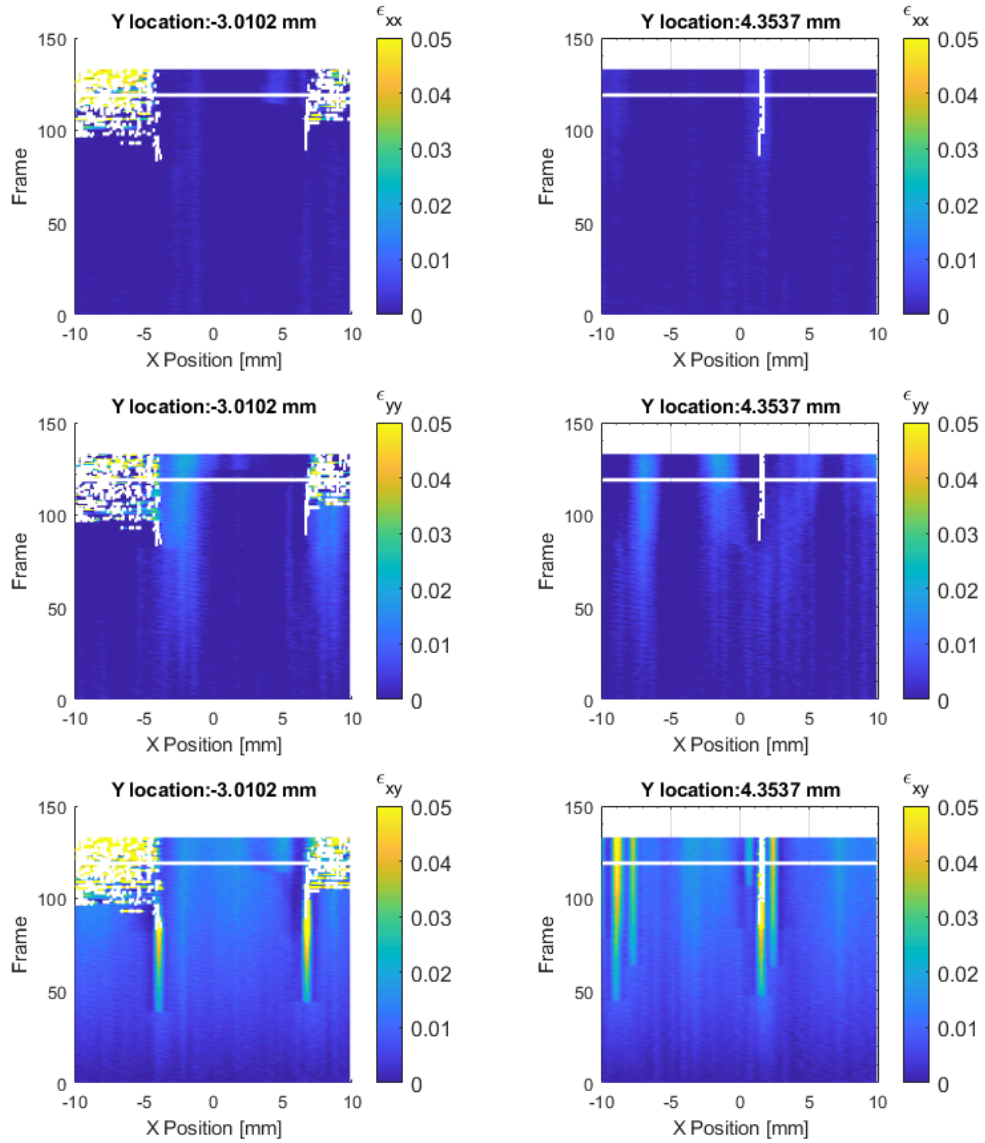
Figure 3.14: Contours of Strain progression using virtual extensometers long the local AOI
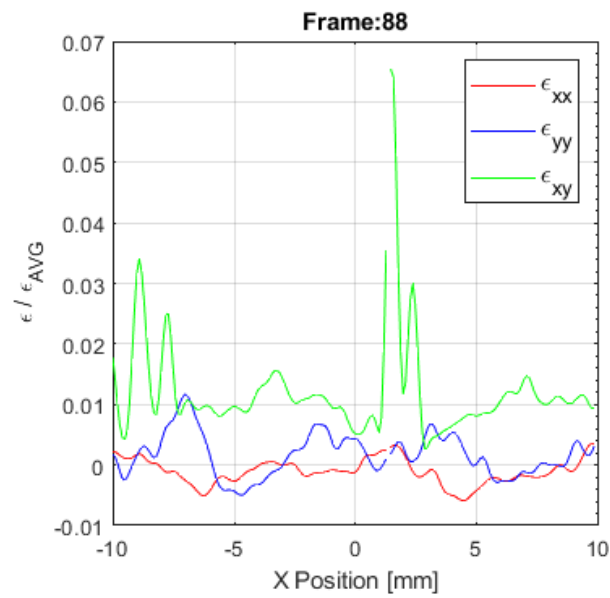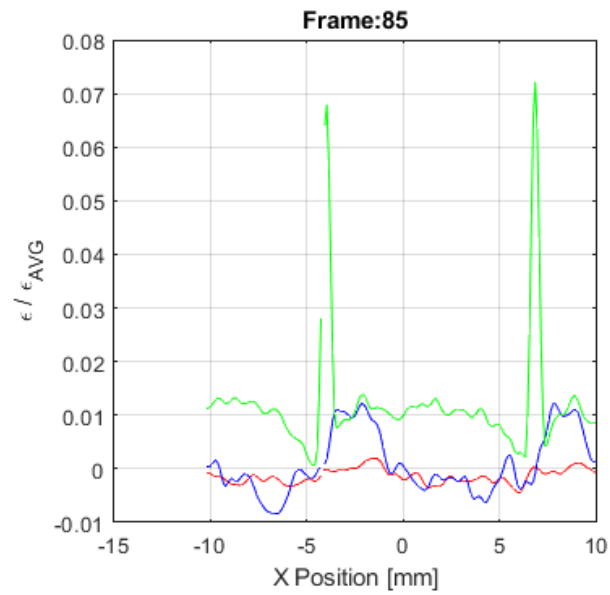
Figure 3.15: Normalized DIC virtual extensometer in-plane strain components before warp tow damage initiation
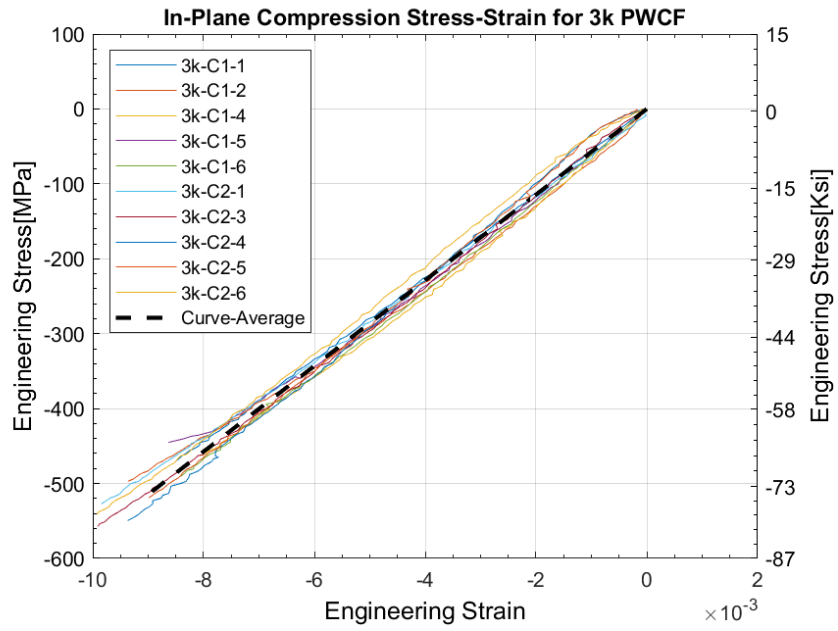
(a)
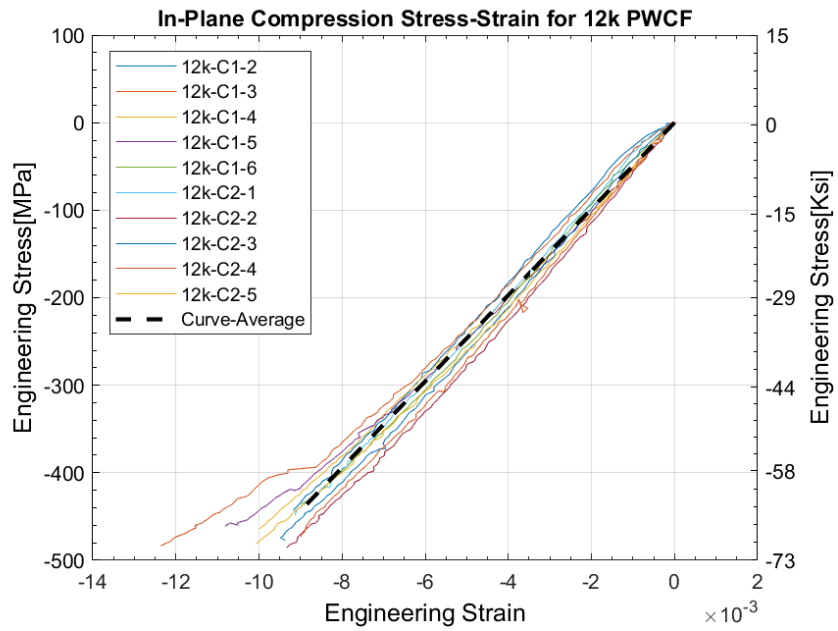
(b)

Figure 3.16: Compression stress strain curves for (a) 3k and (b) 12k PWCF
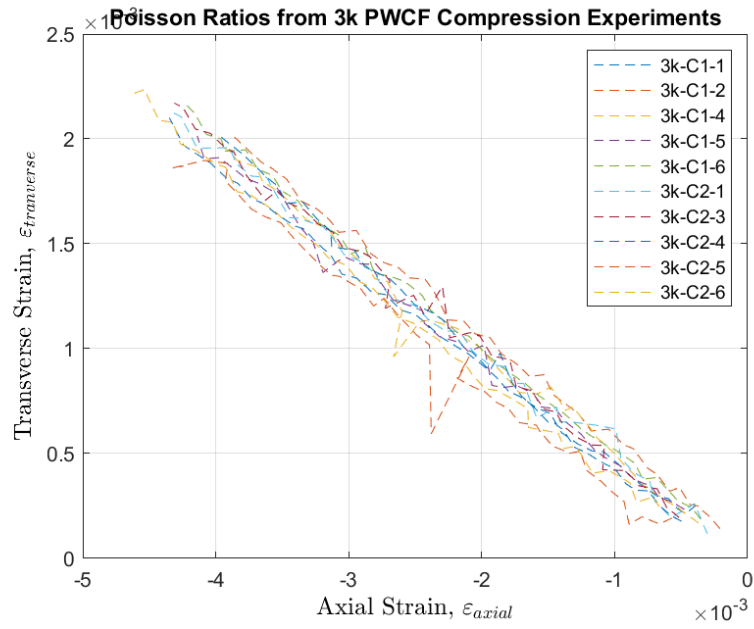
(a)
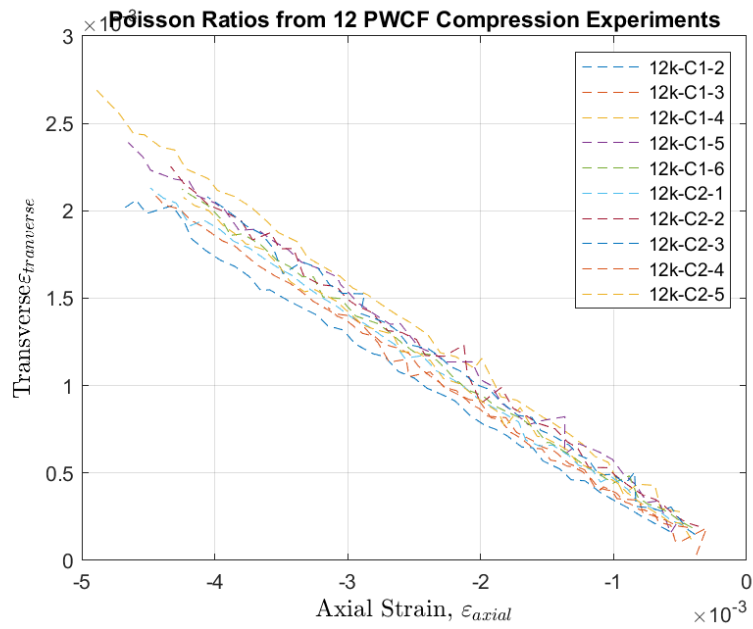
(b)

Figure 3.17: Strain history of axial and transverse in-plane strain from compression using local AOI for (a) 3k material and (b) 12k material

For short beam shear experiments, the AOI is located at the center of the specimen thickness and midway between the top roller and bottom rollers. A rectangular area of 5×2 mm^2 (see Figures 3.9d and 3.10d), which corresponds to roughly 10 $\times$ 6 RUCs and 1 $\times$ 0.5 RUCs for the 3k and 12k materials, respectively, is used to measure strain to obtain stress-strain curves, as shown Figure 3.9d and 3.10d. This location is where the shear strain is high and axial strains are small (in theory, zero bending strain at beam midplane). Both material systems follow similar trends, however, DIC analysis of the 3k short beam shear experiments showed that crack growth at the center of the specimen occurred sooner, likely due to the more voids that were observed during specimen preparation. Summary of the stress-strain curves for short beam shear coupon experiments are shown in Figures 3.18 and 3.19. The peak force is used to determine the end of the stress-strain curves of the short beam shear, due to non-uniform loading occurring at the initiation of damage in the composite, which could occur on the right or left side. The non-symmetric shear strain can be see in the strain history of the short beam shear, Figure 3.20, where the solid green line indicates the right AOI and the marker line shows the left AOI which is initially symmetric but once a transverse strain ,ε_{yy} is seen the loading becomes non-symmetric.
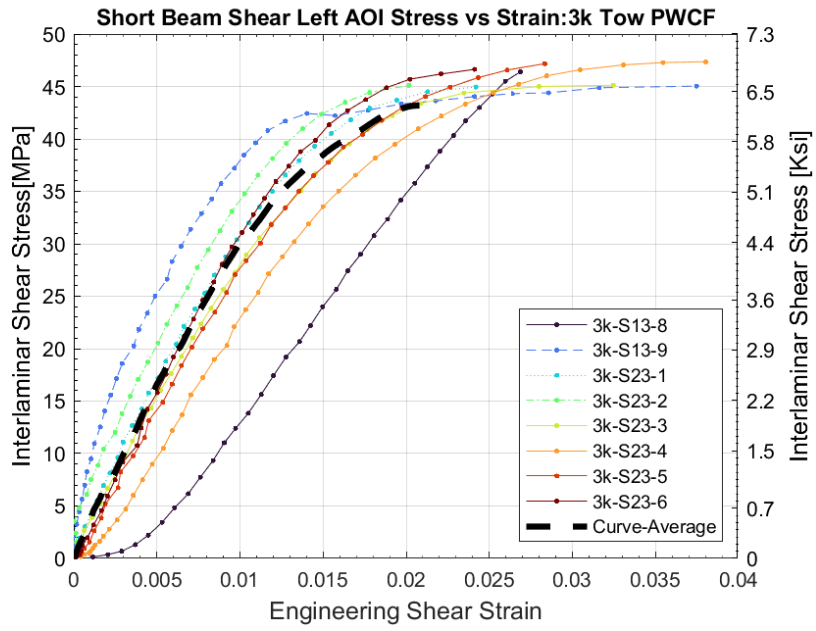
(a)
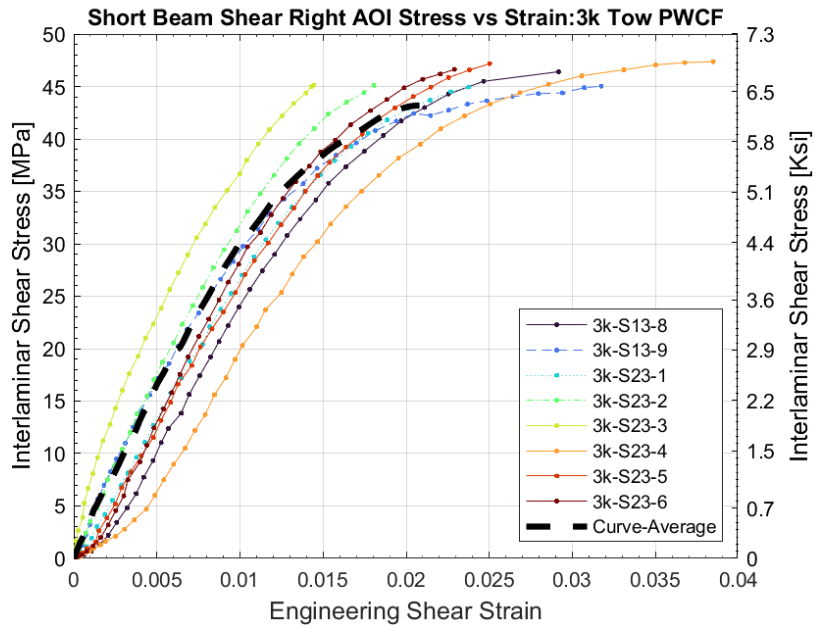
(b)

Figure 3.18: short beam shear stress-strain curves for 3k PWCF using local AOI on (a) left and (b) right side of top roller

55
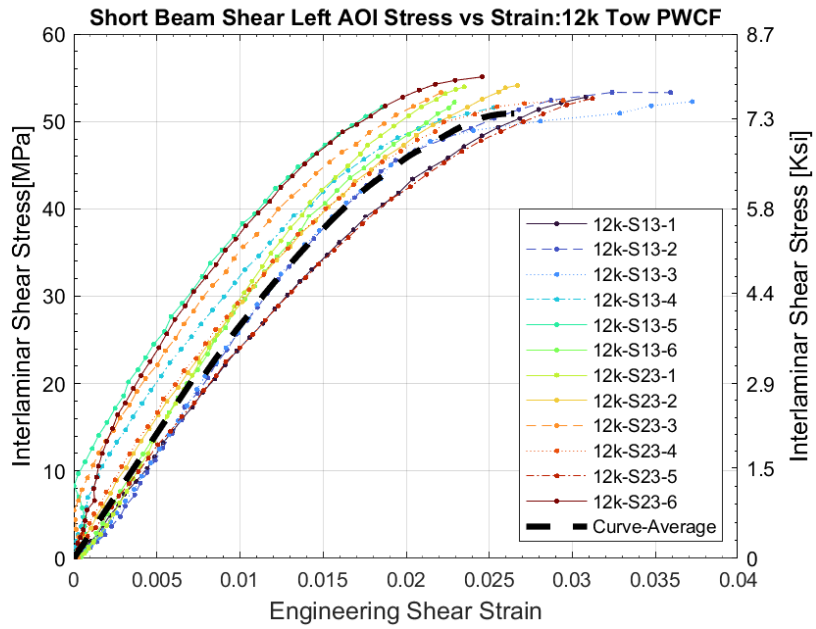
(a)
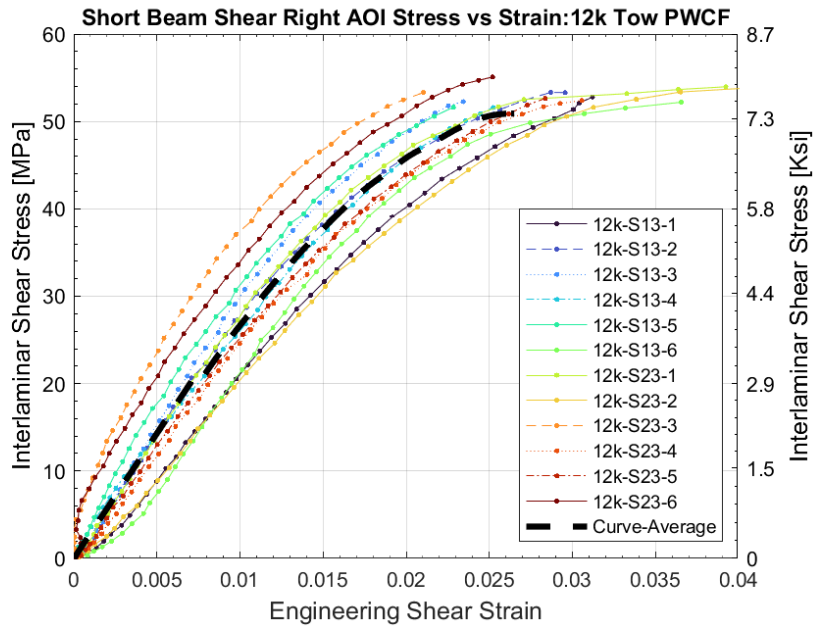
(b)

Figure 3.19: Short beam shear stress-strain curves for 12k PWCF using local AOI on (a) left and (b) right side of top roller

56
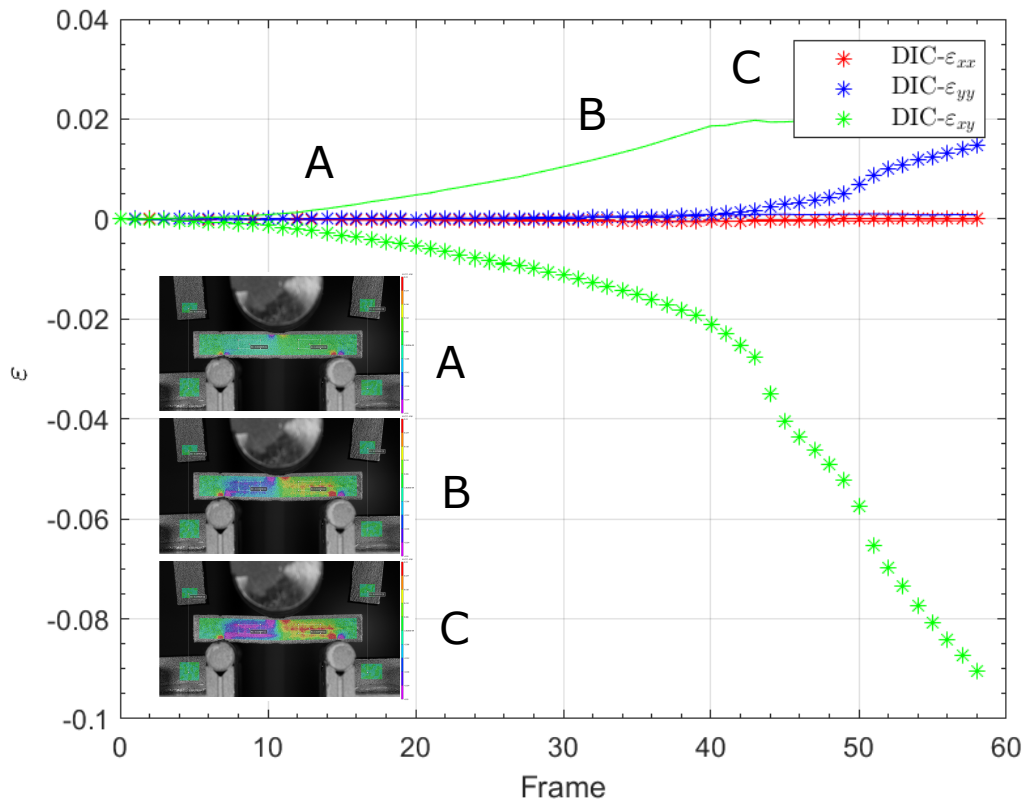
Figure 3.20: Short beam shear strain history of 3k material

For in-plane v-notch rail shear specimens, rectangular areas near the notch tips where zones of high shear strains are concentrated are used to determine stress-strain curves, Figure 3.21a and 3.21b. The areas used for the in-plane shear stress-strain curves are $23 \times 8 \ mm^2$ and $23 \times 11 \ mm^2$, which correspond to roughly 8×2 and 2×1 RUCs for the 3k and 12k material, respectively. DIC speckle size was found to affect the strain measurements. Specifically, it was found that the finer airbrush speckle picked up crack growth at a smaller length scale, which caused the DIC analysis to lose correlation sooner than the coarse speckle. From the DIC analysis of in-plane shear specimens with a fine speckle, cracks were observed near the notches before peak stress. Like the tension experiments, an inhomogeneous strain field was observed (see Figures 3.9c and 3.10c) and tow splitting was observed in the shear experiments. The effect of tow splitting was more significant in the 12k tow material compared to the 3k material due to the large tow and RUC size. The strain history of the local AOI for the 3k and 12k material are shown in Figures 3.22 and 3.23. It is seen that once the strain begins to localize in the middle of the notched area the strain response becomes nonlinear for both 3k and 12k materials. The strain contiues to localize in the notched area with no significant axial or transverse strain observed as seen in Figures 3.22 and 3.23.
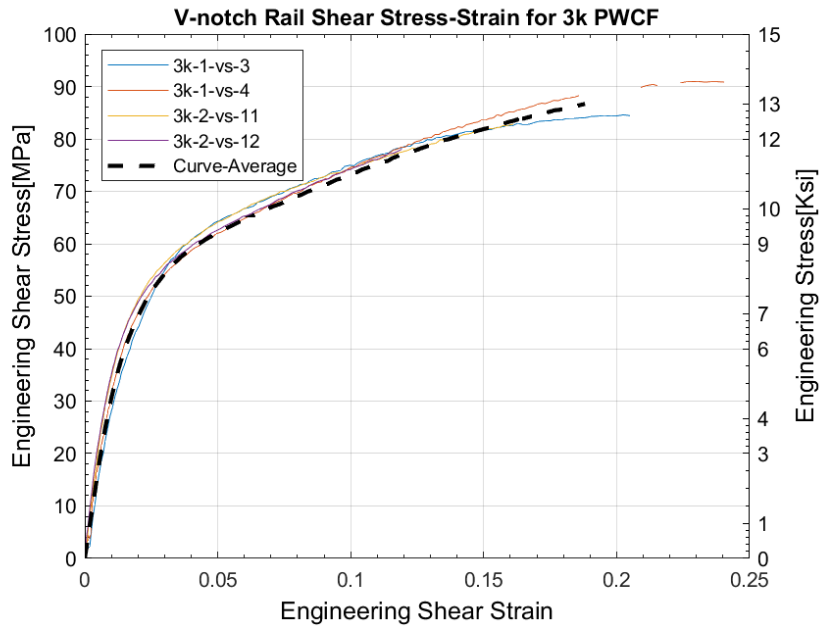
(a)
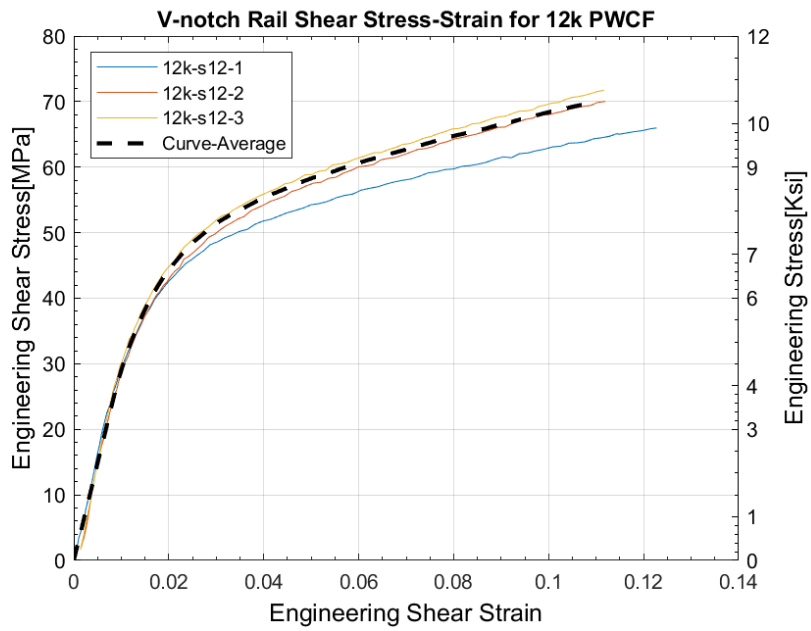
(b)

Figure 3.21: Quasi-static v-notch rail shear stress-strain curves for (a) 3k and (b) 12k PWCF
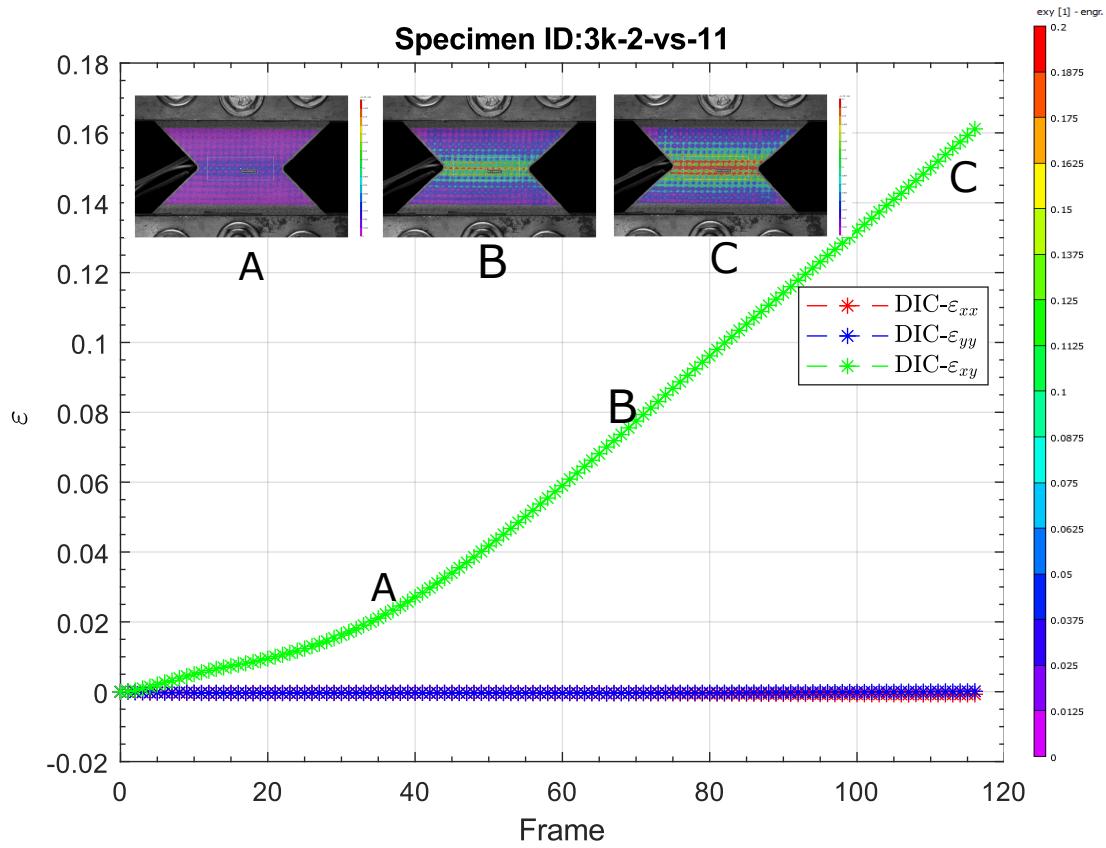
Figure 3.22: V-notch rain shear DIC local AOI strain history for 3k material
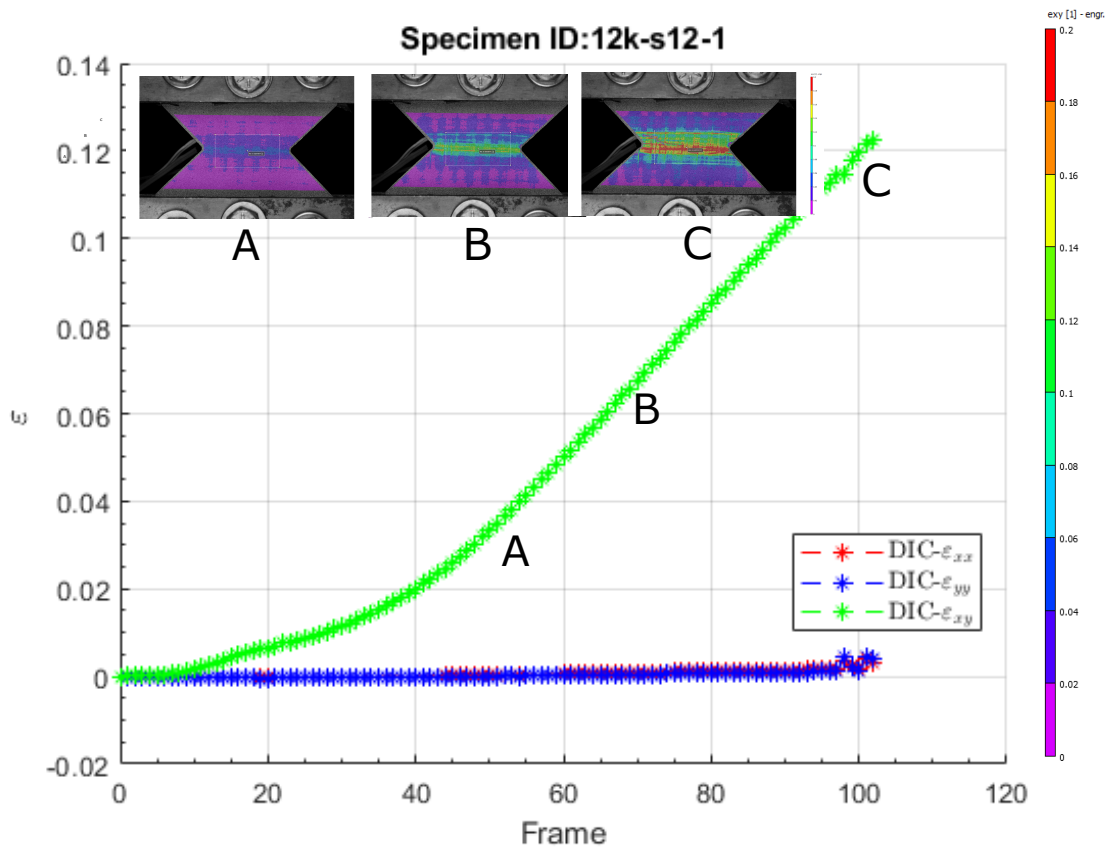
Figure 3.23: V-notch rain shear DIC local AOI strain history for 12k material

3.2 Intermediate Loading of V-Notched Rail Shear

The same fixture half and specimen geometry used in quasi-static v-notch rail shear experiments is used for intermediate loading experiments. Modifications to the top and bottom gripping attachments to account for inertia effects is implemented in the fixture configurations shown in Figure 3.24.
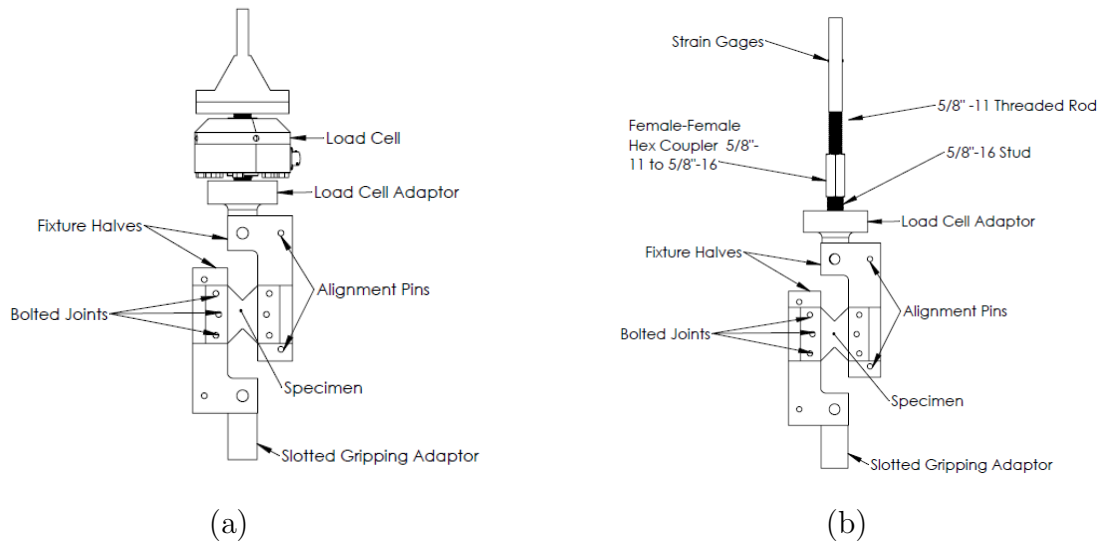
Figure 3.24: V-notch rail shear intermediate loading fixture configurations (a) load cell and (b) half bridge strain gage

3.2.1 Experimental Setup

Experimental testing was performed using a MTS hydraulic load frame with a 22 kip (100 kN) load capacity. A photo and diagram of the experimental setup is shown in Figure 3.25. For quasi-static experiments the axial force from the load cell on the hydraulic frame is used to calculate shear stress using the fixture design in Figure 3.4c. For intermediate loading where the actuator moves at at 3.3 mm/s and 33 mm/s inertial effects must be considered. The hydraulic grips have a significant

mass (30 kg) which will affect the load measurement made by the MTS machine's load cell located above the grips. To accurately measure the load in the specimen, a local load measurement in between the specimen and grips is used to directly measure the force in the specimen. For intermediate experiments the same fixture halves from the quasi-static experiments were used and a modified aluminum adapter allowed either an 12.5 kN Interface load cell to be attached (intermediate version one, Figure 3.24a) a hardened steel rod with two 350 Ω back-to-back strain gages in a half-bridge configuration (i.e. custom built load cell, referred to as intermediate version two), as shown in Figure 3.24b. Additionally, a slotted gripping adapter was needed to provide the bottom grip enough time to accelerate to the desired loading rate [61]. For experiments performed using the quasi-static and intermediate version one configuration (see Figure 3.24a), flat wedges were used for both top and bottom grips. For intermediate version two, the flat grips were used on the bottom and v-serrated grips were used on top to grip the rod (see Figure 3.24b). Specimen pre-loading was performed to help reduced fixture slack and improve alignment. Benefits of using intermediate version 2 (i.e., rod with strain gages) to measure force is that excessive bending stain from fixtures misalignment can be observed and corrected when elastically pre-loading specimen.

For all the DIC analyses, commercially available DIC software, VIC-2D 6, was used to measure 2D surface displacements and strains. For quasi-static tests, images were captured using a Sony α6000 camera with a 105 mm Nikon Micro lens which can record high resolution photo images at 6000 pixels$\times$4000 pixels at 1 frame per second. Camera triggering and synchronization with the test data file was achieved using an Esper TriggerBox which sent a voltage pulse to the camera and data acquisition system at a frequency of 1 Hz. For intermediate loading rates, a Phantom v7.3 high-speed camera with a resolution of 600 px$\times$400 px and the same Nikon 105 mm lens was used to capture images at 2000 fps and 7000 fps. MTS TestWare was used to trigger the high-speed camera by sending to it a voltage pulse which is also recorded
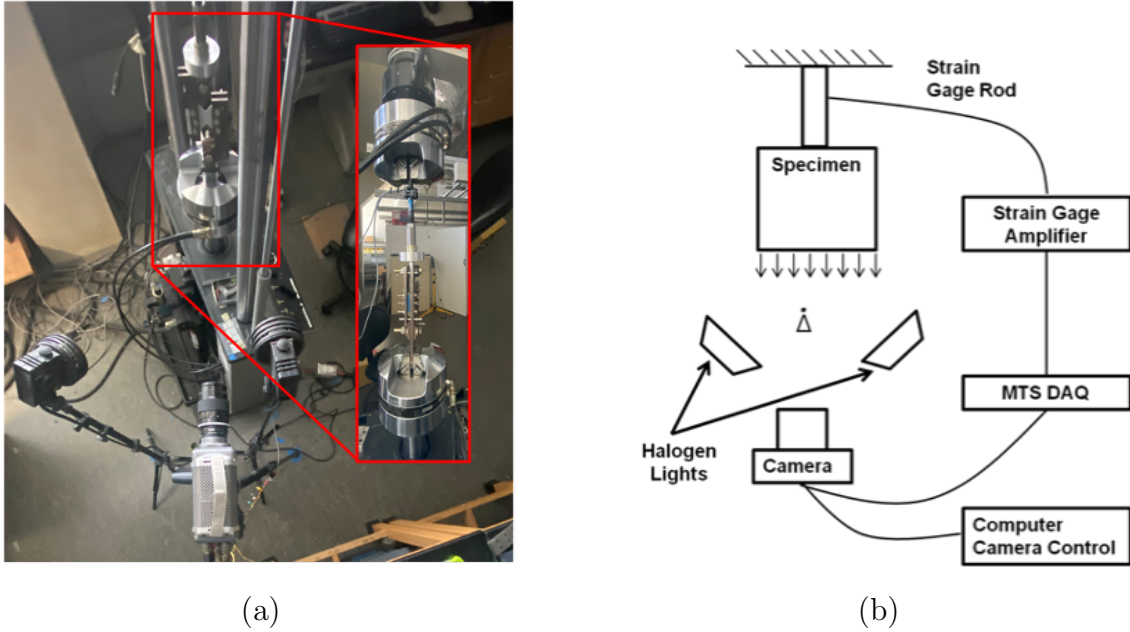
Figure 3.25: Experimental setup (a) image and (b) diagram

in the data acquisition file. DIC analysis used VIC-2D 6 with Gaussian weighted subsets, optimized 8-tap interpolation function, and a zero-mean normalized sum of squared difference (ZMNSSD) correlation criteria. A fine airbrush-created speckle with length roughly 5 to 7 px was used for quasi-static experiments with a high image resolution. Key DIC parameters for VIC-2D 6 are summarized in Table 3.3. For intermediate in-plane shear tests, a coarse speckle length roughly 3 to 4 pixels was created using a black permanent marker pen. When post-processing DIC results, areas of interest (AOI) were defined as shown in Figure 3.7e and 3.7f, with a wider AOI for the 12k material to accommodate the larger RUC size.

3.2.2 Results

A summary of the test matrix of the two woven materials tested at three loading rates 0.033 mm/s, 3.3 mm/s and 33 mm/s is shown in Table 3.4. For in-plane v-notch

Table 3.3: DIC parameters for in-plane shear experiments with VIC-2D 6 software.

Loading Rate	0.033 mm/s	3.3 mm/s	33 mm/s
Camera	Sony	Phantom	Phantom
Camera Resolution	6000 x 4000	600 x 400	600 x 400
Frame Rate (fps)	1	2000	7000
Scale Factor	0.0127	0.119	0.127
Subset Size (px)	35	15	15
Step Size (px)	3	1	1
Strain Filter (px)	9	5	5
VSG (mm)	0.6	2.3	2.4

rail shear specimens, rectangular areas near the notch tips where zones of high shear strains are concentrated are used to determine stress-strain curves, which are plotted for all rates in Figure 3.26. The areas used for the in-plane shear stress-strain curves are 23×8 mm^2 and 23×11 mm^2, which correspond to roughly 8×2 RUCs and 2×1 RUCs for the 3k and 12k material, respectively (see AOI in Figure 3.7e and 3.7f). The end of the stress-strain curve in Figure 3.26 is the ultimate strength which is identified due to a large load drop and the forming of significant matrix damage in the composites. From high speed camera images it was observed that surface cracks propagate parallel to the path of the load develop soon before a large drop in force, as shown in Figure 3.27. Stress-strain curves were obtained till peak stress due to complex stress states that develop due to matrix damage. Additionally, from high speed camera images, damage of the tows near the notch tip lead to the large drop in force which then progresses into failure of the fill tows for materials, Figures 3.27b and 3.27c. Once the fracture begins, large out of plane behavior at the crack region is seen which causes shiny reflections of lighting (negatively affecting the DIC). As shown in Figure 3.27, beyond the load drop, the specimen carries some reduced load while undergoing large deformation unit full separation. This damage onset and load drop (Figure 3.27) is used to determine the limit of stress-strain curve as plotted in Figure 3.26.
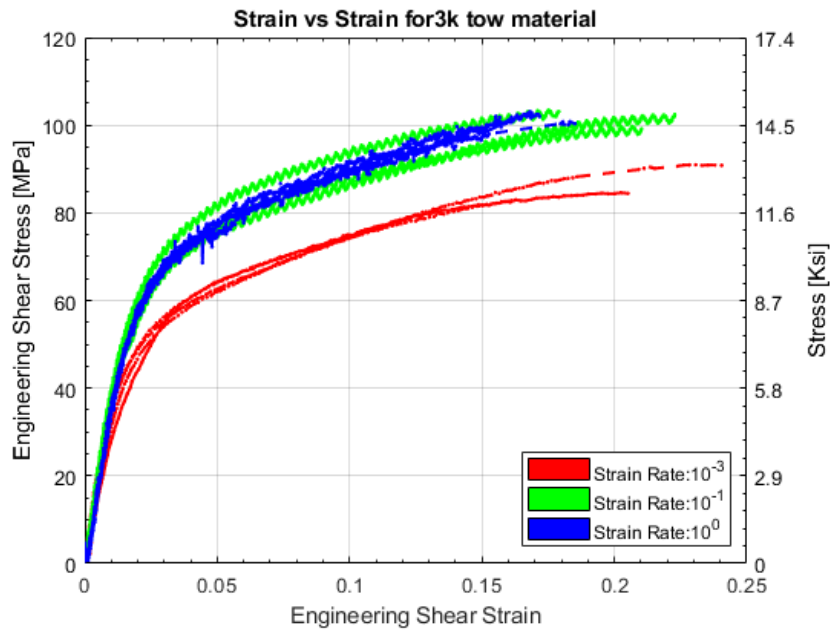
(a)
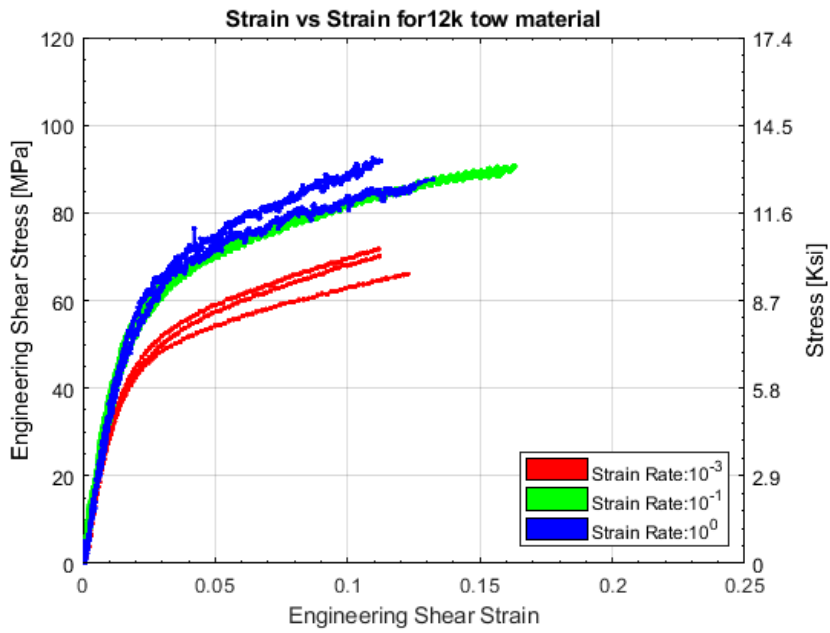
(b)

Figure 3.26: Experimental in-plane shear stress-strain curves at quasi-static and intermediate strain rates (a)3k and (b)12k tow material

Stress History for V-notch Rail Shear
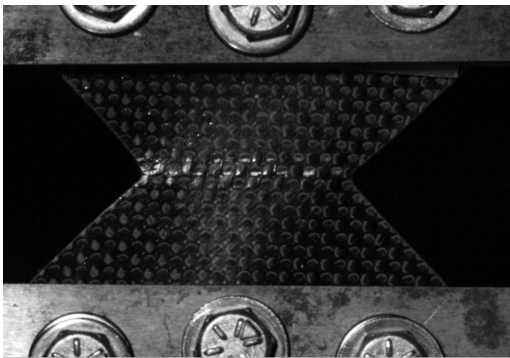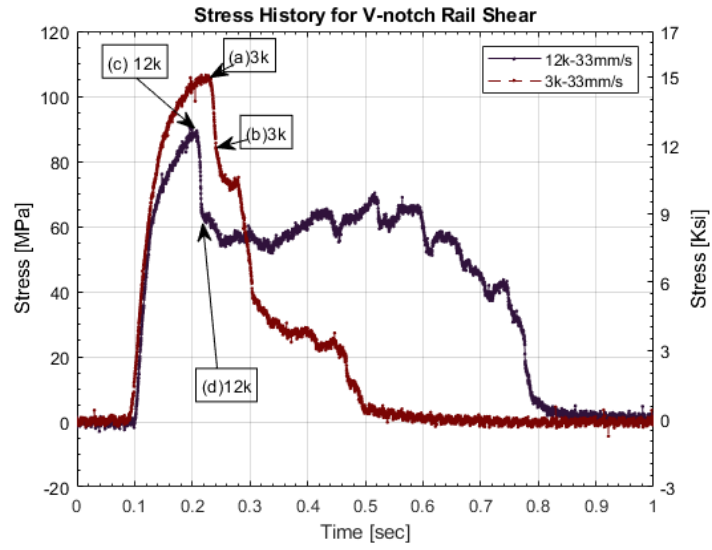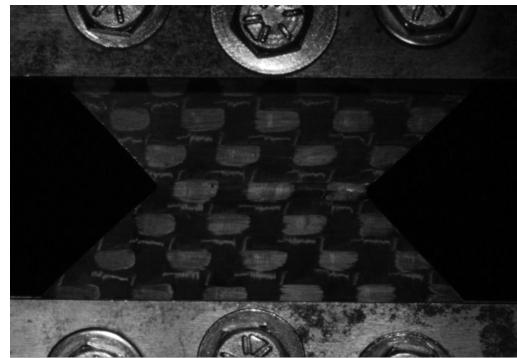
(a) 3k, at peak force

(c) 12k, at peak force

(b) 3k, after load drop

(d) 12k, after load drop

Figure 3.27: Stress history of 33 mm/sec v-notch rail shear with high speed camera images of initial fracture

Table 3.4: V-notch rail shear test matrix.

Material	Loading 0.033 mm/sec	loading 3.3 mm/sec	33 mm/sec
3k PWCF	4	3	3
3k PWCF	3	3	2

Comparing the stress-strain curves in Figure 3.26, for both the 3k and 12k material, the QS rate was significantly different than the intermediate 3.3 and 33 mm/sec rates, which did not show significant differences relative to each other. Both of the fixtures configurations (load cell or strain gaged rod) behaved similarly. The stress-strain curves measured at the highest loading rate follow the same trends as QS curves. Figure 3.28 summarizes the yield and ultimate strength parameters from experiments as well as the shear modulus. Both materials exhibited an increase in yield and ultimate strength with increased strain rate beyond QS, approximately 17-21% for the 3k material and 20-30% for the 12k. Modulus calculations were performed by taking a linear fit between 15-25 MPa. For the 12k material there was a 10 - 20% increase in modulus with increase in rate, while the 3k material showed a 5-8% increase between QS and intermediate rate loading. Specimen yielding is defined as the point where the stress-strain curve deviates greater than 1 MPa from the elastic stress-strain response.

Images of the shear strain contours from DIC, right before correlation is lost in the QS tests(due to damage) and at peak force for intermediate loading rates, is shown in Figure 3.29 for both 3k tow and 12k tow materials. DIC speckle size was found to affect the strain measurements. Specifically, the finer airbrush speckle picked up crack growth at a smaller length scale, which caused the DIC analysis to lose correlation sooner than the coarse speckle. From the DIC analysis of in-plane shear specimens with a fine speckle, cracks were observed near the notches before peak stress. The presence of these cracks was seen in the intermediate loading tests. However, due to the DIC parameters having a lower camera resolution and
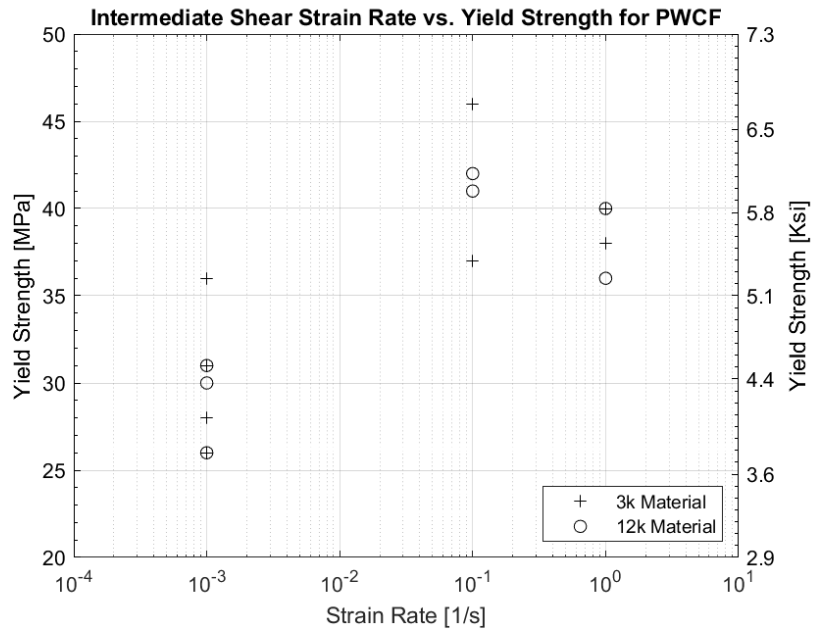
(a)
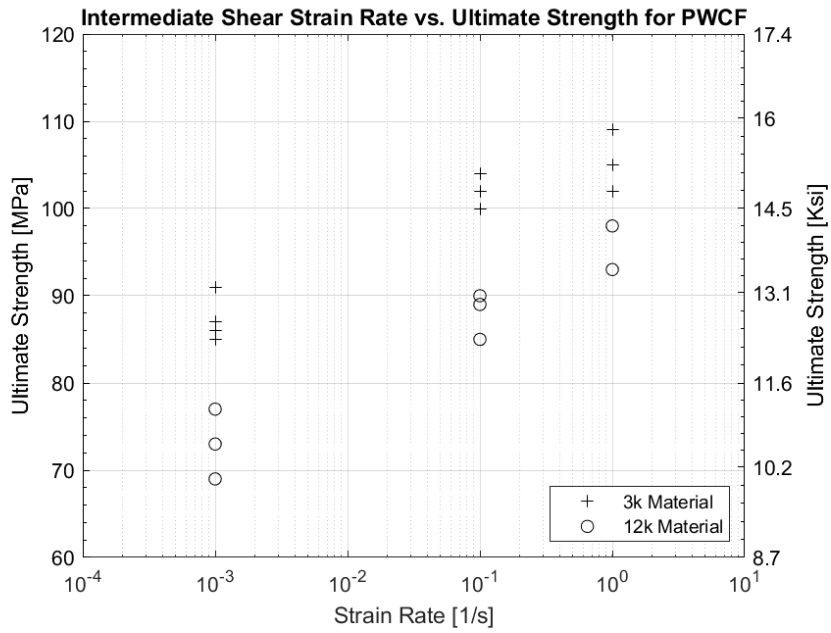
(b)

Figure 3.28: Woven strain rate effects of (a) yield strength and (b) ultimate strength

larger speckle, this did not cause DIC to lose correlation before peak force. For the 3k tow material with high resolution images, a smaller virtual strain gage (VSG) was possible that allows for smaller smoothing regions. A VSG smaller than the width of a tow allowed for a more clear distinction of the non-homogeneous stain fields which can be seen in Figures 3.29a and 3.29b. For intermediate testing that used a Phantom camera with coarse camera resolution (100 times less pixels than images captured with the Sony camera), the coarser camera resolution and speckle size needed for DIC leads to large VSG points. For intermediate tests a VSG size of approximately 2.35 mm was used. This is larger than the width of a tow for the 3k material but smaller than the width for the 12k material. The smoothening in DIC makes it difficult to distinguish the meso-scale tow damage that is observed in the 3k material at intermediate loading rates. The effect of tow splitting was more observable in the 12k tow material compared to the 3k material due to the larger tow and RUC length.

(a)   (b)

(c)   (d)

(e)   (f)
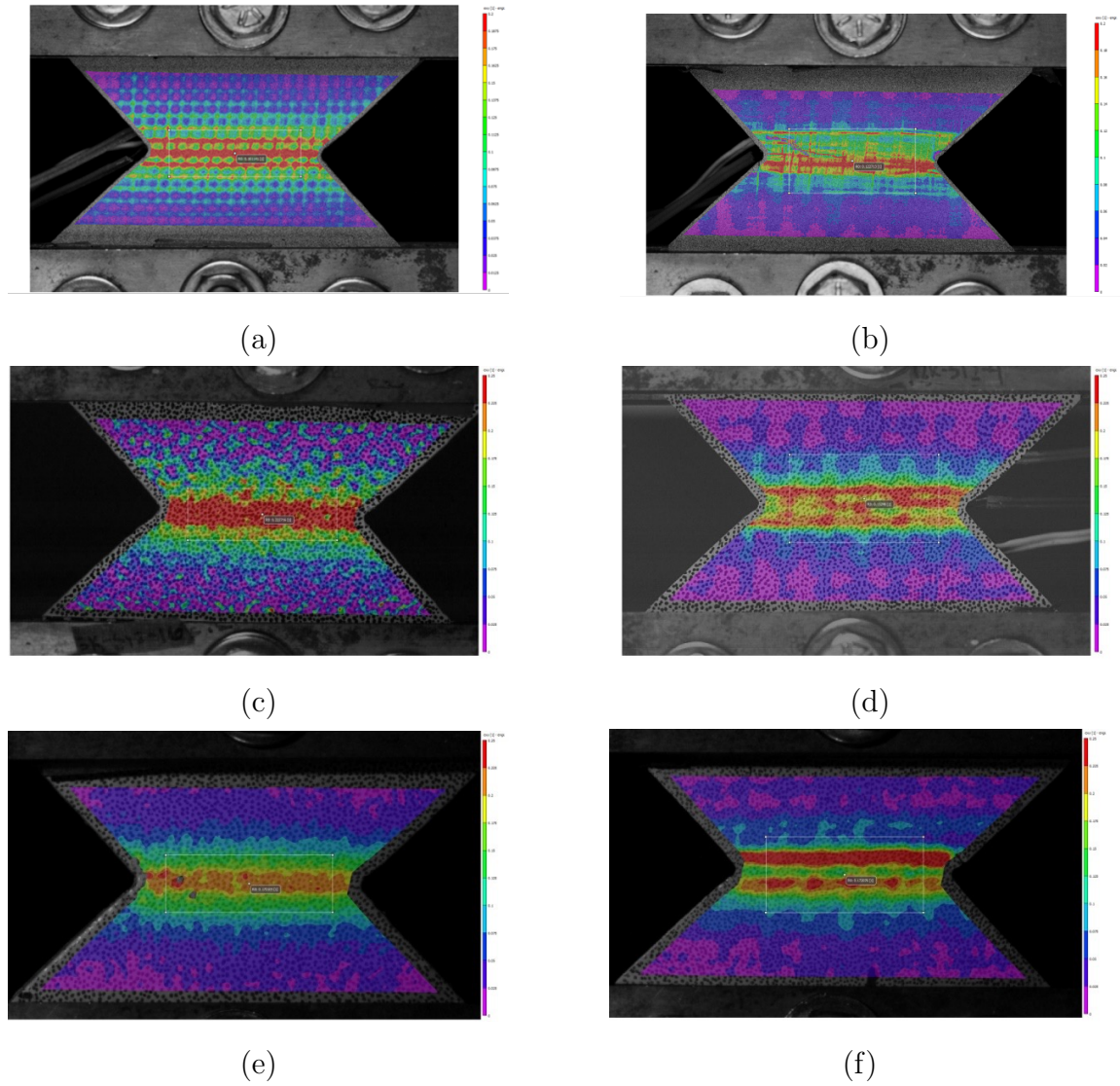
Figure 3.29: Digital Image Correlation (DIC) strain histories for loading rate (a-b) 0.033 mm/s (c-d) 3.3 mm/s and (e-f) 33 mm/s for 3k and 12k material, respectively

3.2.3 Discussion

Comparison of 3k and 12k experiments show more progressive damage in the 3k material due to the RUC size effects relative to the AOI which allows for a large ultimate stress and strain. The point at which initiation of strain localization in the warp tow direction of loading and the progression of strain localization of the warp tows in the 3k material lead to more rapid changes in the post-peak response from high speed camera images. The amount of strain in the specimen is thus dependent on the RUC size. While a larger 12k RUC leads to smaller coupon ultimate strains compared to a smaller 3k tow RUC which allows for progressive damage to occur within the RUC before the entire specimen fails (large load drop post peak), the total energy dissipated by the 12k tow is significantly higher if considering the full area after peak load (see Figure 3.27). The relationship between the mesoscale stress-strain responses of the 12k tow material can be used to investigate tow damage that leads to RUC failure which occurs at the length scale of the coupon. Additionally, the DIC with high speed camera was able to capture inhomogeneous strain fields due to tow damage in the 12k tow material because of the larger tow size. To better assesses the damage that develops before the peak stress, further developments of the fixture and test method are needed to allow the specimen to maintain a uniform load. Low cycle fatigue damage experiments are also needed to better understand the stiffness reduction due to damage accumulation. This would help to determine the relationship between the extent of damage in the meso-scale tow and marco-scale RUC progressive damage response.

Chapter 4

Hybrid Experimental and Numerical Characterization of the 3D Response of Woven Polymer Matrix Composites

The following work has been presented and published at American Society for Composites Technical Conference and is a collaborative effort with NASA Glenn Research Center that provided techicanl guidance and software tools for analysis. It is in preparation for journal publication.

A hierarchical hybrid experimental-numerical methodology to efficiently characterize the rate dependent stress-strain curves of new materials for tabulated or data driven composite material simulations is shown in Figure 4.1. This work consists of experimental and numerical techniques. Work will contribute to understanding of MAT213 capabilities to model woven materials. For this methodology, first the characterization of the repeating unit cell (RUC) serves as a basis for the experimental specimen design to efficiently characterize the material behavior as illustrated in

Table 4.7. Additionally, the RUC characterization is used as inputs for micromechanics analysis using NASA Glenn MAC/GMC. A plain weave RUC from previous works, Figure 2.3, is chosen because of computational efficiency and accuracy. Next, investigation of the fiber volume fraction is used for in calibration of virtual curves by comparing experimental modulus values. Additionally, calibration of a viscoplastic polymer model is done using experimental in-plane shear coupon experiments from Section 3.2. Focus on calibration of the in-plane shear loading is done due to having the largest nonlinearity in woven composites. Lastly, a max stress criterion using constituent properties from [84] is applied to obtain predictive virtual curves for the through-thickness direction. Validation of this methodology and its applicability for woven composites materials using a tabular material model, MAT213, is performed through single element and coupon FEA verification with two different woven RUCs. Additionally, validation studies of an adhesively bonded composite wingbox structure subjected to low velocity impact is simulated and compared with experimental tests.
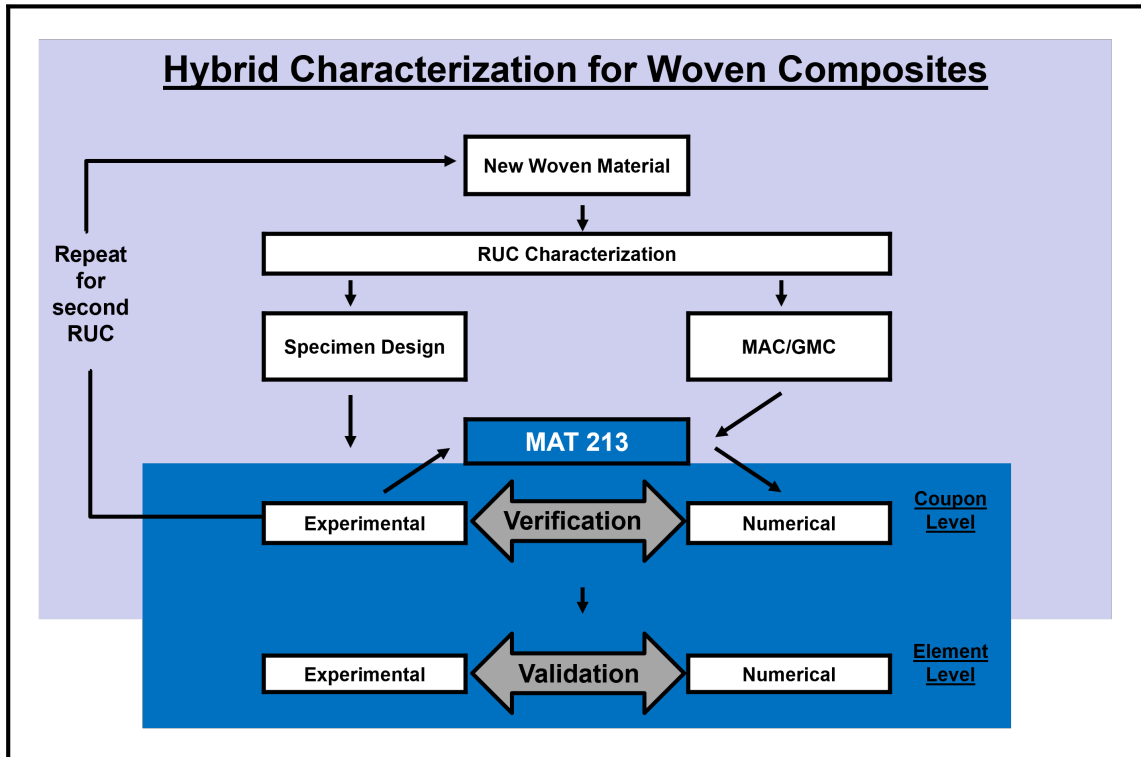
Figure 4.1: High level flow chart of hybrid characterization methodology for woven composites

4.1   Repeating Unit Cell Characterization

Tow measurements were performed from a large plate to get an average value of tow width and the ply thickness. Additionally, image processing software, ImageJ, was used to measure tow parameters from microscope images, as seen in Figure 4.2. Weave geometric parameters are summarized in Table 4.1 and illustrated in Figures **??** and 4.3. Microscope images had an average tow thickness and width of 0.1 mm and 1.55 mm, and 0.17 mm and 4.3 mm for the 3k and 12k material, respectively. These measured values from microscope images and bulk materials lengths are used as areas for a Matlab routine that uses the Image Processing Toolbox to automate visualization of tow, as seen in Figure 4.4. A large variation in the tow width is seen in Figure 4.4 which is due to inherent imperfections in the weave and manufacturing process that leads to resin rich areas, tow splitting, or tow nesting that causes variations in the tow geometry. Additionally, since 2D images are used to measure the 3D geometry of the weave changes in the tow are not capture with a single image slice. The width, thickness and undulation angle in the weave vary depending on the weave slice being measured.

(a)   (b)
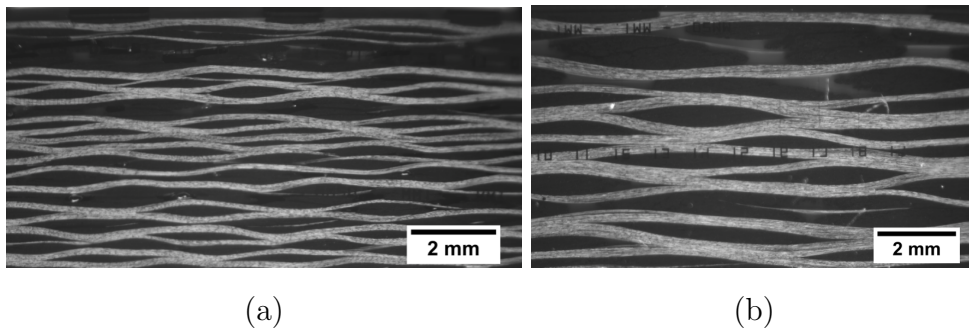
Figure 4.2: Optical microscope images of (a) 3k tow and (b) 12k tow

Table 4.1: Balanced plain weave tow parameters

Parameter	Hexcel-282 Fiber	Toray-T700 Fiber
n_f, Filament count, thousands	3	12
d_{fiber}, Fiber diameter, μm	7	7
h, Ply thickness, mm	0.2	0.33
t_t, Tow thickness, mm	0.1	0.167
w_t, Tow width, mm	1.55	4.30
g_t, Tow gap, mm	0.51	1.35
s_t, Tow spacing, mm	2.06	5.65
RUC dimensions, mm x mm x mm	4.12 X 4.12 X 0.2	11.3 X 11.3 X 0.33
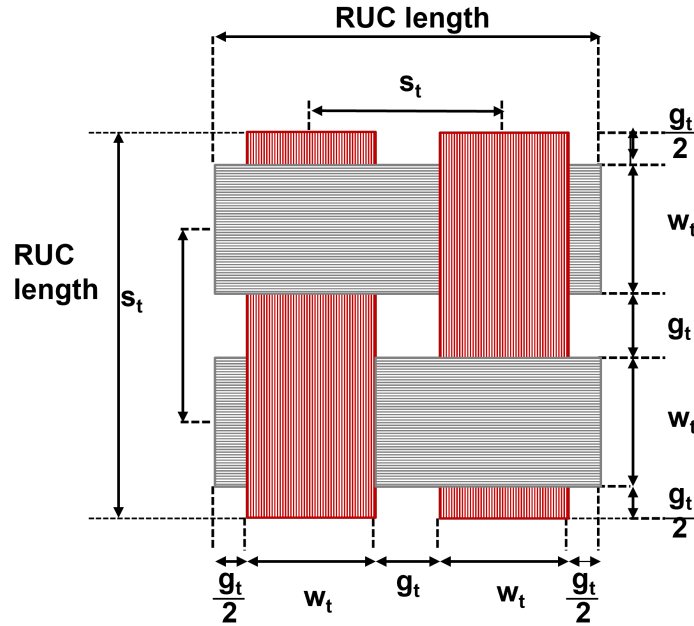
Figure 4.3: Top View of plain weave RUC. Adapted from [8].
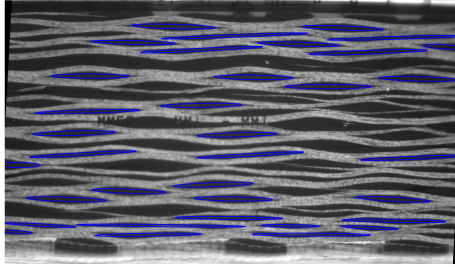
(a) 3k
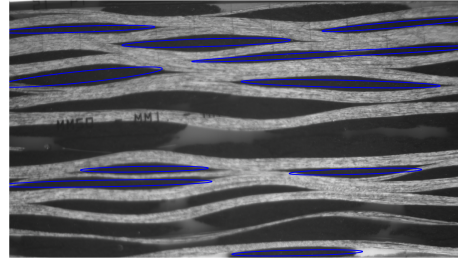
(b) 12k
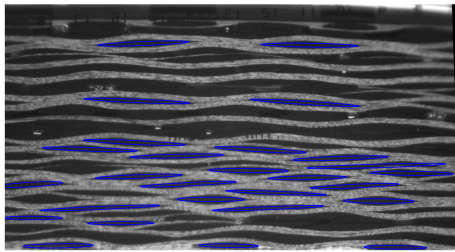
(c) 3k
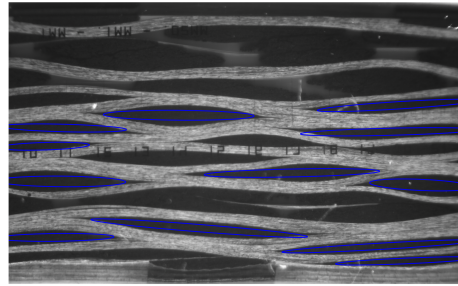
(d) 12k
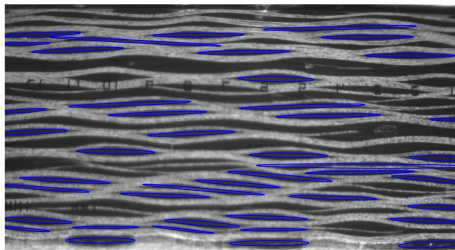
(e) 3k
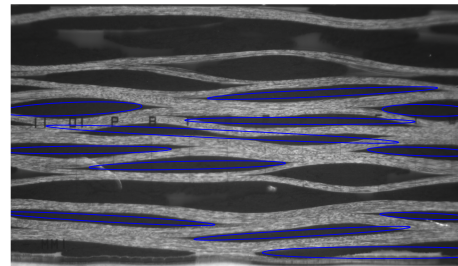
(f) 12k

Figure 4.4: Elliptical tow finder overlay with optical microscope images for 3k and 12k plain weave carbon fabrics.

The tow fiber volume fraction for both materials is calculated using Equation 4.1 from Cox 1997 [8]. The cross section of the tow is assumed to be rectangular. The measured tow parameters gives only a slice of the material geometry. In reality the tow area does not remain constant and is not rectangular but elliptical as seen in Figure 4.2.

$$V_{f,tow} = \frac{n_f(\frac{\pi}{4}d_{fiber}^2)}{t_t w_t} \tag{4.1}$$

Additionally, the fiber volume fraction of the bulk composite materials was calculated using Equation 4.2 following ASTM D792-00 [23] to measure mass density of the final composite plate and using constituent densities provided by the supplier.

$$V_{f,RUC} = \frac{\rho_c - \rho_m}{\rho_f - \rho_m} \tag{4.2}$$

Where ρ_c, ρ_f, ρ_m are the density of composite, fiber and matrix, respectively. The fiber and matrix densities are 1.8 g/cm^3 and 1.09 $\frac{g}{cm^3}$, respectively. Table 4.2 summarizes density measurements of both woven materials for three different manufactured plate thicknesses. Averaged measured composite density for the 3k and 12k are measure as 1.448 $\frac{g}{cm^3}$ and 1.428 $\frac{g}{cm^3}$. Composite densities are used with Equation 4.2 to calculate fiber volume fraction at the RUC level which is summarized in Table 4.3. The 3k material had a larger fiber volume fraction, 50.4% compared to the 12k material, 47.7% following ASTM D792-00.

The relationship between the RUC fiber volume fraction to the tow fiber volume fraction of the plain weave RUC from [21] is used to compare different techniques of measuring fiber volume fraction using Equation 2.17. The optical microscope technique which measured meso-scale tow parameters to calculate RUC volume fraction resulted in a larger fiber volume fraction compared to ASTM D792-00. This is seen in both 3k and 12k materials which is summarized in Table 4.4. The presence of voids as well as resin rich areas are better captured using ASTM D792-00 which provides a better measurement of the composite volume. Whereas the microscope images

assume that the behavior of the composite at a single slice is the same throughout the composite.

Table 4.2: Density measurements for plain weave carbon fabrics.Note: units are in $\frac{g}{cm^3}$

Material	Plate 1	Plate 2	Plate 3	Average $\pm$ Standard Deviation
3k	1.457	1.460	1.426	1.448 $\pm$ 0.019
12k	1.426	1.422	1.4368	1.428 $\pm$ 0.007

Table 4.3: Fiber volume fractions of three different thickness plates calculated from composites densities for 3k and 12k plain weave carbon fabric materials.

Material	Plate 1	Plate 2	Plate 3	Average $\pm$ Standard Deviation
3k	0.517	0.522	0.473	0.504 $\pm$ 0.027
12k	0.474	0.468	0.488	0.477 $\pm$ 0.011

Table 4.4: Fiber volume fraction comparison of 3k and 12k plain weave carbon fabrics

	3k, $V_{f,tow}$	3k, $V_{f,RUC}$	12k, $V_{f,tow}$	12k, $V_{f,RUC}$
ASTM D792	0.652	0.504	0.634	0.477
Optical Microscope	0.744	0.56	0.651	0.49

4.2　Micromechanics Analysis

Micromechanics analysis for both 3k and 12k materials used tow parameters and elastic properties from Tables 4.1 and 4.5. The reinforcing fibers are modeled as linearly elastic and transversely isotropic. Elastic properties from the supplier are used and unknown elastic properties of the constituents were assumed using similar fibers and epoxies from Daniel and Ishai [23] which are summarized in Table 4.5. Since a balanced plain weave carbon fabric is being investigated both warp and fill tows are assumed to have the same geometry and material properties. Additionally, the undulation angle for the plain weave was set to zero. This was done because the fidelity of the RUC used does not have continuous fiber geometry or allow for update to undulation angle as loading progresses. Next, the rate-dependent experimental in-plane shear stress-strain curves were used to calibrate n, the rate-dependent parameter in the viscoplastic polymer model (see Equation 4.4). Lastly, an optimization scheme using root mean square error (RMSE), like Murthy et al. [85], was created in Matlab to find the remaining viscoplastic parameters, which are summarized in Table 4.6.

Table 4.5: Constituent elastic parameters

Parameter	Fiber	SC-780 Epoxy
Density g/cm^3	1.8	1.09
E_a, Axial Modulus, GPa	228	2.9
E_t, Transverse Modulus, GPa	15	2.9
ν_a, Axial Poisson's Ratio	0.2	0.35
ν_t, Transverse Poisson's Ratio	0.2	0.35
ν_t, Shear Modulus, GPa	27	0.35

Table 4.6: Viscoplastic polymer parameters

$D_0(1/s)$	n	q	$Z_0(MPa)$	Z_1 (MPa)	α_0	α_1
10^6	0.57	16.32	22	45	0.00025	0.00025

4.2.1 Volume Fraction Calibration

A comparison of the modulus obtain experimentally and through micromechanics analysis using tow volume fractions obtain from microscope images and through ASTM D792-00, are shown in Figures 4.5a and 4.5b for the 3k and 12k materials, respectively. For in-plane tension, in-plane compression, in-plane shear, and short beam shear, the experimental modulus values were found using a linear fit between 50-200 MPa, 100-300 MPa, 10-25 MPa, and 10-25 MPa, respectively. For the 3k material, the tensile and compressive response of the calibrated MAC/GMC analysis behaved linearly to failure and stiffer compared to the experimental stress-strain curves for both volume fractions, as seen in Figure 4.8a and comparing the modulus value from Figures 4.5a. This is because the undulation angle was set to zero, which caused a stiffer response. A similar trend was seen with the in-plane tension experiments for the 12k material where the MAC/GMC response behaved stiffer compared to the experimental response. This response, however, follows the linear portion of the experimental stress-strain curve more closely than the 3k material but does not capture the nonlinear behavior near failure. When using the tow fiber volume fraction that was obtain from ASTM D792-00 the response better matches the experimental tension and compression curves as shown in Figures 4.8a and 4.8b for the 3k material and Figures 4.9a and 4.9b for the 12k material. For the 3k and 12k material, the in-plane shear modulus shown in Figure 4.5. MAC/GMC analysis matches the experimental shear curves well under small strain, however, when the strain becomes larger the stress-strain response begins to deviate shown in Figures 4.8c and 4.9c, for the 3k and 12k materials. The experimental shear modulus compared well with MAC/GMC values for both tow volume fractions, Figure 4.5.
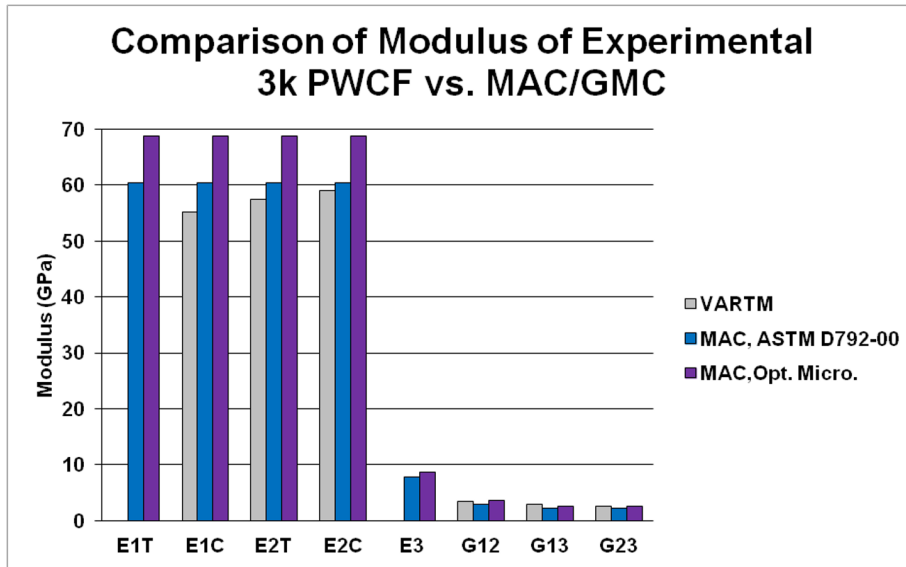
(a)
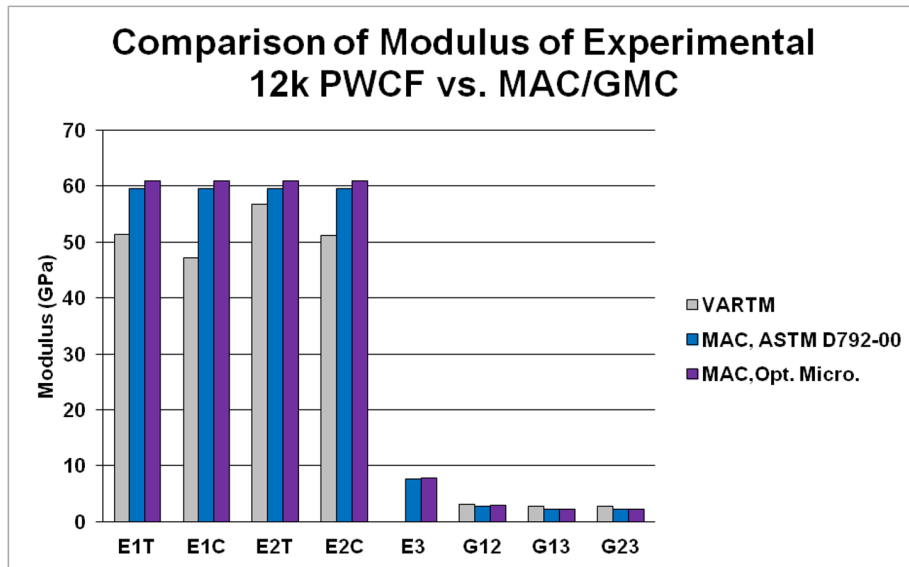
(b)

Figure 4.5: Comparison of experimental modulus from VARTM vs. MAC/GMC for (a) 3k and (b) 12k material

4.2.2 Rate Calibration

It has been observed that polymers are strain rate-sensitive [14, 24]. Therefore, rate-dependent material models are needed to characterize this response. A modified Bodner-Partom (BP) viscoplasticity model, which is typically used for metals, has been used to characterize the viscoplastic polymer response using neat resin data at various loading rates [22, 86]. A detailed procedure about the characterization is found in Goldberg et. al [87]. The main parameters are described in the following equations.

$$f = \sqrt{J_2} + \alpha\sigma_{kk} \tag{4.3}$$

$$\dot{\varepsilon}_{ij}^I = \dot{\lambda}\frac{\partial f}{\partial \sigma} = 2D_0 exp\left[-\frac{1}{2}\left(\frac{Z}{\sigma_e}\right)^{2n}\right]\left(\frac{S_{ij}}{2\sqrt{J_2}} + \alpha\delta_{ij}\right) \tag{4.4}$$

In the inelastic potential function, Equation 4.3, J_2 is the second invariant of the deviatoric stress tensor, σ_{kk} is the hydrostatic stress and α is a state variable used to account for hydrostatic stress effects. An associative flow rule, Equation 4.4, is used to determine the inelastic flow where $\dot{\lambda}$ is a scalar rate variable, D_0 is a constant scale factor that represents the maximum inelastic strain rate, σ_e is the effective stress defined in Equation 4.5, S_{ij} are the components of the deviatoric stress tensor, and δij is the Kronecker delta.

$$\sigma_e = \sqrt{3}f = \sqrt{3J_2} + \sqrt{3}\alpha\sigma_{kk} \tag{4.5}$$

The isotropic internal stress state variable Z and mean stress effect state variable α evolve depending on q which is the material hardening rate, Equations 4.6 and 4.7. Z_1 and α_1 represent the maximum values of Z and α. The initial values of Z and α are defined by the material constants Z_0 and α_0. The term $\dot{e}_e^I$ represents the effective deviatoric

84

$$\dot{Z} = q \left(Z_1 - Z \right) \dot{e}_e^I \tag{4.6}$$

$$\dot{\alpha} = q \left(\alpha_1 - \alpha \right) \dot{e}_e^I \tag{4.7}$$

The experimental in-plane shear curves from Section 3.2 are compared with the calibrated the visco-plastic polymer model Figure 4.6. At quasi-static (QS) loading, 10^{-3} s^{-1}, the initial elastic portion matches the virtual curves for both 3k and 12k materials, Figures 4.6a and 4.6b. Additionally at QS loading, the nonlinear trend is captured, however, for the 3k material the virtual curve under predicts the first hump and does not reach the same max stress as the experiments. Similarly, at QS the 12k material the first hump is under predicted in the virtual curve. The max stress at QS for the 12k material does compared to the experimental tests. At the first intermediate loading rate, 10^{-1} s^{-1}, the initial nonlinear portion of the curve is under-predicted similar to the QS curves for both 3k and 12k materials. The end of the curve near max does compare better with experimental curves at 10^{-1} s^{-1} versus 10^{-3} s^{-1} for the material.

Lastly, at the fast loading rate, 10^0 s^{-1}, the initial nonlinear hump is better capture compared to the 10^{-3} s^{-1} loading for both materials. Additionally, the end of the virtual curve follows the same trend as the experiments but slightly over predicts the max stress, Figures 4.6e and 4.6f. From intermediate shear experiments, no significant difference was observed between $10^{-1}s^{-1}$ and 10^0 s^{-1}. Whereas, in the micromechanics analysis does show changes in the loading rate between 10^{-1} s^{-1} and 10^0 s^{-1}. Overall, the virtual curves did match well with experimental curves for the calibrated rate parameter, n. Sensitivity of this parameter is shown in Figure 4.6 that shows an decrease (shown in red) and a increase (shown in green) of the rate parameter value from Table 4.6. From this it can be seen, that calibration of this parameter is important to capture the nonlinear rate dependent behavior in woven polymer matrix composites.
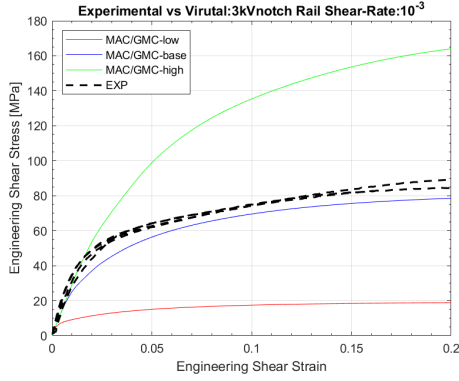
(a) 3k loaded at 10^{-3} s^{-1}
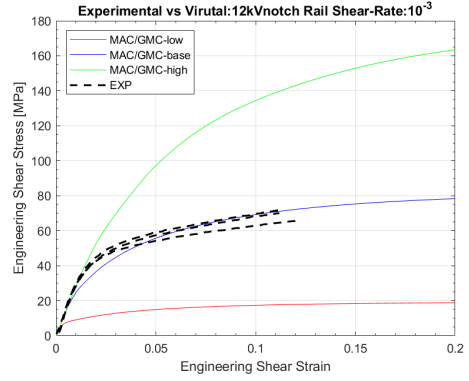
(b) 12k loaded at 10^{-3} s^{-1}
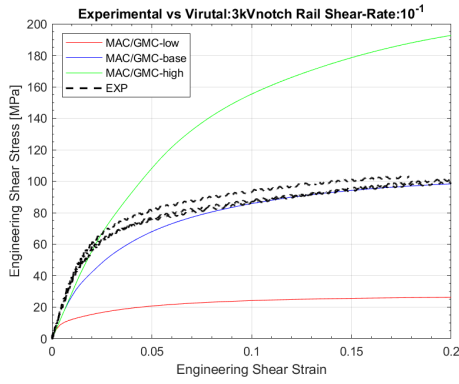
(c) 3k loaded at 10^{-1} s^{-1}

(d) 3k loaded at 10^{-1} s^{-1}

(e) 3k loaded at 10^{0} s^{-1}

(f) 3k loaded at 10^{0} s^{-1}

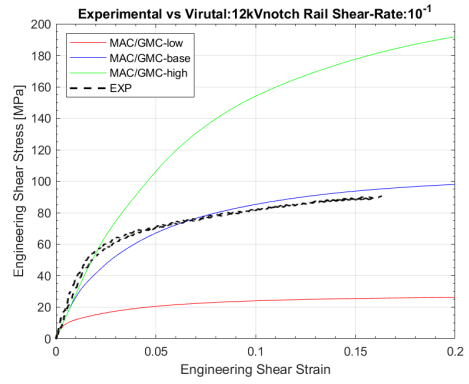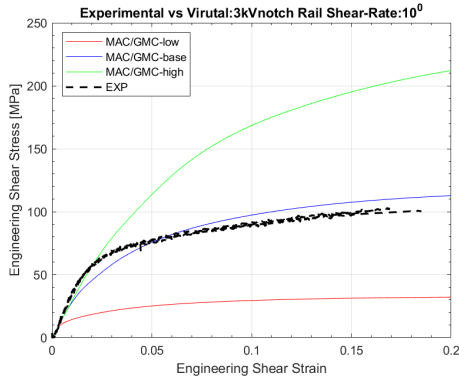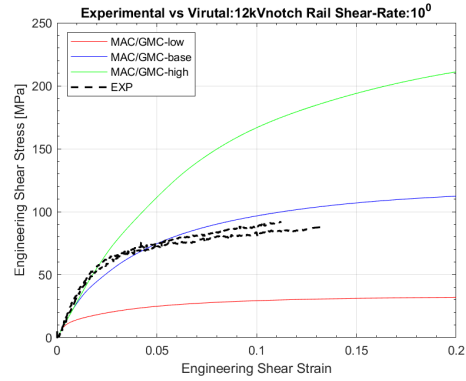Figure 4.6: Sensitivity of rate parameter, n, compared with 12k tow in-plane shear experimental results at rate three loading rates.

86

Once the rate dependence is calibrated the addition of subcell failure using constituent stress allowables from [84] with IM7 and 8552 properties for the fiber and matrix, respectively. Comparison between the experimental tension, compression, v-notch shear, and short beam shear at QS loading from Section 3.1. For the 3k material the strength for in-plane tension and compression was over predicted compared to the experimental strengths using both the tow fiber volume fraction from microscope images and ASTM D792-00, as shown in Figures 4.7 and 4.8. The tensile strength for the 3k using the tow fiber volume fraction from microscope images over predicted the strength by 55%, whereas, using the tow fiber volume fraction from ASTM D792-00 the strength is over predict by 34%. For the 12k material an average of the 1-direction and 2-direction strength are compared with MAC/GMC which showed an over predicted strength of 32% and 27% with microscope and ASTM D792-00 tow fiber volume fraction, respectively. Similarly, the compression strength is over predict by 48% and 30% for the 3k material and 44% and 41% for the 12k material. As for the short beam shear experiments for the 3k material, it was noted that voids were present in the 3k material, which lead to early failure. This can be seen by comparing the lower interlaminar shear strength of the experiments and similar materials from the literature.

Overall, MAC/GMC is able to match available experimental. Additionally, predictive virtual curves in the through thickness tension and compression direction are shown in Figure 4.10.
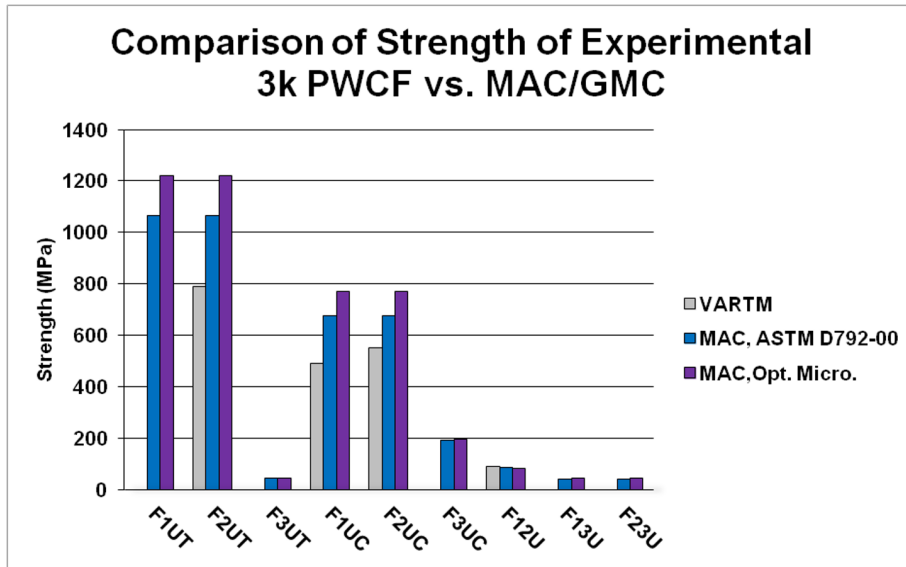
(a)
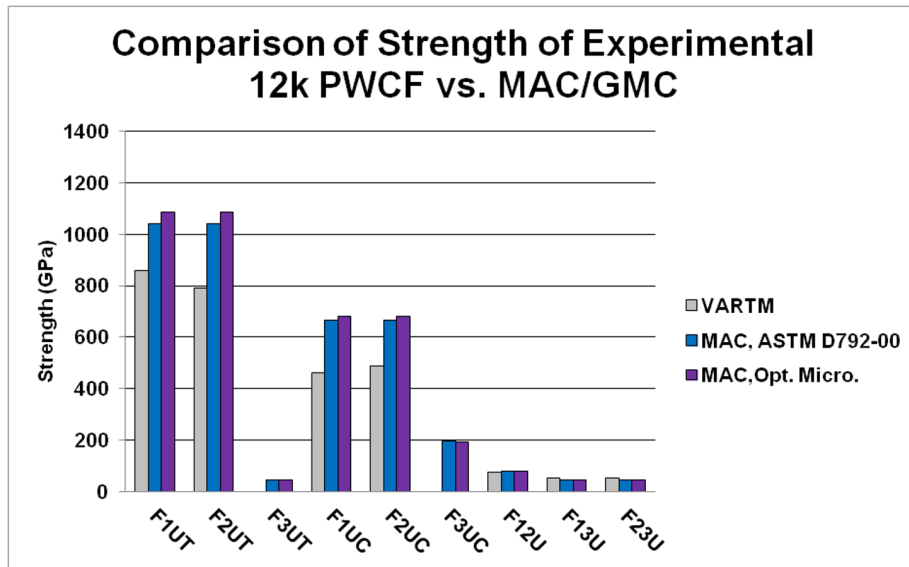
(b)

Figure 4.7: Comparison of experimental strengths from VARTM vs. MAC/GMC (a) 3k and (b) 12k material.
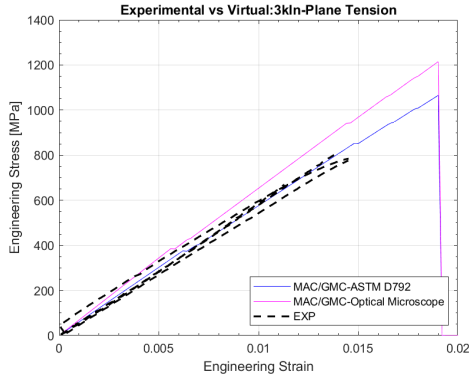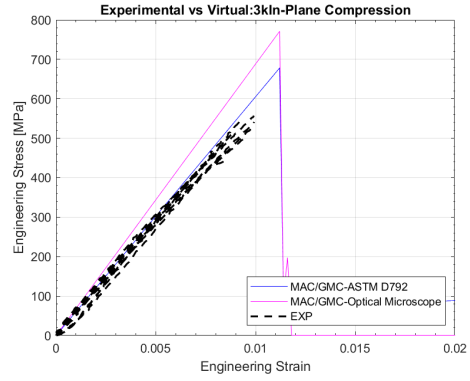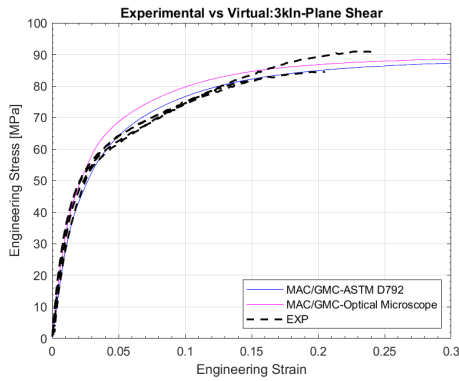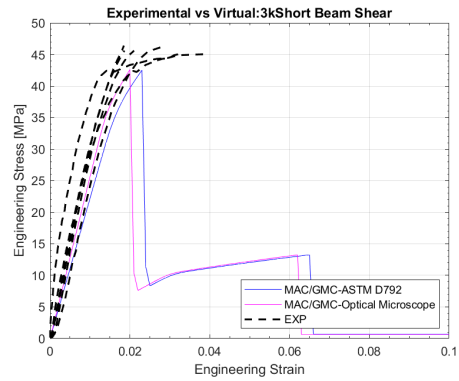
Figure 4.8: Sensitivity of tow volume fraction parameter compared with 3k tow experimental results at quasi-static loading (a) tension (b) compression (c) in-plane shear and (d) short beam shear
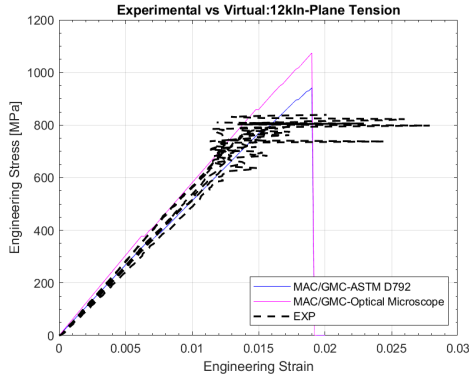
(a)
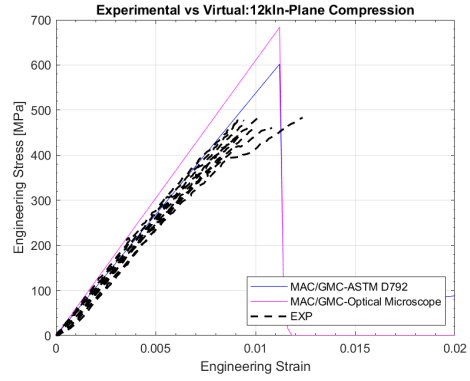
(b)
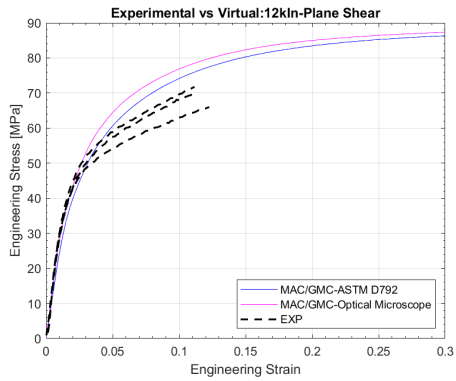
(c)
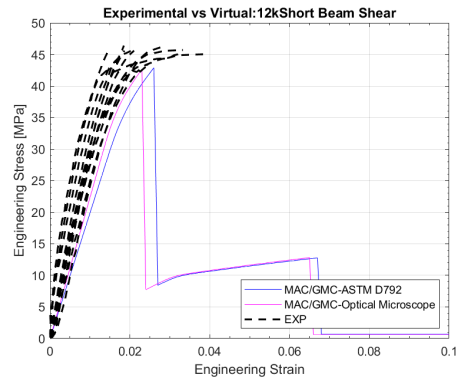
(d)

Figure 4.9: Sensitivity of tow volume fraction parameter compared with 12k tow experimental results at quasi-static loading (a) tension (b) compression (c) in-plane shear and (d) short beam shear
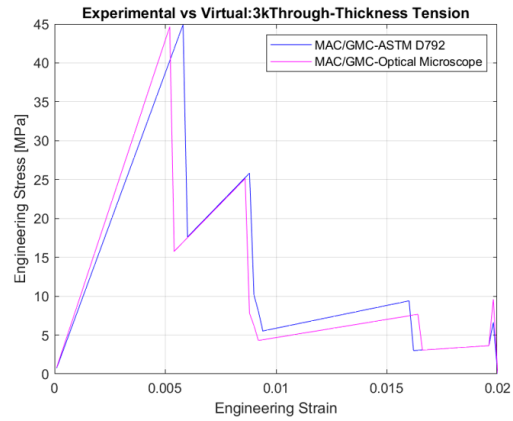
(a)
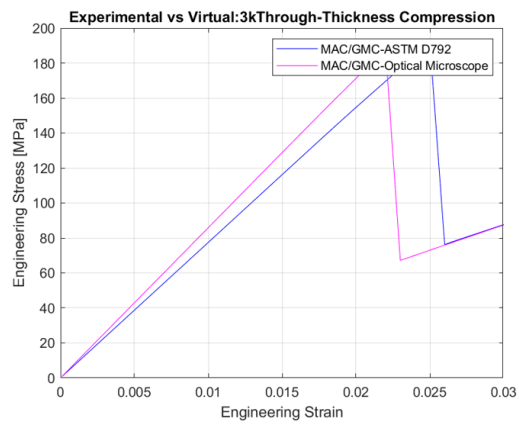
(b)

Figure 4.10: Sensitivity of tow volume fraction parameter from MAC/GMC results of 3-direction (a) tension and (b) compression for the 3k material

91

4.3 MAT213 Inputs

Inputs parameters for MAT213 are summarized in Table 4.8 and input curves are shown in Figures 4.11 and 4.12 for the 3k and 12k material, respectively. The elastic properties were determined from experimental tests from Table A.1 and A.2. The through thickness modulus and strength were obtained from MAC/GMC analysis and not experimentally. Additionally, MAT213 requires Poisson's ratio in ν_{31} and ν_{32} which were not directly determined experimentally. Therefore, the through thickness modulus obtained from MAC/GMC analysis were used to compute ν_{31} and ν_{32} from experimental ν_{13}, and ν_{23} values using the relationship from the orthotropic compliance matrix as shown in Equations 4.9 from [23]. Additionally, a table of yield strains is used for plasticity algorithm initiation. For normal loading in the direction of the fiber such as tension and compression where the macro-scale response is linear and brittle the yield value corresponds to the ultimate strain from the experiment. Figures 4.11 and 4.12 show the input curves with perfectly plastic input curves in black and damage curves in magenta for 3k and 12k materials, respectively. The portion of the curves up till peak stress are the same for perfectly plastic and damage curves which come from experimental curve averages from QS coupon experiments from Section 3.1. The difference in the perfectly plastic and damage curves is the post-peak response which is augmented. The damage portion of the curve uses a 90% stress reduction value. No damage is added to the off-axis curves. For the material behavior is modeled with a linear elastic response in the normal directions where the strength in the 1 and 2-direction for tension and compression come from experimental values. The strength for 3-direction tension and compression strength come from virtual stress predictions from MAC/GMC. To avoid numerical instabilities, the end strain of the input curve for all loadings is set to a large value.

Figure 4.11: MAT213 Input Curves for 3k material
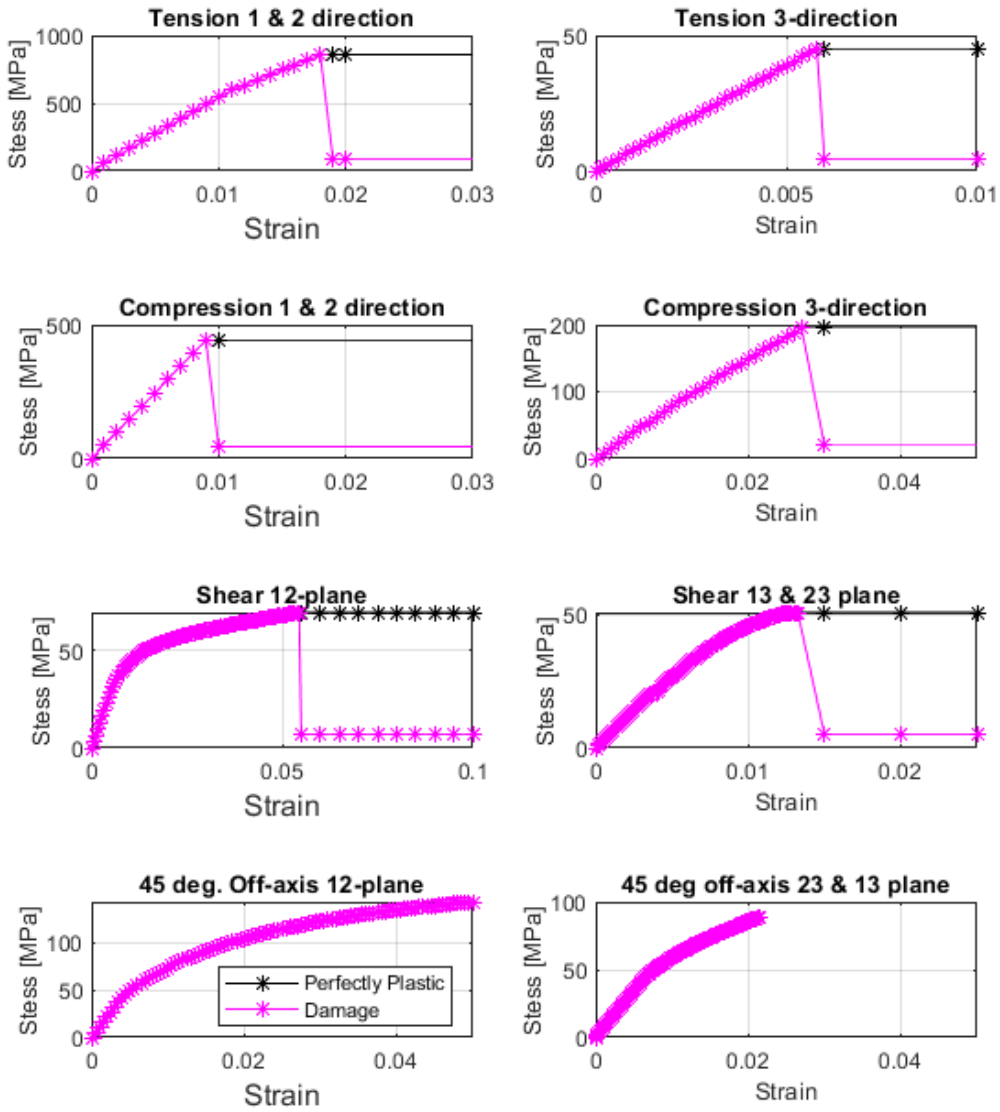
Figure 4.12: MAT213 Input Curves for 12k material

Table 4.7: Woven Composites Tabular Input Summary of MAT213.

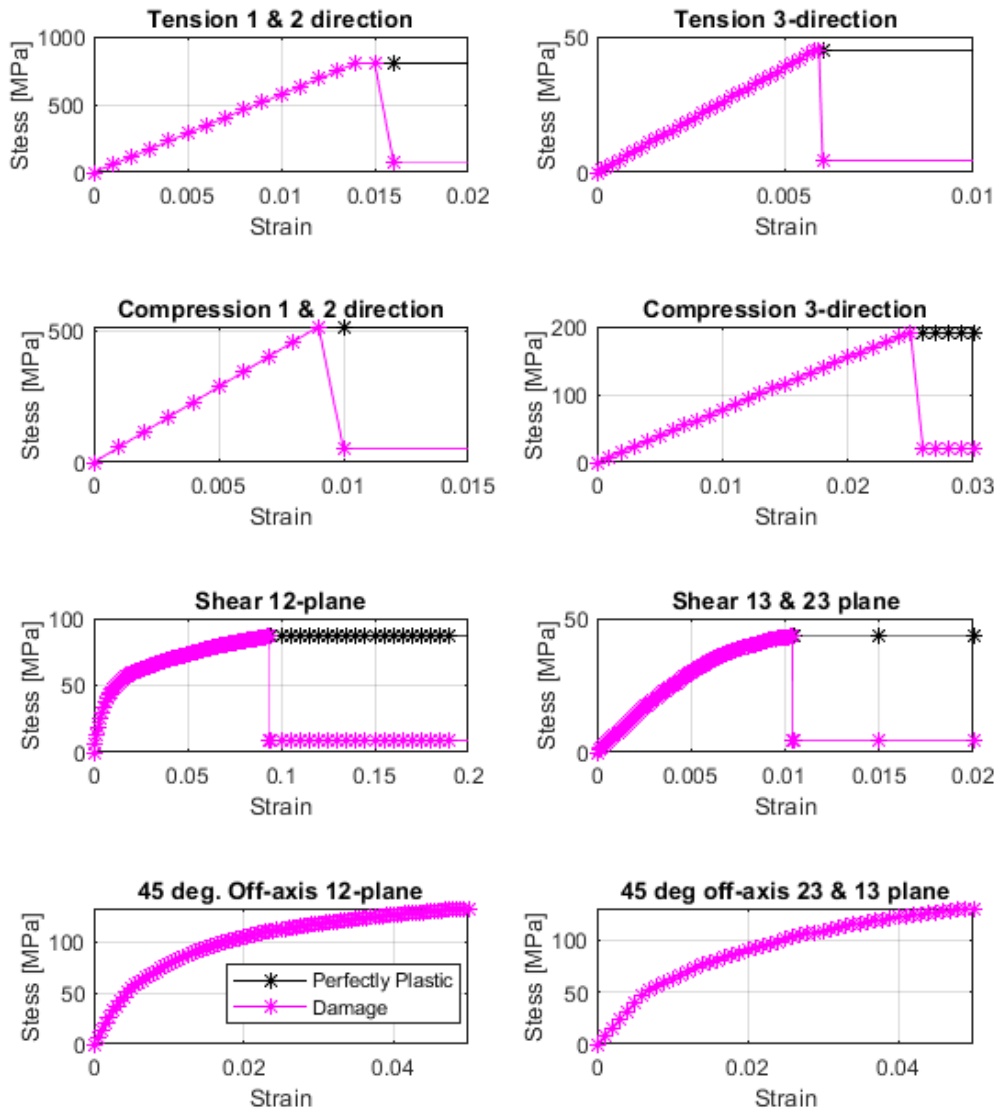| Label	Description	Experimental Virtual	ASTM Standard	Input
T1	Tension 1-Direction	Experimental	D3039	$\sigma_{11} vs. \epsilon_{11}, \nu_{12}, (\sigma_{11,Y})^T, (\epsilon_{11,Y})^T$
T2	Tension 2-Direction	Experimental	D3039	$\sigma_{22} vs. \epsilon_{22}, \nu_{21}, (\sigma_{22,Y})^T, (\epsilon_{11,Y})^T$
T3	Tension 3-Direction	Virtual		$\sigma_{33} vs. \epsilon_{33}, (\sigma_{33,Y})^T, (\epsilon_{33,Y})^C$
C1	Compression 1-Direction	Experimental	D695M	$\sigma_{11C} vs. \epsilon_{11C}, \nu_{13}, (\sigma_{11,Y})^C, (\epsilon_{11,Y})^C$
C2	Compression 2-Direction	Experimental	D695M	$\sigma_{22C} vs. \epsilon_{22C}, \nu_{23}, (\sigma_{22,Y})^C, (\epsilon_{2,Y})^C$
C3	Compression 3-Direction	Virtual		$\sigma_{33C} vs. \epsilon_{33C}, (\sigma_{33,Y})^C, (\epsilon_{33,Y})^C$
S12	Shear 1-2 Plane	Experimental	D7078M	$\tau_{12} vs. \gamma_{12}, (\sigma_{12,Y}), (\epsilon_{12,Y})$
S23	Shear 2-3 Plane	Experimental	D2344	$\tau_{23} vs. \gamma_{23}, (\sigma_{23,Y}), (\epsilon_{23,Y})$
S13	Shear 1-3 Plane	Experimental	D2344	$\tau_{13} vs. \gamma_{13}, (\sigma_{13,Y}), (\epsilon_{13,Y})$
O12	45 deg Off-axis in 1-2 Plane	Virtual		$\sigma_{45}^{1-2} vs. \epsilon_{45}^{1-2}, (\sigma_Y)^{1-2}, (\epsilon_Y)^{1-2}$
O23	45 deg Off-axis in 2-3 Plane	Virtual		$\sigma_{45}^{2-3} vs. \epsilon_{45}^{23}, (\sigma_Y)^{2-3}, (\epsilon_Y)^{2-3}$
O13	45 deg Off-axis in 1-3 Plane	Virtual		$\sigma_{45}^{1-3} vs. \epsilon_{45}^{1-3}, (\sigma_Y)^{1-3}, (\epsilon_Y)^{1-3}$

$$\nu_{31} = \frac{E_3}{E_1}\nu_{13} \tag{4.8}$$

$$\nu_{32} = \frac{E_3}{E_2}\nu_{23} \tag{4.9}$$

Characterization of flow coefficients is performed following a procedure similar to C.T. Sun for an associative flow law and similar approaches for unidirectional composites to determine flow coefficients. For a unidirectional composite determination of flow coefficients has been found in assuming transverse isotropy in the 2-3 plane with optimization software to find flow coefficients [2, 3, 76]. Similarly, for a balanced plain weave transverse isotropy in the 1-2 plane can be assumed when the warp and fill tow are the same reinforcing fiber which is the case for a balanced plain weave carbon fabric. Applying this assumption to Equation 4.10 reduces the number of

unknown flow coefficients from 9 to 6 as shown in Equation 4.11

$$h^2 = H_{11}\sigma^2_{11} + H_{22}\sigma^2_{22} + H_{33}\sigma^2_{33} + 2H_{12}\sigma_{11}\sigma_{22} + 2H_{23}\sigma_{22}\sigma_{33}$$
$$+ 2H_{13}\sigma_{33}\sigma_{11} + H_{44}\sigma^2_{12} + H_{55}\sigma^2_{23} + H_{66}\sigma^2_{13} \tag{4.10}$$

$$h^2 = H_{11}(\sigma^2_{11} + \sigma^2_{22}) + H_{33}\sigma^2_{33} + 2H_{12}\sigma_{11}\sigma_{22}$$
$$+ 2H_{23}(\sigma_{22}\sigma_{33} + \sigma_{33}\sigma_{11}) + H_{44}\sigma^2_{12} + H_{55}(\sigma^2_{23} + \sigma^2_{13}) \tag{4.11}$$

Where $H_{11} = H_{22}$, $H_{13} = H_{23}$ and $H_{55} = H_{66}$. It has been observed from experiments and literature [88, 89] that plain weave materials exhibits small nonlinearity. Therefore, by setting $H_{11} = 1$ generality of the transversely isotropic flow law can be applied. Flow coefficients H_{12}, H_{13}, H_{23} are calculated using the relationship from Equation 2.27 and assuming that the plastic Poisson ratio's are approximately equal to the elastic Poisson's ratio, $\nu^e \approx \nu_p$

$$H_{12} = -H_{11}\nu^p_{21} \approx -H_{11}\nu^e_{21}$$
$$H_{13} = -H_{11}\nu^p_{13} \approx -H_{11}\nu^e_{13}$$
$$H_{23} = -H_{11}\nu^p_{23} \approx -H_{11}\nu^e_{23} \tag{4.12}$$
$$H_{33} = \frac{\nu^p_{13}}{\nu^p_{31}} \approx \frac{\nu^e_{13}}{\nu^e_{31}}$$

Lastly the shear flow coefficients, H_{44} and H_{55}, are calibrated to match the through thickness tension curves in effective stress vs effective plastic strain space. Where a uniaxial load in the through thickness direction using MAC/GMC micromechanics which is extrapolate to 5 % strain and does not included subcell failure. Then assuming that the effective stress is equal to the flow surface and the effective plastic strain is found using Equations 4.10. Similarly, a unidirectional shear load for both 12-plane and 23-plane can be applied which can be then be converted to effective stress and effective plastic strain as shown in Equation 4.14. Figure 4.13 shows parametrically the effects of H_{44} and H_{55}. It is seen that flow coefficient of 45 results in

the closest match between the target through thickness curve and the shear curves. For the case where the fibers are modeled as elastic then no plastic strain is allowed in the elastic directions, which can be done by setting $H_{11} = H_{22} = 0$ which would also result in $H_{12} = H_{13} = H_{23} = 0$.

$$h = \sigma_e = \sigma_{12}\sqrt{H_{44}} \tag{4.13}$$

$$\epsilon_e^p = \frac{\epsilon_{12}^p}{0.5\sqrt{H_{44}}} \tag{4.14}$$
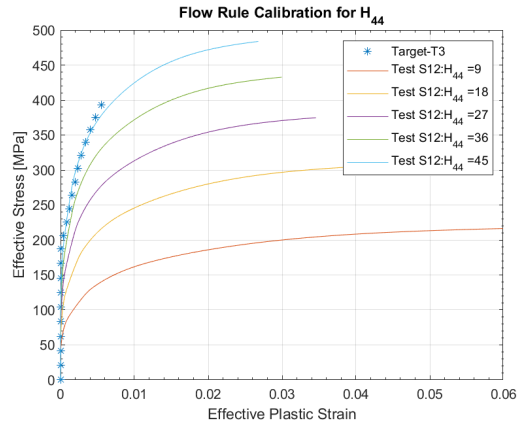
(a)
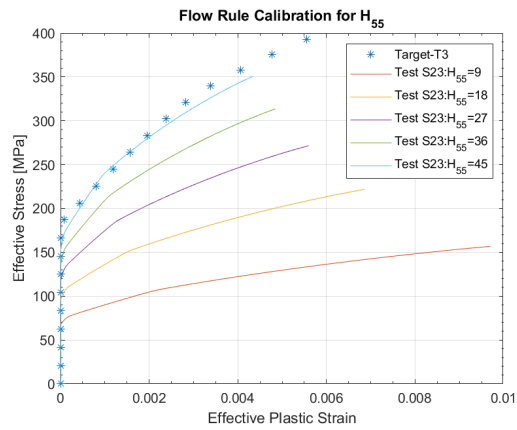
(b)

Figure 4.13: Flow coefficient characterization for 3k material for (a) in-plane shear and (b) transverse shear

Table 4.8: MAT213 Input Parameters

Parameter	Description	PWCF 3k input	PWCF 12k input
RO	Mass density, $\frac{g}{cm^3}$	1.448	1.428
EA	Young's modulus in a-direction, GPa	57.44	54.11
EB	Young's modulus in b-direction,GPa	57.44	54.11
EC	Young's modulus in c-direction,GPa	7.73	7.65
PRBA	Elastic Poisson's ratio ba	0.044	-0.074
PRCA	Elastic Poisson's ratio ca	0.068	0.071
PRCB	Elastic Poisson's ratio cb	0.071	0.071
GAB	Shear modulus in a-b plane, GPa	3.35	3.18
GBC	Shear modulus in b-c plane, GPa	2.86	2.86
GCA	shear modulus in c-a plane, GPa	2.86	2.86
PTOL	Yield function tolerance	10^{-6}	10^{-6}
H11	Flow coefficient	1	1
H22	Flow coefficient	1	1
H33	Flow coefficient	6.08	6.94
H12	Flow coefficient	-0.044	0.074
H23	Flow coefficient	-0.504	-0.500
H13	Flow coefficient	-0.528	-0.505
H44	Flow coefficient	45	45
H55	Flow coefficient	45	45
H66	Flow coefficient	45	45

4.4 Verification

For the single element and multi-element coupon verification, reduce integration solid hex elements with a calibrated stiffness based hourglass control based on Belytschko-Bindeman [90] is used for all the models for computational efficiency. This form of hourglass control is recommended for low velocity impact and for elements with large aspect ratios [91] which typically occurs when meshing composite parts. The layup of the coupons tested had all 0 degree plies, therefore, the coupons are modeled as smeared homogeneous and delamination between plies was not included. Simulations were run on a Windows desktop computer using LS-DYNA double presion explicit solver. Models with the finest mesh were ran on a Linux cluster.

When modeling composite materials the material coordinate system needs to be defined. This is important when dealing with orthotropic materials that are directionally dependent. For othotropic materials, LS-DYNA offers various options for defining material axis [25]. Where AOPT=0 defines the locally orthotropic material axis using the local element axis. This option however does not allow for rotations about the normal axis which is needed for composites with different ply orientations. AOPT=2 defines the globally orthotrpoic material axis using two vectors a and d. This option is well suited for composite parts that are flat. Lastly, AOPT=3 allows for locally orthotropic material axis and allows for rotation of material axis which is well suited for curved composite structures, such as c-channel parts with varying ply orientations. For single element and coupon verification AOPT=2 is used, whereas, for the validation case study of a wingbox structure, AOPT=3 is needed to properly capture the different ply orientations in the c-channel parts.

Additionally, from literature [92, 93, 94, 95] invariant node numbering (INN) is recommended for directionally dependent materials that undergo large deformations due to fiber realignment. INN prevents erroneous definition of the local coordinate
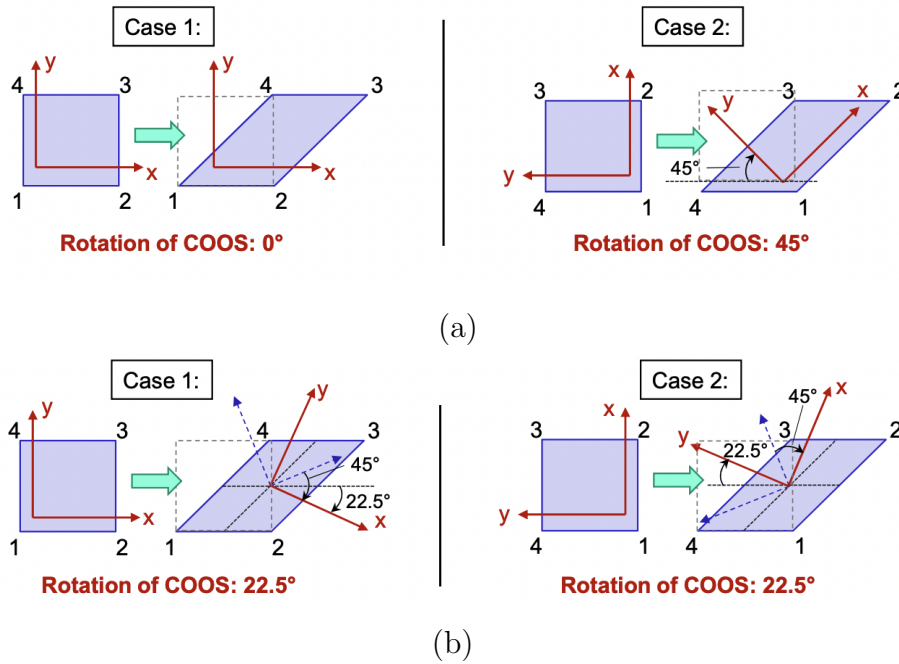
Figure 4.14: Change in element coordinate system (ECS) during deformation with (a) no invariant node numbering and (b) with invariant node numbering. (c) Representation of vectors to define ECS with INN. [25]

system when elements are highly distorted [94], as shown in Figure 4.14a. Additionally, INN makes element forces independent of node sequencing. INN uses a bisection method to define local element axis, as illustrated in Figure 4.14b. For shells INN creates two vectors, a_1 and a_2, using midpoints from the element sides. Next, a vector, n, normal to a_1 and a_2 is created. Additionally, a vector, b_1, is created which is in the middle of a_1 and a_2, as shown in Figure 4.15. Vector, b_2, is created which is orthogonal to n and b_1. Lastly, vectors b_1 and b_2 are rotated back 45 deg to obtain the local element local coordinate system. A similar process is performed for solid elements.

Figure 4.15: Representation of vectors to define ECS with INN. [25]

4.4.1 Single Element

Single element verification is performed to verify that the material inputs have been correctly implemented. Loading is applied at a cons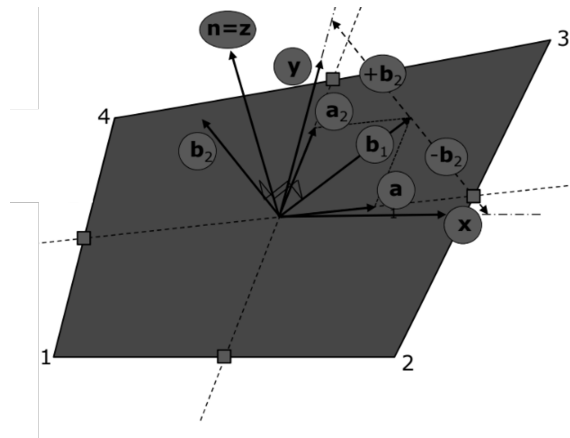tant displacement rate and boundary conditions for tension and compression along all the principle material directions (PMD) are shown in Figures 4.16a and 4.16b, respectively. Similarly, simple shear in all three principle material planes (PMP) are shown in Figure 4.16c. In addition to simple shear, pure shear loading of single elements is done where the material coordinate system is rotated 45 degrees in the PMP and a bi-axial tension-compression loading is applied as shown in Figure 4.17. Outputs of the single element for tension, compression and simple shear are output in the global reference frame, whereas, for pure shear the results are output in the local material frame.

The 3k tension curves shown in Figure 4.11 were simulated using MAT 213 and the results compare well with the experimental stress-strain input curves. In Figure 4.18, the black indicates the experimental input curves, and the red curve show the output from the LS-DYNA simulation. It was found that in tension for all normal loading, the single element output matched the perfectly plastic input. When using the the damage curves, the response till peak stress matches the input. Past peak
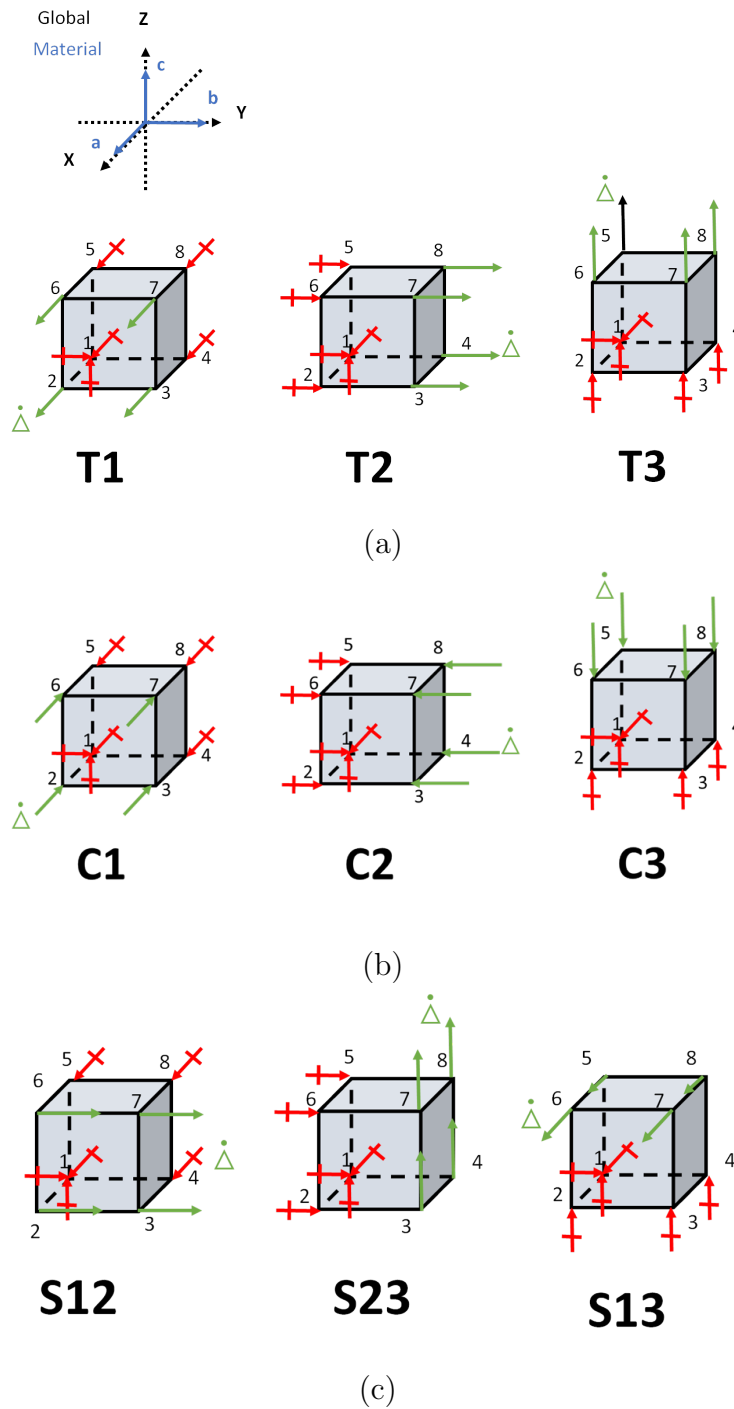
102

Figure 4.16: Single elements boundary conditions and loading in (a) tension and (b) compression and (3) simple shear
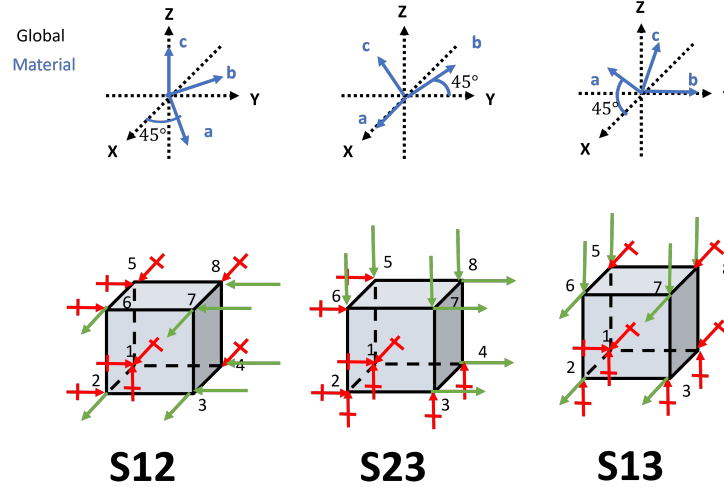
103

Figure 4.17: Single elements loaded in tension and compression in all three normal directions with the boundary conditions

stress the simulation shows differences with the input curves. This is due to sharp drop off past peak stress which is numerical difficult to capture. As strain evolves the residual stress is seen to match the input for 3k and 12k damage curve inputs. For the 12k input the elastic response matches the input and the plastic response follows the correct trend from the input but does not match the exact slope, as seen in Figure 4.18 and 4.19.

For in-plane compression the response of the perfectly plastic input is seen to produce numerical oscillations occurring past peak stress. This was seen in both the 3k and 12k materials, Figures 4.20 and 4.21. The results of the compression single elements with damage inputs is seen to produce similar trends to the tension single elements where the slope of the stress reduction does not exactly match the input.

Similar to the tension and compression single element simulations, the in-plane simple shear elements were found to match up with the perfectly plastic input curves

when INN is not invoked for both 3k and 12k input. When INN is invoked in simple shear the response in the elastic and small strain region appears to be correct, but when the strain begins become large the response begins to divert from the experimental input. Additionally, it is seen in the in-plane simple shear with INN invoked that the response using perfectly plastic or damage input curves produce the same output for the 3k material as shown in Figures 4.22a and 4.22b. At large strains the deformed element the element axis have changed with INN which explains why the response deviates from the input. For transverse shear with perfectly plastic curves, the elastic portion is captured and the initial nonlinearity follows the input curve but does not match the response as seen in Figures 4.22c and 4.22c. The behavior of the transverse shear loaded in simple shear with perfectly plastic curves is seen to behave the same with and without INN invoke as seen in Figure 4.22c. The plateau stress is correctly capture for simple shear loading for 3k and 12k when using the perfectly plastic curves. When using the damage curves the residual stress of the transversely loaded simple shear element varies when INN is invoked. When INN is not invoked the residual stress matches the input but when INN is invoke the residual stress is overestimated both both 3k and 12k input as seen in Figures 4.22d and 4.23d, respectively.

From pure shear single element simulations it is seen that the response behave similarly with and without INN invoke. This is the case for all three shear single elements and for both material inputs. For in-plane shear the response matches the input under small strains and begins to deviate under large strains, similar to the simple shear case with INN invoked. The pure shear response shows a gradual stress reduction which is contrary to the simple shear with INN invoked which shows stress increasing as strains increase. For transverse shear loaded in pure shear the nonlinear response matches the initial nonlinearity, however, peak stress is seen to drop early and more gradually compared to the input curves.
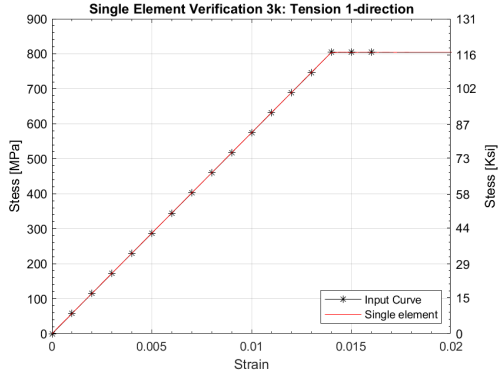
(a) 3k, T1-perfectly plastic
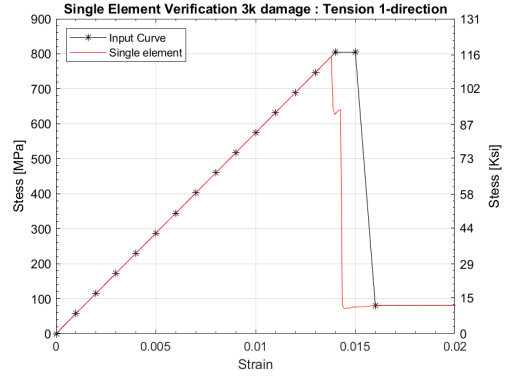
(b) 3k, T1-damage
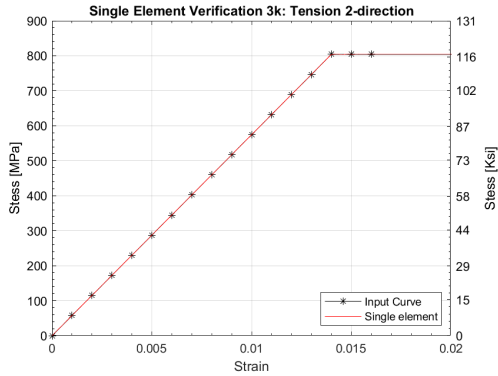
(c) 3k, T2-perfectly plastic

(d) 3k, T2-damage

(e) 3k, T3-perfectly plastic

(f) 3k, T3-damage

Figure 4.18: Single element verification of tension loading for 3k material with input curve shown in black and simulation shown in red.

(a) 12k, T1-perfectly plastic

(b) 12k, T1-damage

(c) 12k, T2-perfectly plastic

(d) 12k, T2-damage

(e) 12k, T3-perfectly plastic

(f) 12k, T3-damage

Figure 4.19: Single element verification of tension loading for 12k material with input curve shown in black and simulation shown in red.
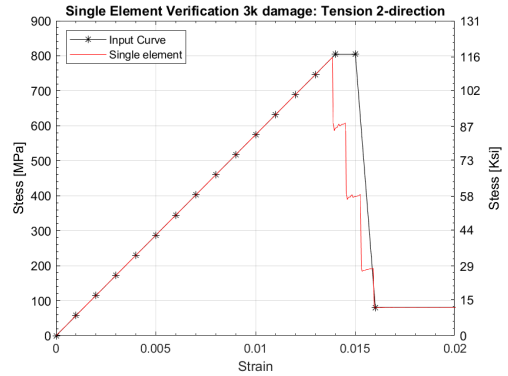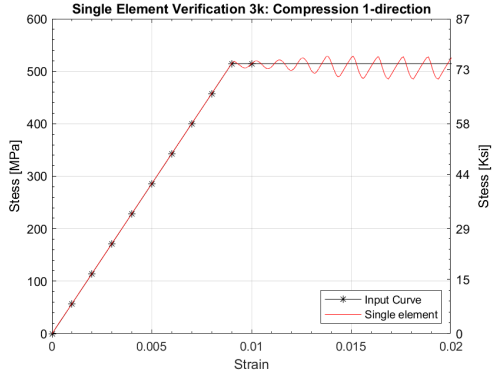
(a) 3k, C1-perfectly plastic

(b) 3k, C1-damage

(c) 3k, C2-perfectly plastic

(d) 3k, C2-damage

(e) 3k, C3-perfectly plastic
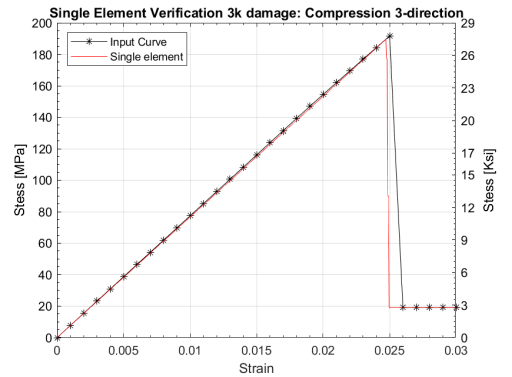
(f) 3k, C3-damage

Figure 4.20: Single element verification of compression loading for 3k material with input curve shown in black and simulation shown in red.
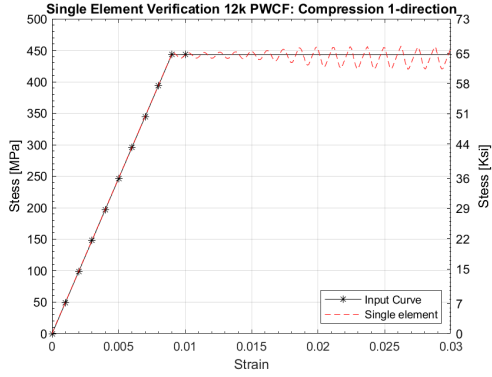
(a) 12k, C1-perfectly plastic
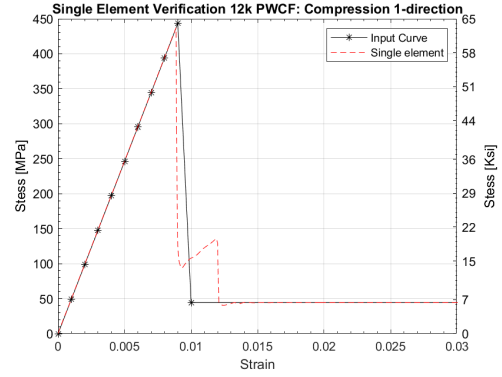
(b) 12k, C1-damage
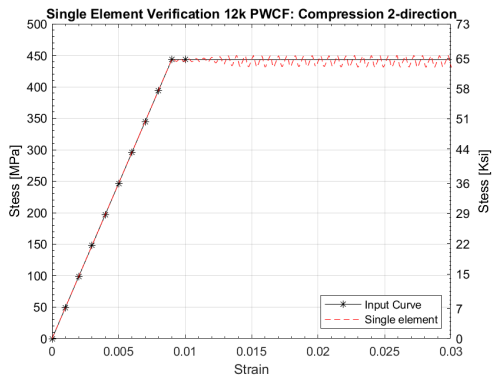
(c) 12k, C2-perfectly plastic
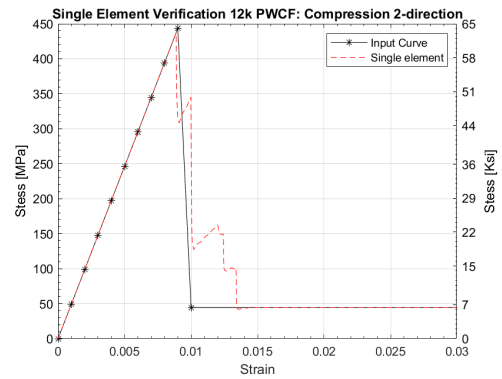
(d) 12k, C2-damage
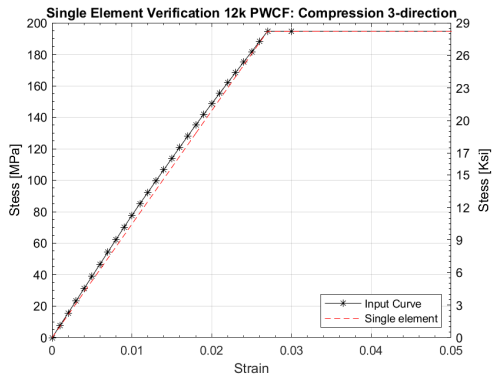
(e) 12k, C3-perfectly plastic
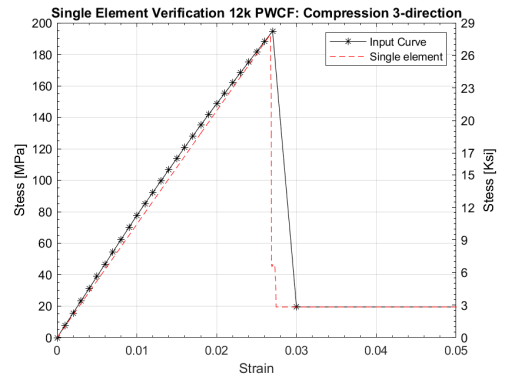
(f) 12k, C3-damage

Figure 4.21: SSingle element verification of compression loading for 12k material with input curve shown in black and simulation shown in red.
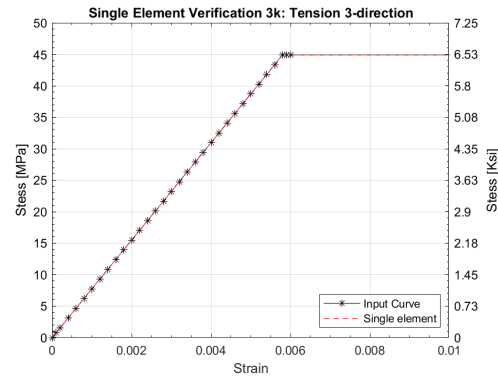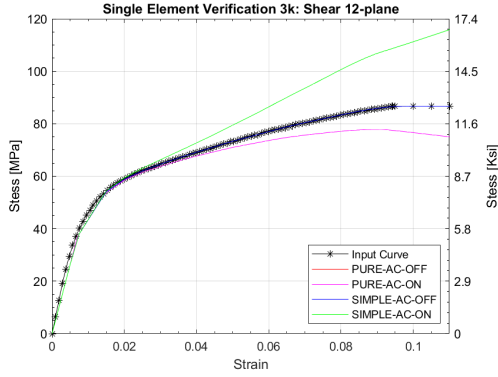
(a) 3k, S12-perfectly plastic
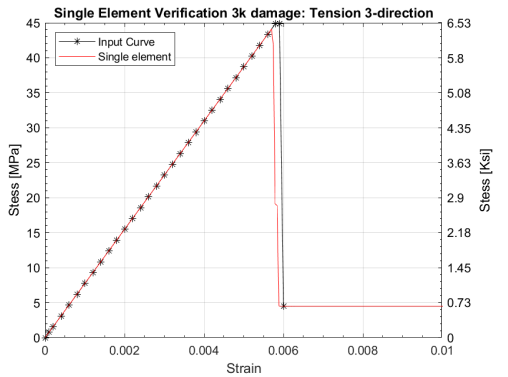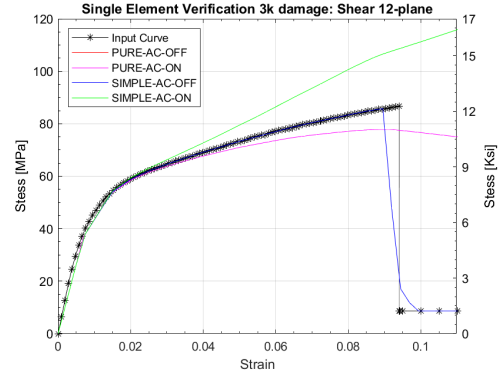
(b) 3k, S12-damage
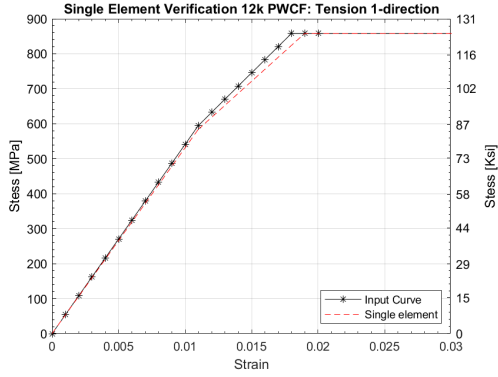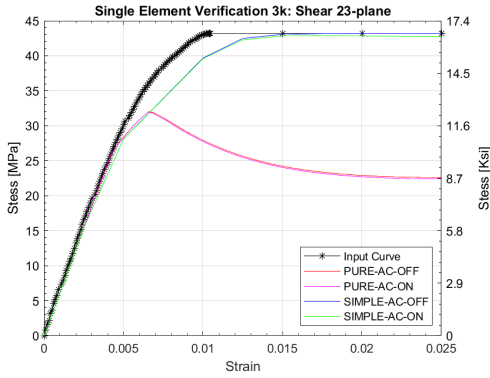
(c) 3k, S23-perfectly plastic
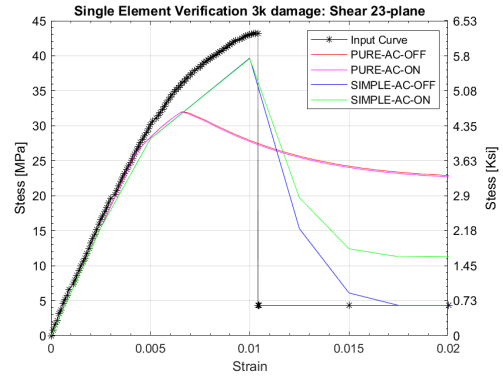
(d) 3k, S23-damage
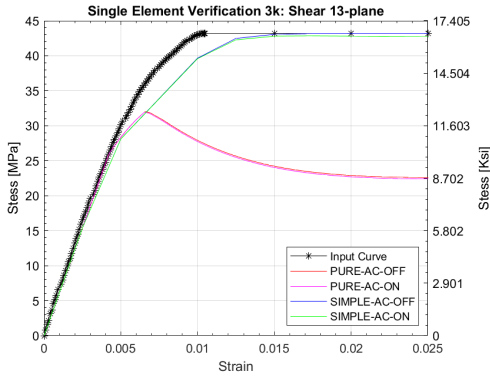
(e) 3k, S13-perfectly plastic
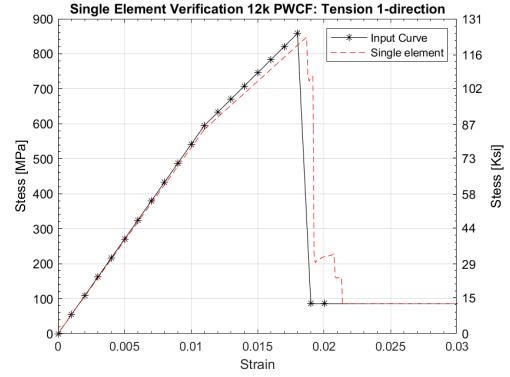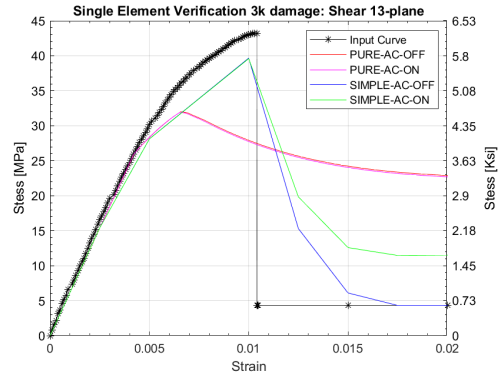
(f) 3k, S13-damage
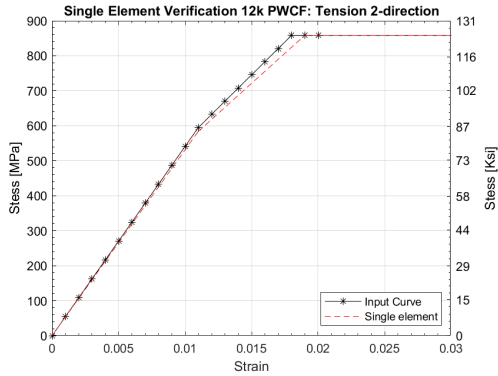
Figure 4.22: Single element verification of shear loading for 3k materialwith input curve shown in black and simulation shown in red.
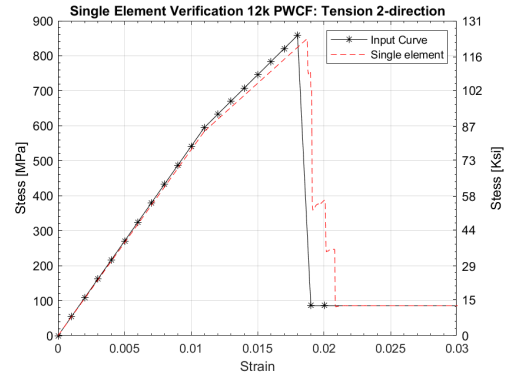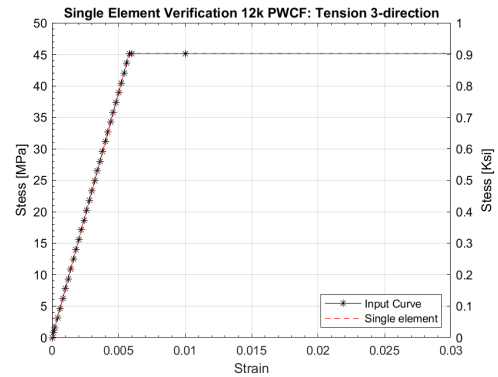
110
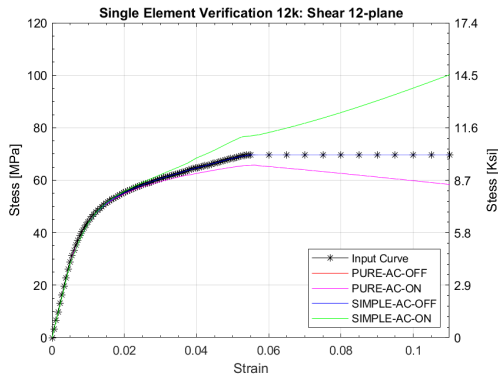
(a) 12k, S12-perfectly plastic
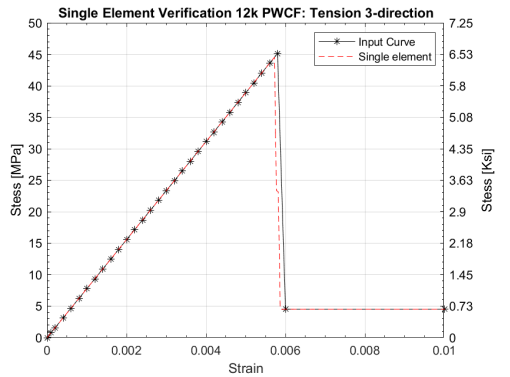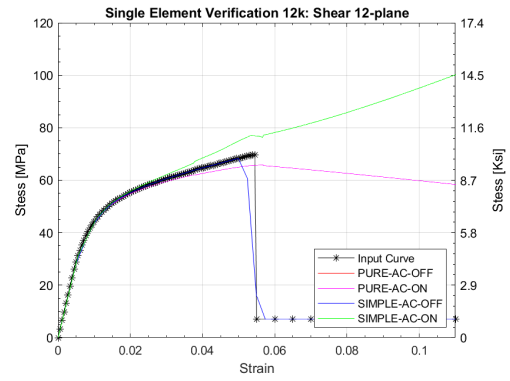
(b) 12k, S12-damage
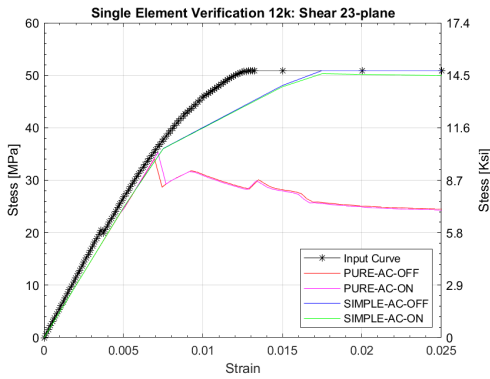
(c) 12k, S23-perfectly plastic
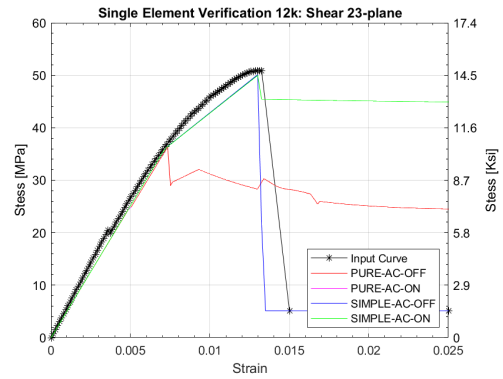
(d) 12k, S23-damage

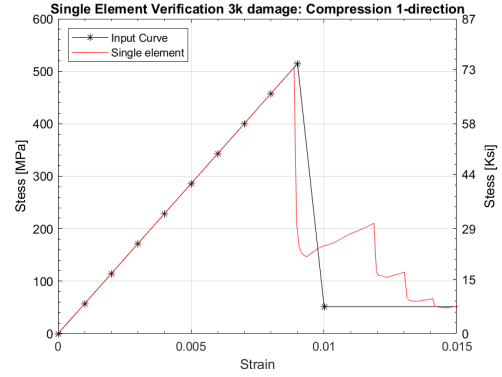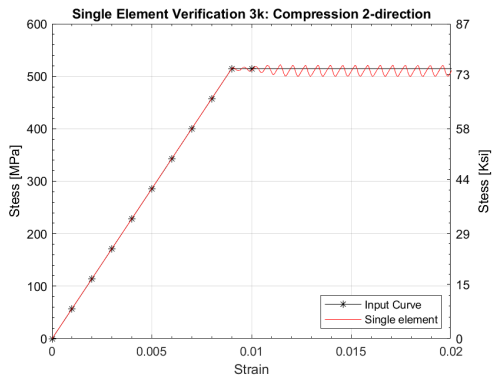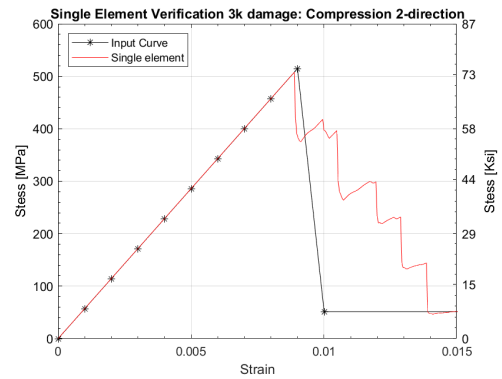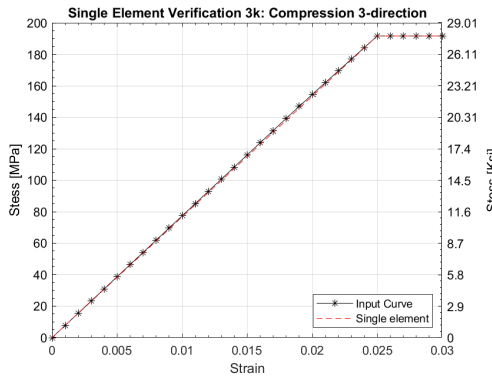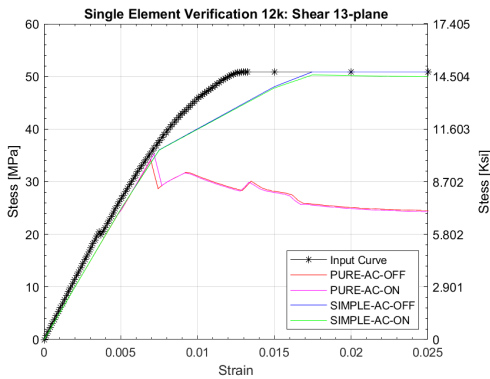(e) 12k, S13-perfectly plastic
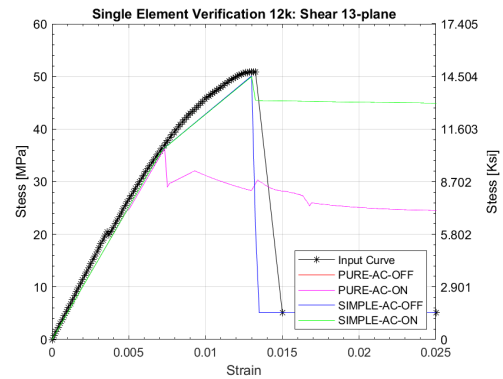
(f) 12k, S13-damage

Figure 4.23: Single element verification of shear loading for 12k material.

4.4.2 Coupon Level Verification

The goal of the multi-element verification studies was to simulate more closely the geometry of coupon experiments done in Section 3.1 to see to what extent the experimental test could be replicated. The same idea for verification is done as single element, but with more complicated geometry. The element aspect ratio and size was kept similar for all the coupon verification models as is summarized in Table 4.9. Symmetry is taken advantage of to reduce computational cost and is used for compression, v-notch shear and short beam shear models.

Table 4.9: Model Summary of Coupon Models Verification.

Model	Symmetry plane	Min. Aspect Ratio
Tension	None	12.7
Compression	XY	12.9
V-notched Rail Shear	XY	10.8
Short Beam Shear	YZ & XZ	12.9

V-notch rail shear coupon model was meshed with a biased that has a refined mesh near the notch tips. The bolted joint are modeled with tied contact between the specimen and fixture for simplicity and for computation efficiency. Displacements in the z-direction are constrained on the bottom face of the specimen to model XY plane symmetry. Additional z-direction constraints are imposed to capture the fixture boundary conditions at dowel pin and loading pins. Nodal forces at the reaction end are used to calculate engineering shear stress with the specimen cross-sectional area. An extraction area of 25 mm × 12 mm, as seen in Figure 4.24, is used to get an average strain value. V-notch rail shear specimen was simulated using three elements sizes as shown in Figure 4.25 which had a refinement factor of 1/8. A mesh convergence study is then performed which compared the error between peak shear stress in the simulation at damage initiation with the peak shear stress from the input curve which is shown in Figure 4.27. For the 12k material a smaller error

112

exist between the simulation and experiment when compared to the 3k material, as seen in Figure 4.27. Qualitatively, the contour of the shear damage variable (Figure 4.26) is seen to match the damage observed from experimental high speed camera images as shown in Figure 3.27. The stress-strain response from the simulation is compared with input curves as shown in Figure 4.28. It is seen that the max stress compares well with the input, however, the strain at which damage initiates in the model is smaller compared to the experiments. This lower strain can be the result of using an extraction area that is larger and not exactly the same as the experiments. The post-peak response is seen to improve with mesh refinement as seen in Figure 4.28. From mesh convergence study, Figure 4.27, it is seen that with mesh 3 the the peak stress at damage initiation results do not show much difference compared to mesh refinement 1. Therefore, for tension, compression and short beam shear simulations a coarse mesh and one refinement is performed using perfectly plastic input curves.

$u_x = u_y = u_z = 0$

Δ

Extraction area: 25 X 12 mm

Bottom View

$u_z = 0$

Isometric View

by LS-PRE

$\dot{\Delta}$
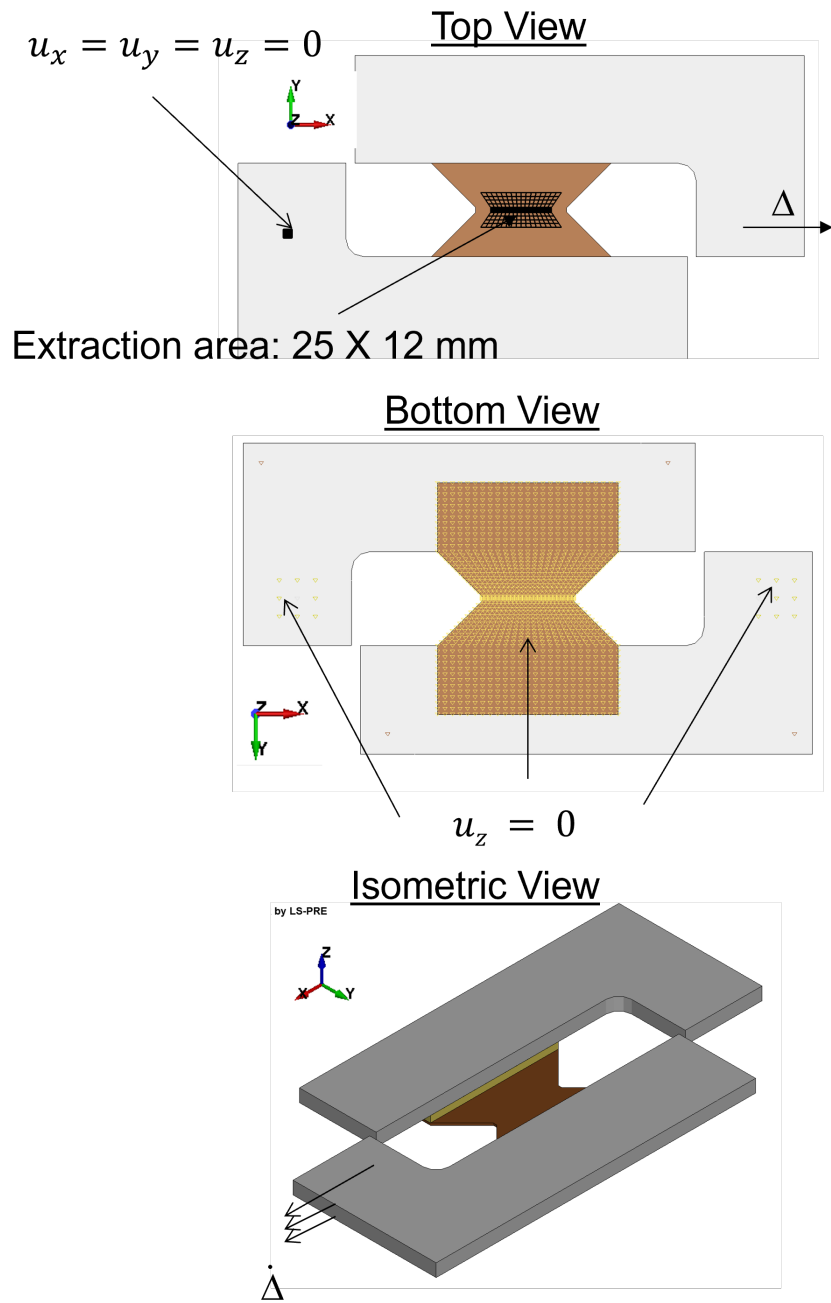
Figure 4.24: V-notch rail shear model setup.

(a) 156 elements   (b) 1248 elements   (c) 9984 elements
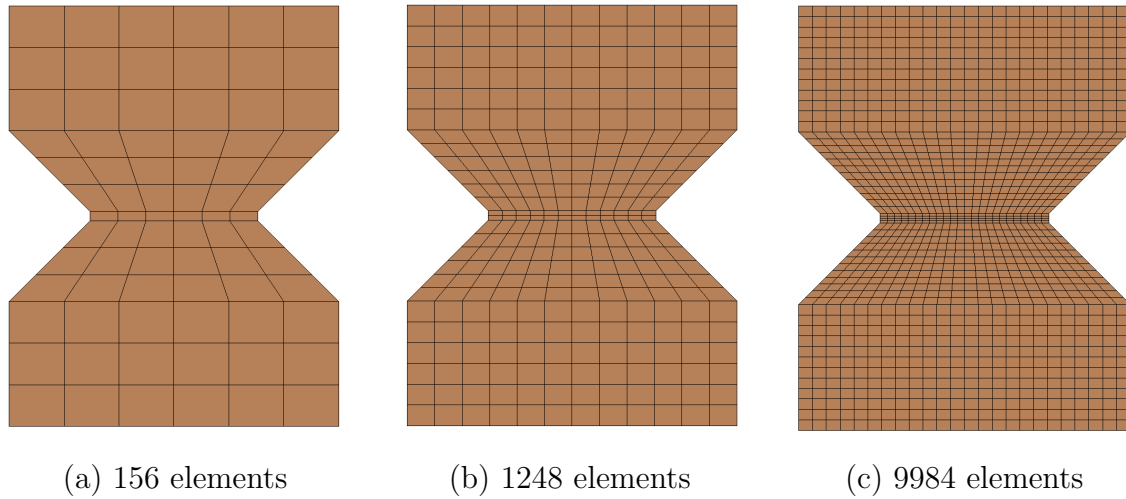
Figure 4.25: FEA mesh for v-notch shear verification with top view of (a) coarse (b) mesh refinement 1 (c) and mesh refinement 2.

The specimen geometry used for the verification of the in-plane tension specimen for both 3k and 12k material inputs is shown in Figure 4.29 where the specimen gage section is modeled with a 25.4 mm length, 2 mm thickness, and 25.4 mm width. Element size was kept uniform for tension and compression models. For the compression model, similar boundaries as the v-notch shear model are used which takes advantage of XY symmetry. Nodal forces at the reaction end is used to calculate engineering stress for tension and compression. Extraction area of size 13 mm × 1 mm and 25.4 mm × 25.4 mm is used to obtain an average strain value as shown in Figures 4.29 and 4.30 for compression and tension, respectively. The results of the multi-element simulations in tension with 3k material inputs match the elastic response. Softening is observed to occur past peak stress, as seen in Figure 4.32a. For the 12k material inputs, a similar trend which was observed in the single elements where the nonlinear harding does not match the input. The compression simulations do match the response of the input well. Short beam shear model uses a biased mesh.

(a)   (b)
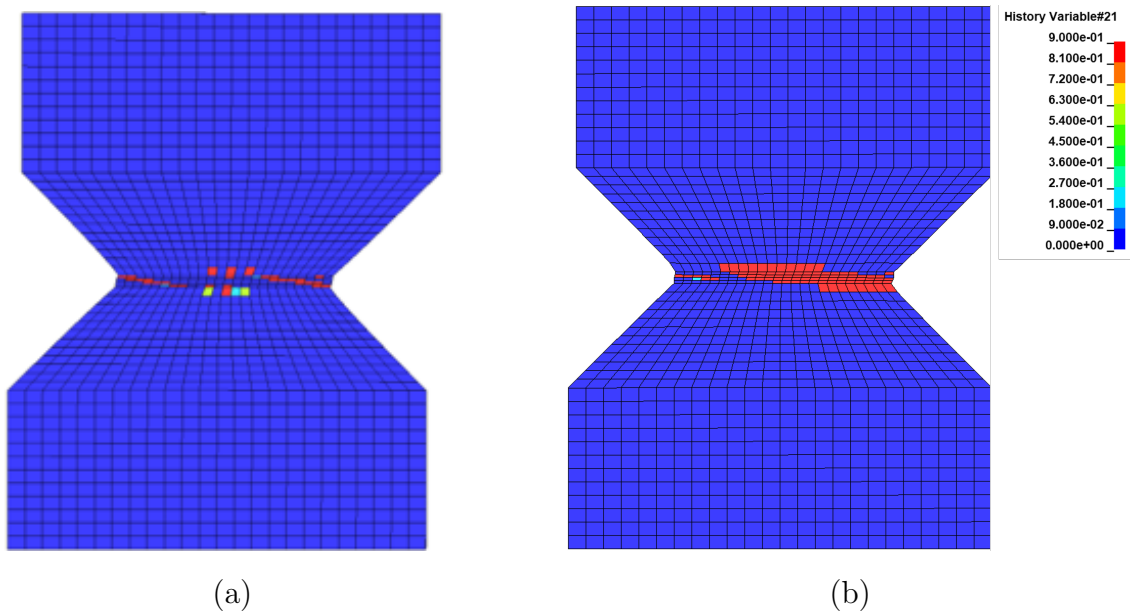
Figure 4.26: FEA results showing shear damage contours at the initiation of damage with finest mesh for and (12k) material inputs.
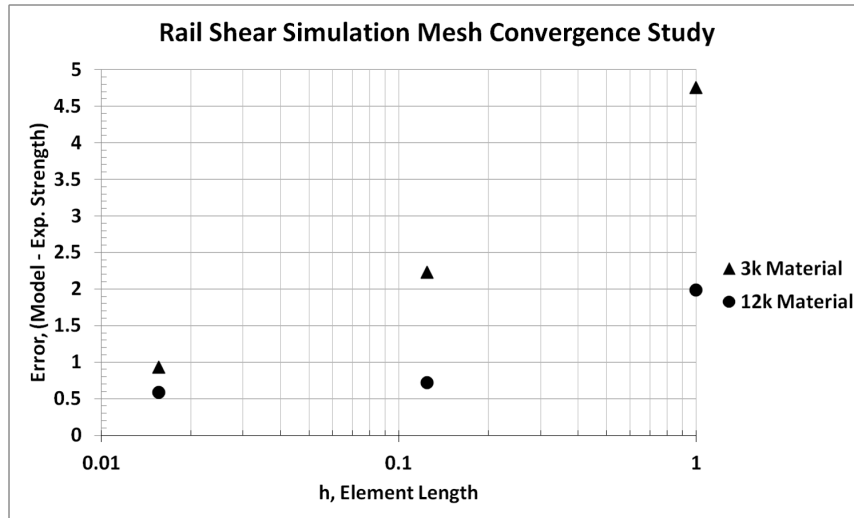
Figure 4.27: V-notch rail shear mesh convergence plot showing error between simulation at damage initiation and experimental strength.

(a)   (b)
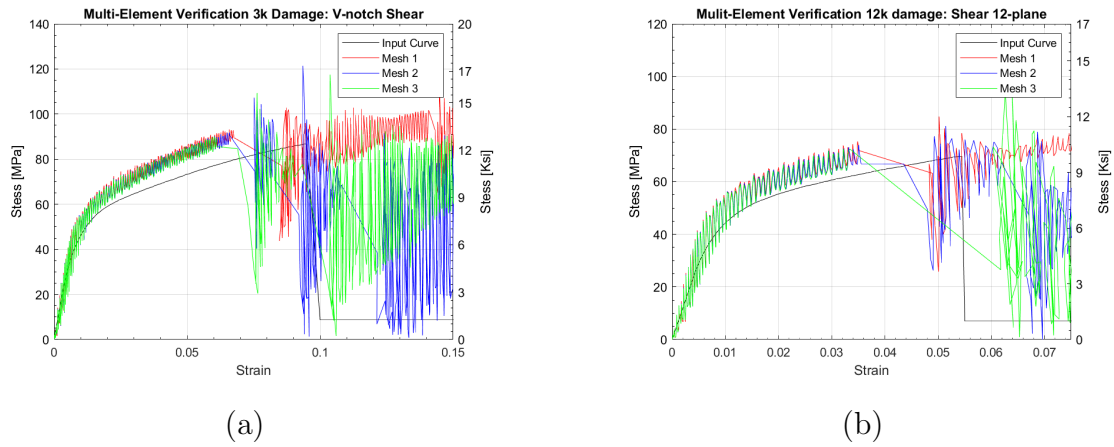
Figure 4.28: Stress strain response of v-notch coupon verification of (a) 3k and (b) 12k material.
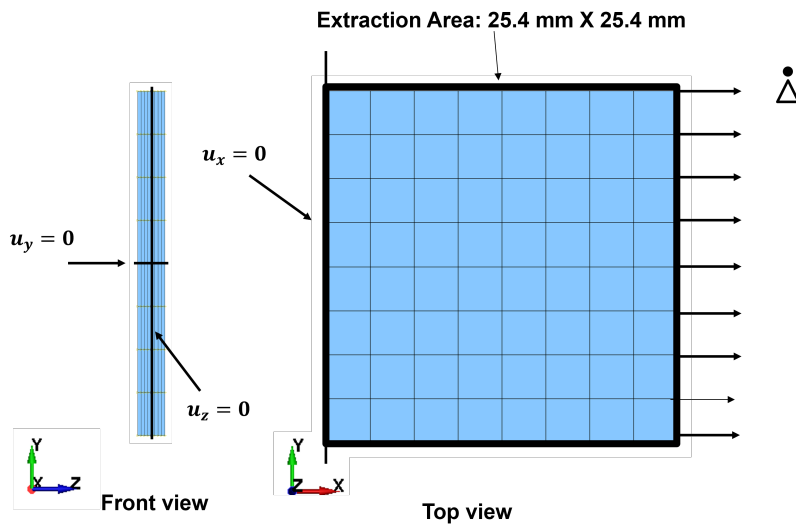
Figure 4.29: FEA mesh for tension verification with top view oand side view
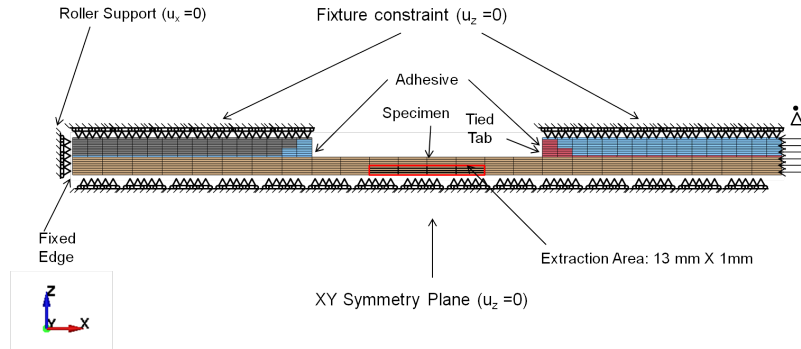
Figure 4.30: FEA mesh for compression model verification with top view of (a) coarse and (b) fine mesh. (c) the side view of fine mesh
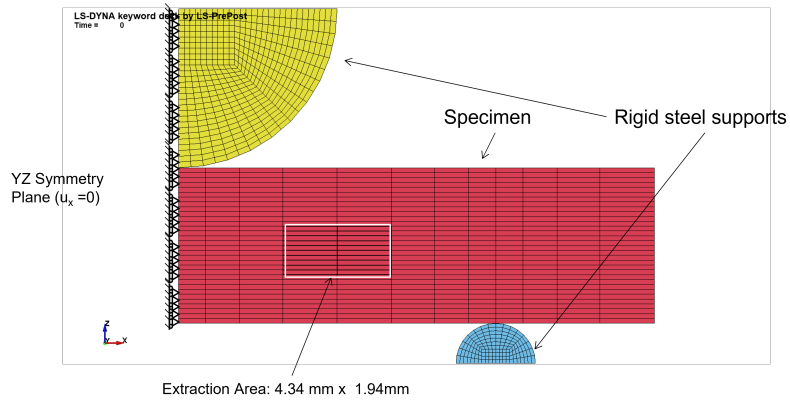
Figure 4.31: FEA mesh for short beam shear quarter model verification with top view of (a) coarse and (b) fine mesh. (c) the side view of fine mesh

4.5 Validation Studies

4.5.1 Experiment Setup

The pendulum impact system used in the following studies was been previously developed in Delaney and Whistler [96, 97] for flat plate composites. The system consists of stacked 50.8 mm diameter stainless steel masses mounted on the end of a stiff, lightweight fiberglass rod as shown in Figure 4.33. The swinging radius of the mass center is 1.42 m. Masses vary depending on the impacting tip radius. The mass of all the parts for the impactor tip, m_N, is summarized in Table 4.10. The impacting tip consists of a hemispherical tip mounted onto a dynamic force-measuring load cell. A US Digital A-2 absolute encoder wheel with 3600 discrete steps to measure the angle of arm of the pendulum system to 0.1 degree resolution. All data scquistion is capture with a 12-bit USB Picoscope 3424 4-channel oscilloscope. A picture frame fixture with a 10.5 in. × 10.5 in. window is used to attached wingbox specimen to pendulum impactor support structure.

Table 4.10: Pendulum impactor tip masses

Description	Mass (kg)
25.4 mm steel hemi-sphere tip	0.4622
Load cell 1060 V5 insert	0.4613
Load cell 1060 V5 adaptor	0.6265
End weight	0.6174
5 weights	1.8945
Wire	0.0107
Rod large	0.0757
Release	0.1031
Center section	0.7079
Bar mass, m_B	0.7217
Total tip mass, m_N	4.9593
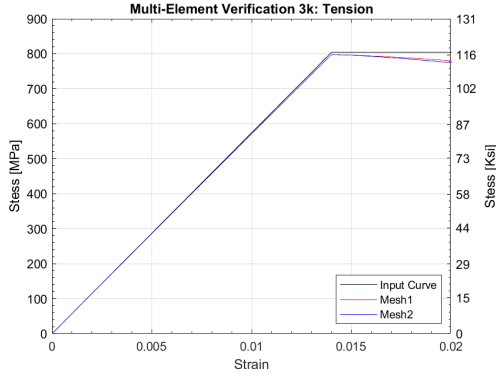
(a) 3k tension
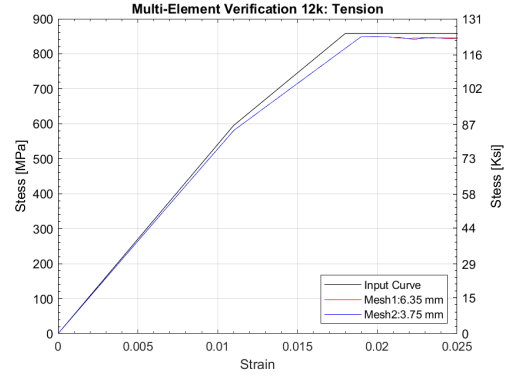
(b) 12k tension
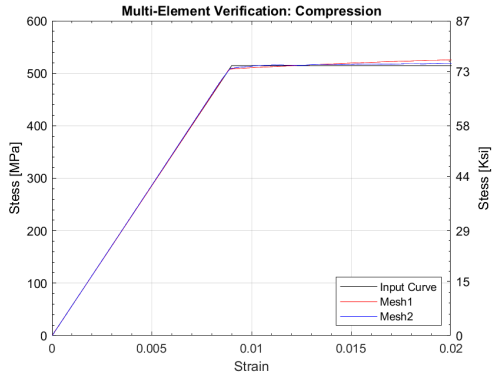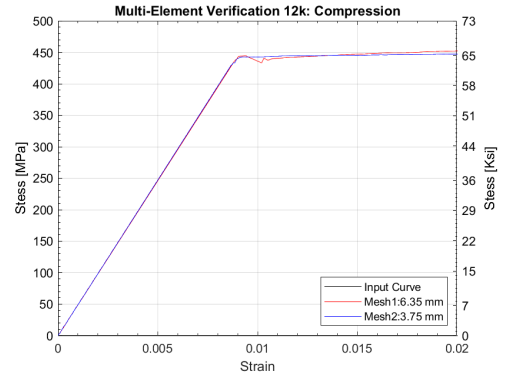
(c) 3k compression
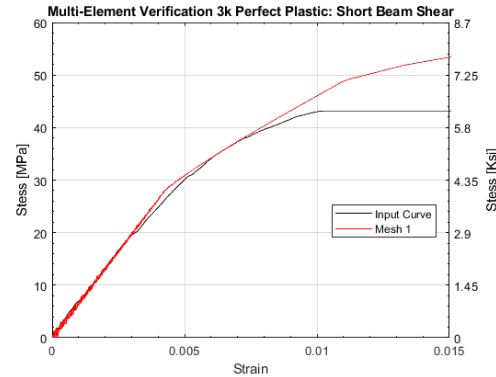
(d) 12k compression

(e) 3k short beam shear
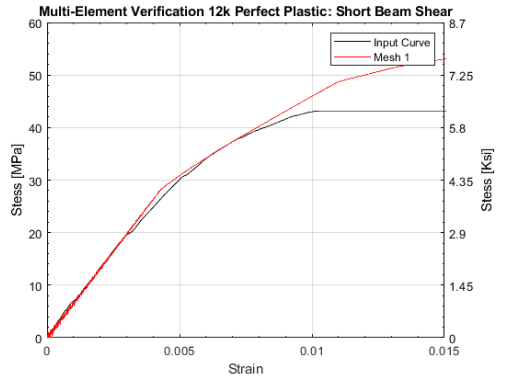
(f) 12k short beam shear

Figure 4.32: Coupon verification of (a-b) tension, (c-d) compression and (e-f) short beam shear models using perfectly plastic curves for 3k and 12k material, respectively.

120

Figure 4.33: Pendulum impact frame setup image showing mass tip in freefall.

The kinetic energy of a heavy mass on a rotating bar is define below as

$$E_{KE} = \frac{1}{2} m_N v_N{}^2 + \frac{1}{2} J_B \dot{\theta}^2 \tag{4.15}$$

Where J_B is the rotational inertia of the bar.

$$J_B = \frac{1}{3} m_B L_B^2 \tag{4.16}$$

Substituting Equation 4.16 to rearrange the kinetic energy

$$E_{KE} = \frac{1}{2} m_N v_N^2 + \frac{1}{2} \left(\frac{1}{3} m_B L_B^2 \right) \dot{\theta}^2 \tag{4.17}$$

The angular velocity can be related to the velocity a the tip mass and at bar center of mass, L_B, which is at midlength of the bar, with the following relation

$$\dot{\theta} = \frac{L_B}{v_B} = \frac{L_N}{v_N} \tag{4.18}$$

$$\dot{\theta} \approx \frac{L_B}{v_B} \approx \frac{L_N}{v_N} \tag{4.19}$$

Using Equation 4.18 to substitute into Equation 4.17 to get the kinetic energy as a function of angular velocity.

$$E_{KE} = \frac{1}{2} \left(m_N L_N^2 + \frac{1}{3} m_B L_B^2 \right) \dot{\theta}^2 \tag{4.20}$$

Similarity, the kinetic energy can be written as a function of the velocity at the tip

$$E_{KE} = \frac{1}{2} \left(m_N L_N^2 + \frac{1}{3} m_B \left(\frac{L_B^2}{L_N} \right)^2 \right) v_N^2 \tag{4.21}$$

which can be written as

$$E_{KE} = \frac{1}{2} \left(m_{eq} \right) v_N^2 \tag{4.22}$$

Where m_{eq} is the equivalent mass from the kinetic energy, Equation 4.21, and is defined as

$$m_{eq} = \left(m_N L_N^2 + \frac{1}{3} m_B \left(\frac{L_B^2}{L_N} \right)^2 \right) \quad (4.23)$$

The equivalent mass can be used to calculate the change in momentum, δp, using Equation 4.24

$$\Delta p = m_{eq} \left(v_{N,f} - v_{N,i} \right) \quad (4.24)$$

Additionally, the change in momentum can be related to the impulse using Equation 4.25

$$I = \Delta p \quad (4.25)$$

Where Impulse, I, is the area under the force history as defined in Equation 4.26.

$$I = \int_{t_1}^{t_2} F \, dt, \quad (4.26)$$

4.5.2   Wingbox Structure

The baseline geometry used in this investigation is representative of a composite wing box on an Unmanned Aerial Vehicle (UAV) with a high aspect ratio. The structure being investigated in this project is a long slender rectangular spar with a cross section as shown in Figure A.2. The structure consists of two c-channels bonded together with two rectangular plates to create a hollow box spar. Adhesively bonded composite wingbox was manufactured by bonding two 101.6 mm flat plates on the top and bottom and two c-channels for the right and left. Three VARTM infusions with a [0/+45/-45/90] layup were needed. First, a large 254 mm × 1270 mm plate was trimmed to get the top and bottom plates. The second and third infusions were performed to get c-channel parts. Figure A.3a in the Appendix shows manufacturing setup and fixtures used to bond parts together with structural paste adhesive. Additively manufactured parts were used on both ends to ensure proper spacing between channels. Manufacturing of a long single wingbox helps to reduce cost of manufacturing supplies that are single use by running fewer infusions.

Meshing of the laminated composite wingbox is done at the ply-by-ply approach in which the thickness of the element is set equal to the ply thickness. Tiebreak contact using a cohesive zone formulation between plies and at adhesive interface is used to model debond. The parameters used for the laminate and adhsieve are summarized in Table 4.11 which are based off [98, 99] The element size similar to the mesh convergence study at the coupon level v-notched rail shear verification tests was used in wingbox simulations. The modeling of the support structure is included to properly capture the boundary conditions. Displacement constraints are define at the nodes where the bottom support plate is attach to the pendulum system, as shown in Figure 4.35. Additionally, bolts are included in the support structure. The torque applied to the bolts in the experiments was not measure, therefore, pre-stressing of bolt parts in not included. A penalty based contact definitions with friction is added to the areas where the wingbox is in contact with the support plates. From
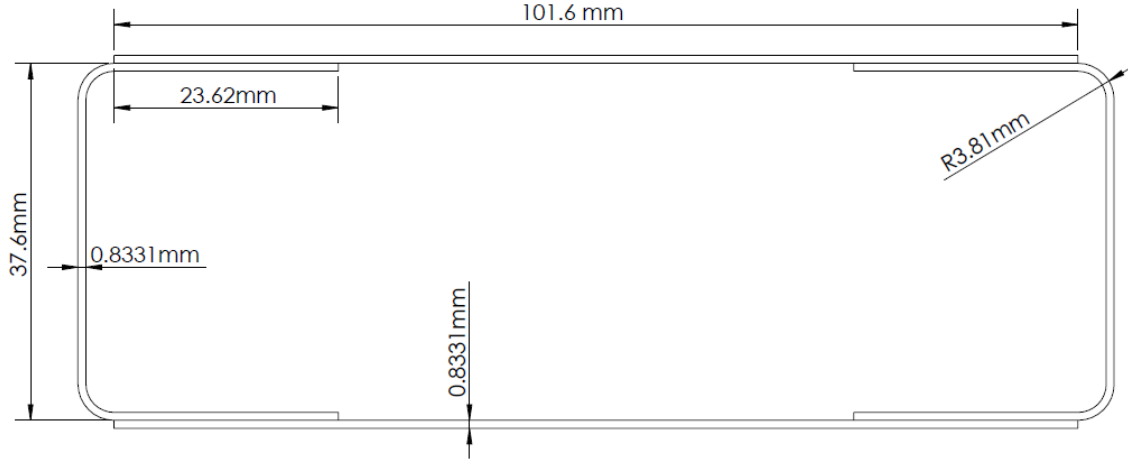
Figure 4.34: Wingbox cross section

Table 4.11: Tiebreak parameters using cohesive zone formulation

Parameter	Laminate	Adhesive
Normal Stiffness, Pa/m	1.6721e14	6.85E10
Tangent Stiffness,Pa/m	1.6721e14	23.2e10
Peak traction normal direction, MPa	27.58	12
Peak traction tangential direction, MPa	55.16	36
PExponent for mix mode	1	1
GIC, N m	750	1060
GIIC, N m	2539	2800

previous studies, it was found the the boundary conditions effect the impact response at low velocity [100]. It was seen that with fixed boundary conditions that the force increase greater than with simply supported boundary conditions with increasing velocity. Additionally, with increasing velocity the displacement decrease for the fully clamped boundary conditions.
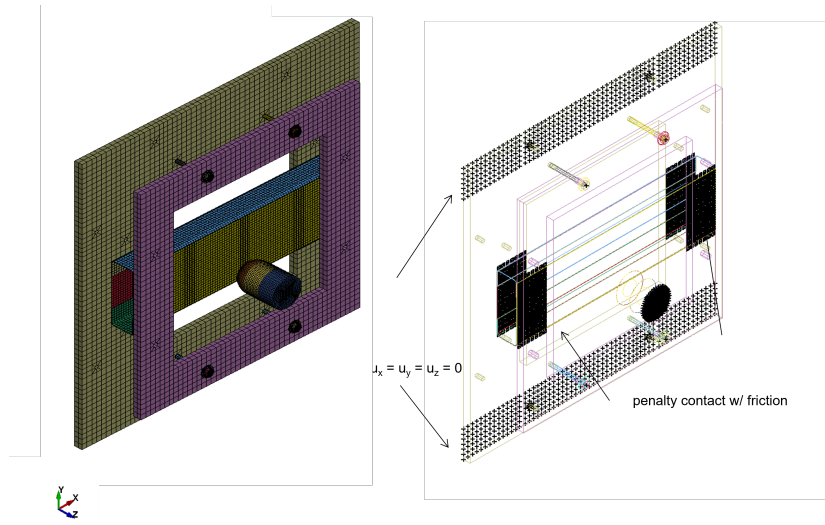
(a)
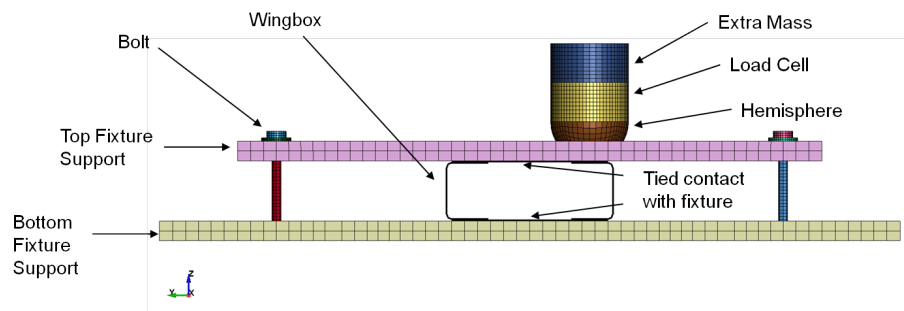
(b)
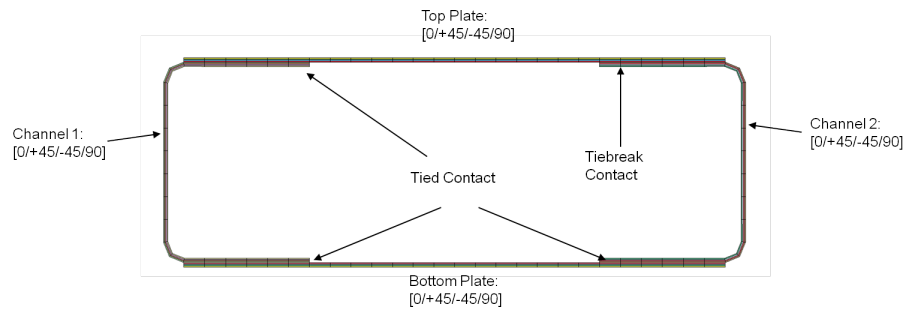
(c)

Figure 4.35: FEA model diagram for pendulum impact validation

126

4.5.3 Results

A matrix of experimental results are summarized in TableA.3. The experimental force history of three different energy levels: 5 J, 10 J, and 20 J are shown in Figure 4.37. The 5 J impact did not produce adhesive disbond damage that was detectable using pocket UT sensor. Whereas disbond of 1.25" and 2.0X" as shown in Figure 4.36 for the 10 J and 20 J impact, respectively. Additionally, from Figure 4.37 it can be seen that the 5 J force history follows a bell curve. Whereas the oscillation are seen in the 10 J and 20 J which are signs of damage. Also, the slope of unloading is less stiff compared to the loading.

Calibration of the wingbox model is done using the results from the 20 J low-velocity impact experiment with a 25.4 mm radius tip. A comparison the of the force history between experimental load cell and the section force from the simulation load cell is shown in Figures 4.38 and 4.39 for 5 J and 20 J energy levels. For the 5 J case, the simulation is ran with perfectly plastic input curves and force history has the same shape as the experiment but the peak force is under predicted. Performing more experiments would help to give a better idea of the experimental variation. For the 20 J case, the simulation with perfectly plastic curves matches the experiment well in the initial loading till peak stress, until which the simulation slightly overestimate the peak as seen in Figure 4.39. The wingbox model simulated with damage curves show a lower peak stress compared to the experimental. Both perfectly plastic and damage curves do not match the unloading response of the impact. The damage curves do a better job at matching the initial unloading. Additionally, the velocity of the impactor in the 20 J simulation is compared with the measured experimental out-bound velocity. When perfectly plastic curves are used the outbound velocity is larger than the experimental, whereas, when damage curves are used the outbound velocity is smaller than the experimental, as seen in Figure 4.40. The force history and change in velocity from both 20 J experiment and simulation are used to calculate impulse force and change in moment. The change

in moment and impulse in the experiment show very small difference (less than 1 %) which helps to verify experimental measurements. Comparing the experimental change in momentum with results from simulations it is seen that the perfectly plastic curves over predict the change in momentum, whereas, the damage curves under predict the response. Next, comparing the experimental impulse with simulations it is seen that impulse is under predicted for both input curves. The smaller impulse is due to the unloading response which occurs faster in the simulation compared to the experiment. It should be noted that the damage response in the material model occurs after peak stress. The present of damage before peak stress is possible which would need additional experiments to characterize.

Table 4.12: Comparison of 20 J impact of wingbox simulation with experiments

Specimen ID	Experiment WBIM-3	Simulation Perfectly Plastic	Simulation Damage
v_{out}, m/s	1.80	1.92	1.62
Δp, kg m/s,	22.8	23.4	21.8
I, N sec	22.9	18.6	17.6
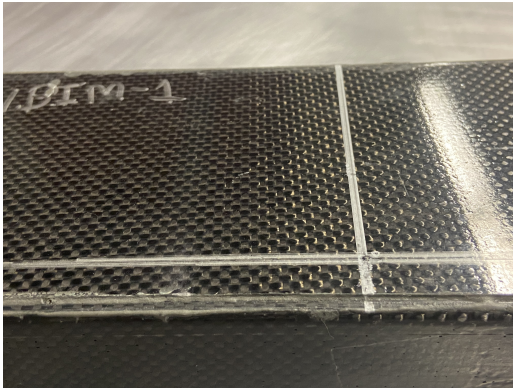
(a) 5 J

(b) 20 J
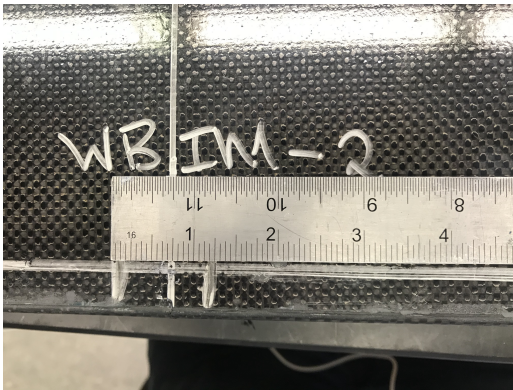
(c) 10 J

(d) 10 J

Figure 4.36: Post-impact images
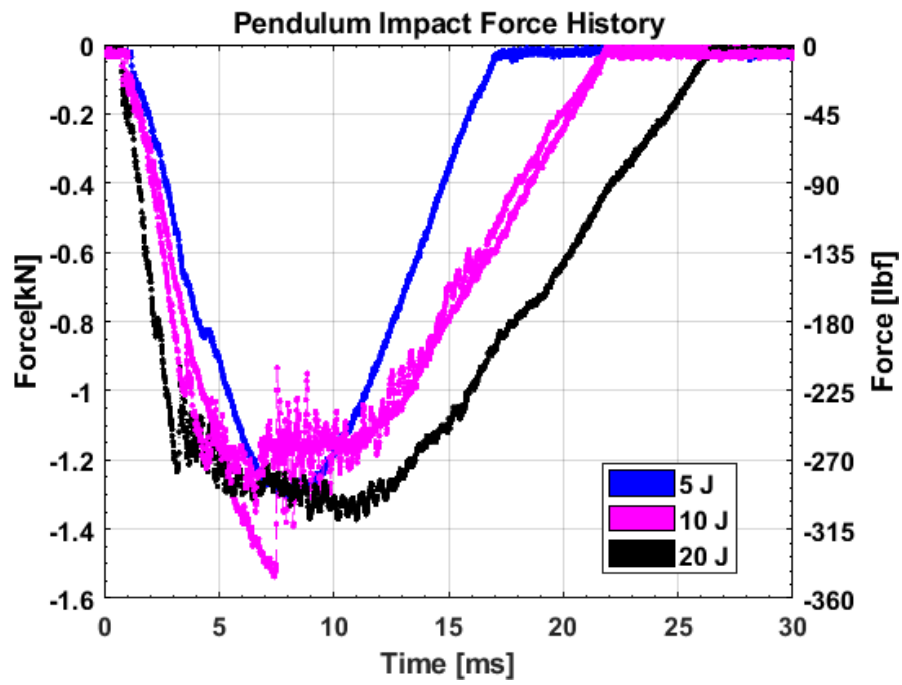
Figure 4.37: Wingbox force history
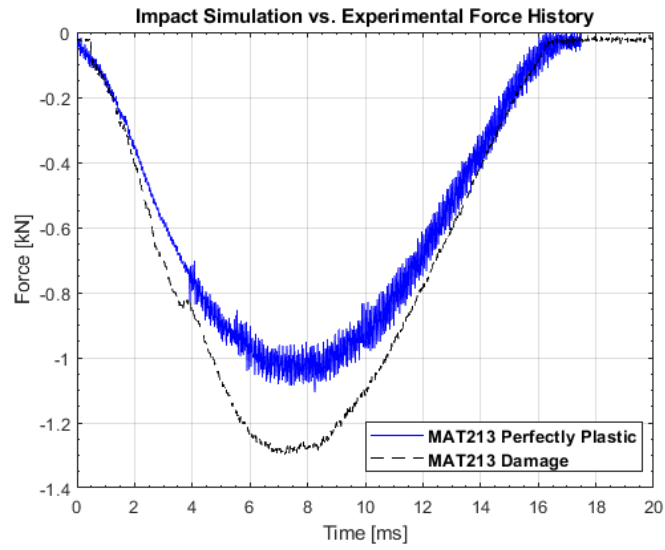
Figure 4.38: Force history comparison between experimental and simulation of 5 J impact energy
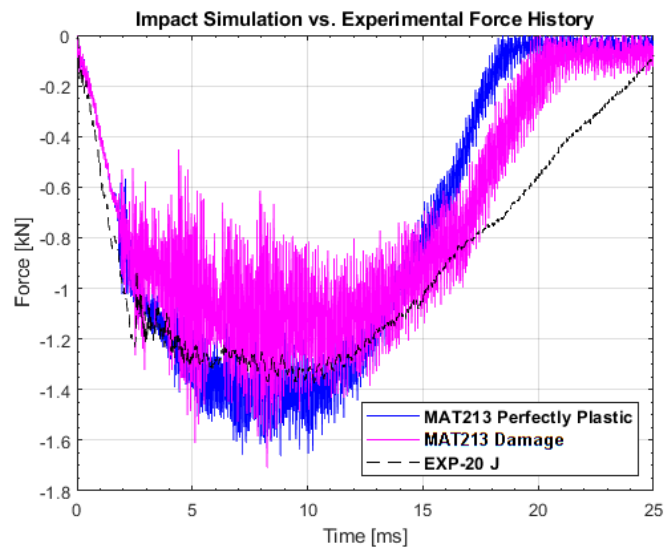
Figure 4.39: Force history comparison between experimental and simulation of 20 J impact energy

131
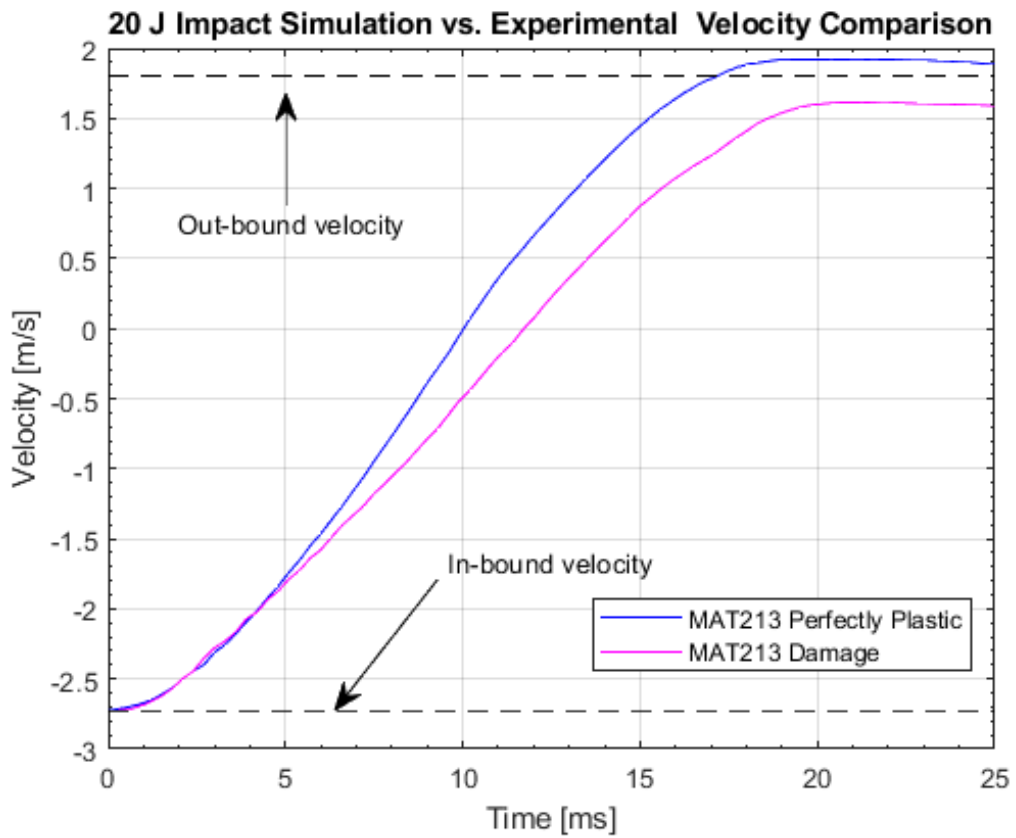
Figure 4.40: Velocity comparison between experimental and simulation of 20 J impact energy

4.6 Discussion

An experimental and analytical methodology that aims to capture the deformation mechanics of woven fiber composite materials found that non-homogeneous strain fields are present under in-plane tension and shear. Mesoscale damage from tow splitting was found to contribute to the specimen failure, especially for the larger 12k tow. Consideration of edge effects on the notch geometry needs to be further investigated to ensure material failure is not influenced by edge effects, especially relative to the tow geometry. The stress-strain response of short beam shear experiments were capture and the full RUC was captured for the 3k material. Specimen geometry did not allow for extraction areas to be sufficiently large enough to characterize the full 12k RUC. Effects of the undulation angle in the micromechanics were not considered in the this study. From experiments, the continuum response of the specimen was found to be heavily dependent on mesoscale tow behavior. Future studies are needed using a higher-fidelity plain weave RUC in which a continuous weave geometry is utilized to better calibrate experimental results with micromechanics analysis. Additionally, it was found that modeling the weave as homogeneous continuum is a big assumption due to the presence of high localized strains especially at the tows oriented transverse to the loading, and the growth of mesoscale damage. Finite element verification showed good agreement with experiments in elastic and small strains. At larger strains, the stress-strain behavior deviated from input curves. Additionally, from impact level validation studies the change in momentum from simulations with MAT213 compared well with experiments. However, the impulse force response from the simulations were lower compared to experiments. This highlights the need for characterization of the progressive damage that occurs before peak stress. This methodology does offer a framework to generate inputs for MAT213, or other advanced composites material models, for woven fiber architecture using limited experimental data.

Chapter 5

Defect Characterization in Additively Manufactured Metals

The following chapter is in preparation for publication which is a collaborative work with Lawrence Livermore National Laboratory (LLNL) that provided AM metals and California State University, Long Beach (CSULB) that is performing high speed mechanical experiments.

Two alloys (316L austenitic stainless steel and 300M maraging steel) were manufactured and machined by LLNL. Geometry of the axisymmetric tensile specimens with a 6.35 mm diameter is shown in Figure 5.1. Specimens were AM by laser powder bed fusion (LPBF) and include cylindrical volumes in the center of the specimens where the powder is not fused, as illustrated in Figure 5.2. These regions have a 1 mm radius and 10 mm length and contain mostly loose powder. These specimens represent the case where one large defect is present in the material. Half of the tensile specimens were heat treated to sinter the loose powder, followed by water quenching. The other half were left "as-built". To understand the effect that process induced fusion defects play on the loading rate effects of powder bed manufactured materials a set of samples are tested from quasi-static (QS) to intermediate loading rates.
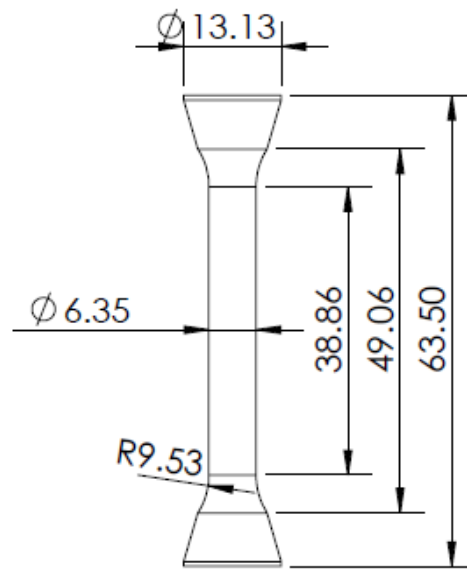
Figure 5.1: Axisymmetric tension specimen geometry.
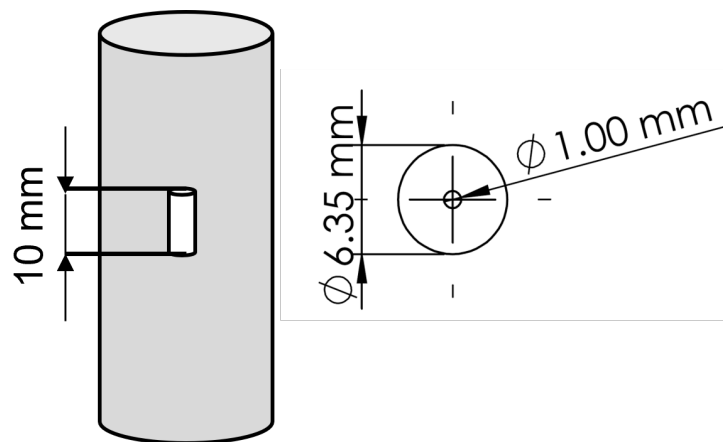
Figure 5.2: Illustration of cylinder fusion defect size; outer diameter of specimen is 6.35 mm and length of 1.00 mm diameter defect is 10 mm..

5.1 Test setup

QS to intermediate mechanical experiments are performed using an MTS 810 hydraulic test frame with 22 kip load capacity. V-serrated wedges are used to grip the tension fixture's 5/8" threaded rod ends, as shown in Figure 5.3. Threaded rods were high strength and smooth. The smoothness helps to reduces issues with alignment of the fixture assembly into the test frame. The fixtures uses a slotted housing bracket to connect the specimen to a threaded coupler as seen in Figure 5.3. Before inserting into slotted housing brackets, high strength aluminum split collars were attached to the specimen. A high strength aluminum is used to make parts reusable and to avoid collars from breaking due to the high strength of the steels. Additionally, a pivot block with rod ends is used to create moment releases and allow for a uniaxial load in the specimen. Once fixture is assembled in the load frame elastic pre-loading to 1 kN is applied to remove fixture slack.

For QS experiments, specimens are affixed with reflective tape which is used to measure displacement using a laser extensometer with a gage length of 20 mm and full scale reading of 100 mm. Additionally, displacement is measured using 2D digital image correlation (DIC). 2D DIC is not recommended for curved surfaces due to large out-of-plane errors. Here DIC is used to measure only axial strains since the specimen is curved. A Sony α6000 camera with a 105 mm Nikon Micro lens is used at QS rates to capture high resolution still images, 6000 px. $\times$ 4000 px., at 1 frame per second (fps). An Esper Triggerbox with two output channels turned on is used to trigger the camera. One of the channels is connected to the Sony camera to trigger the image capture. The second output channel is connected to the MTS controller data acquisition to time synchronize force measurements. It is recommend to use a data acquisition sampling frequency of 120 Hz to obtain a more defined pulse in the data. Sampling at a low frequency (i.e., 1-10 Hz.) makes it difficult to distinguish pulses. For intermediate loading rates, a Phantom v7.3 high speed camera with a

Half Bridge
350 Ω SG

Pivot block

Rod
ends

Al7075 Collars

Specimen

Slotted housing
bracket

Threaded coupler

Grade 8 steel threaded rod

⌀13.13

⌀6.35

38.86

49.06

63.50

R9.53
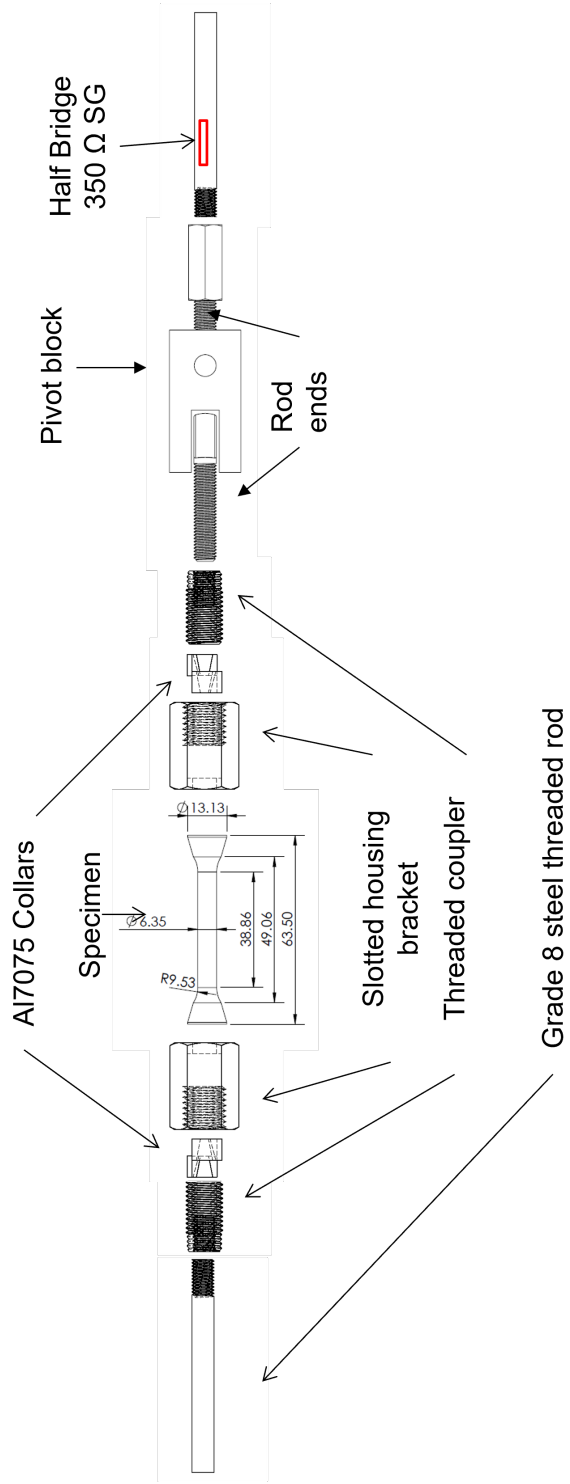
Figure 5.3: Quasi-static/intermediate tension fixture assembly

137

resolution of 600 px. × 208 px. and the same Nikon 105 mm lens was used to capture images at 3,000 fps and 16,000 fps for experiments at loaded at 10^{-1} s^{-1} rates. MTS TestWare was used to trigger the high-speed camera by sending to it a voltage pulse which is also recorded in the data acquisition file. To measure force at QS rates the load cell on the test frame is used. The test frame load cell is also used to calibrate two 350 Ω back-to-back strain gages in a half-bridge configuration (i.e. custom built load cell) that were attached to the top threaded rod of the test fixture, as seen in Figure 5.3. Force measured in the rod is used to calculate stress in the specimen at intermediate loading rates. Force in the rod is used instead of the MTS system's load cell measurement due to inertia effects from the mass of the hydraulic grips (30 kg).

For DIC, the entire specimen region in the camera field of view (FOV) is analyzed as illustrated in Figure 5.5. A virtual extensor, which is the same length as the gage used for the laser extensometer and located along the center of the specimen is used to measure local displacement, as shown in Figure 5.5. Markings on the specimen were added to facilitate virtual extensometer placement. LED lights are used when capturing QS images, whereas, at intermediate loading halogen lights are used due to the fast shutter speed with the high speed camera. For intermediate experiments, only DIC displacements are measured due to sensor limitations with the laser extensometer. All DIC analysis is performed using VIC-2D 6 with Gaussian weighted subsets, optimized 8-tap interpolation function, and a zero-mean normalized sum of squared difference (ZMNSSD) correlation criteria. Incremental DIC is used due to large plastic deformation seen in metals. A speckle with length roughly 5 to 7 px. was used for intermediate loading experiments with a low image resolution. This same speckle was used for QS experiments. Key DIC parameters for VIC-2D 6 are summarized in Table 5.1.

138
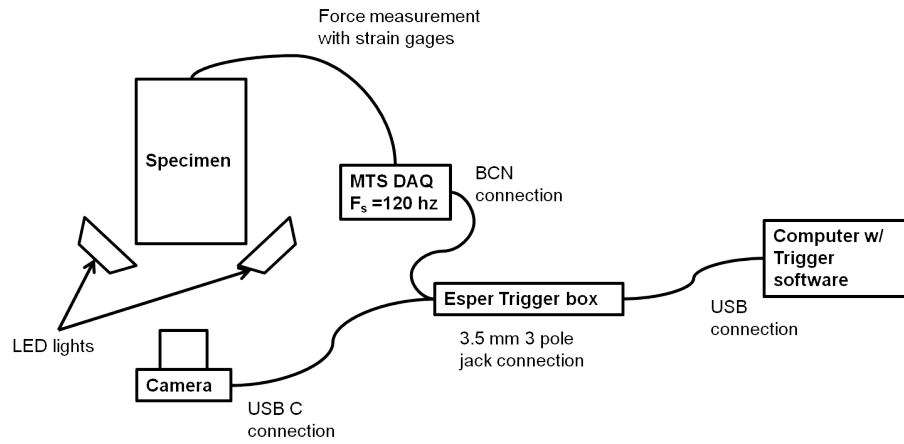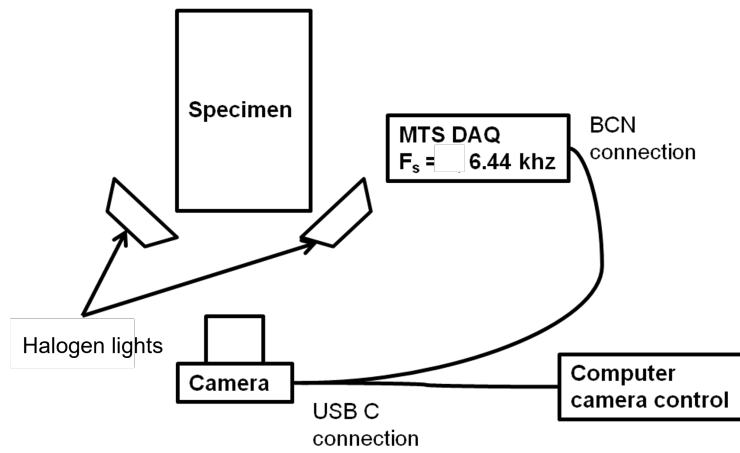
Figure 5.4: Test setup for AM tension experiments at (a) quasi-static and (b) intermediate loading .
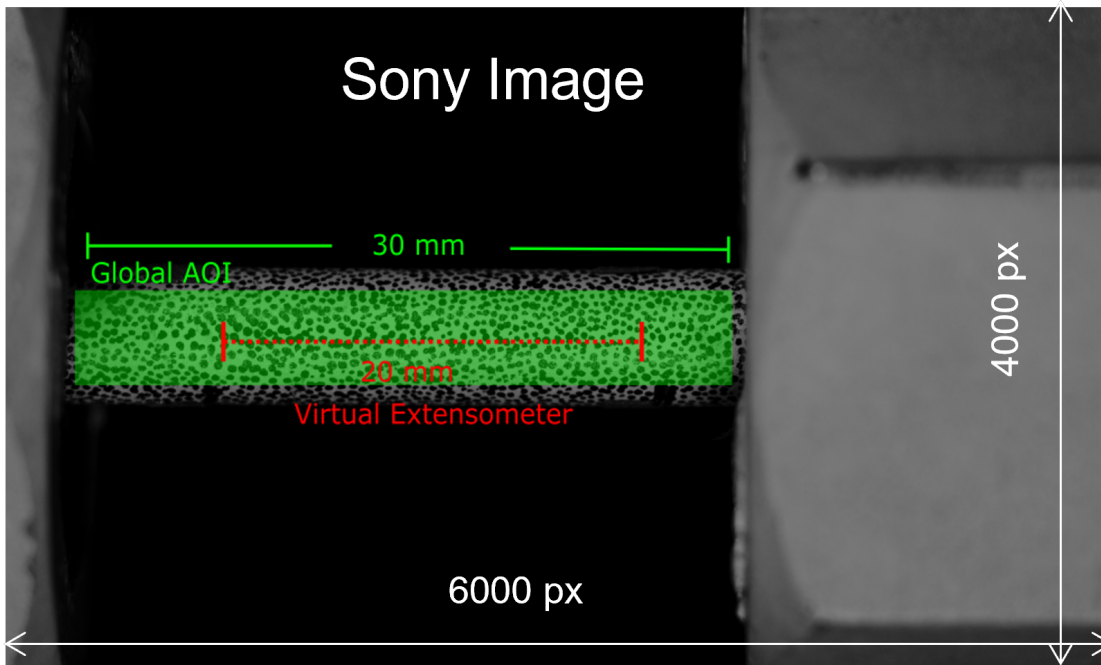
Figure 5.5: DIC area of interest (AOI) for AM tension specimen.

Table 5.1: DIC parameters for AM shear experiments with VIC-2D 6 software.

Loading Rate	0.033 mm/s	3.3 mm/s	33 mm/s
Camera	Sony	Phantom	Phantom
Camera Resolution	6000 x 4000	600 x 208	600 x 208
Frame Rate (fps)	1	3,000	16,000
Scale Factor	0.009	0.076	0.076
Subset Size (px)	95	19	19
Step Size (px)	5	1	1
Strain Filter (px)	5	5	5
VSG (mm)	1.0	1.7	1.7

5.2 Results

A test matrix showing a summary of specimens tested is shown in Table 5.2. Specimens are loaded till fracture. Images of experiments from high speed camera loaded at at 10^{-1} s^{-1} and recorded at 3,000 fps show significant necking occurring before fracture in the as-built 316L material as seen in Figure 5.6a. From camera images it is seen that once fracture occurs in the as-built 316L material and the specimen splits in half, loose powder is left exposed as shown in Figure 5.6b. Additionally, it was observed that once the specimen fails, powder and material fragments flew in the air. A N95 mask was worn during subsequent tests to avoid inhalation of harmful toxins. This was seen most pronouncedly in the as-built material. Specimens manufactured with the 316L powder with heat treatment applied showed increased ductility in the specimen as seen in Figure 5.6c. For both as-built and heat treated 316L necking occurs at the specimen center where the fusion defect is located. Additionally, in the heat treated 316L specimens, the loose powder is no longer seen at fracture. The as-built 300M material shows brittle fracture with little signs of necking occuring before fracture as seen in Figure 5.7a. Fracture occurs too quickly and exposed powder, which was seen in the as-built 316L, is not observed for the as-built 300M. For the 300M specimens, heat treatment resulted in an in increase the amount of necking at the specimen center, as seen in Figure 5.7d, compared to the as-built specimens in Figure 5.7a.

Table 5.2: AM tension test matrix

Loading rate, in/s	as-built 316L	as-built 300M	316L (HT)	300M (HT)
0.0015	3	3	2	3
0.015	2	3	3	3
0.15	3	3	3	3
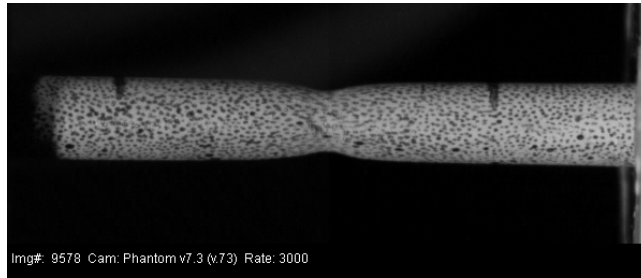
(a) as-built 316L at necking
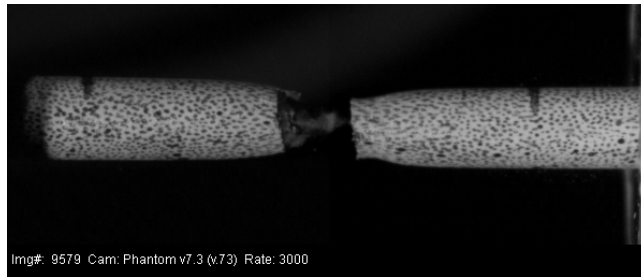
(b) as-built 316L at fracture
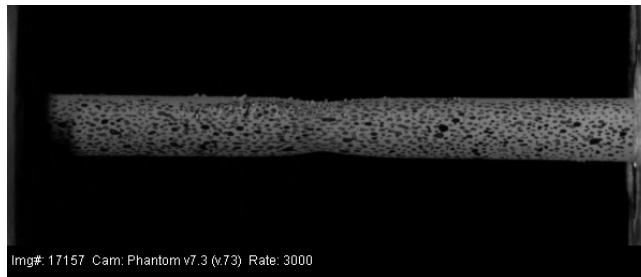
(c) heat treated 316L at necking
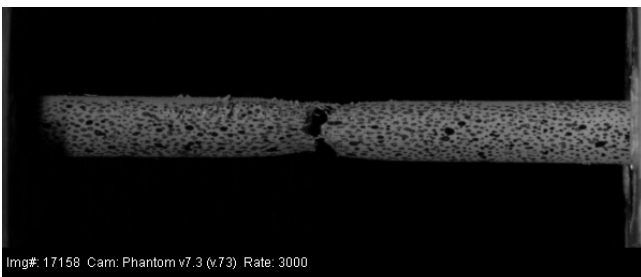
(d) heat treated 316L at fracture

Figure 5.6: High-speed camera images of 316L specimen at necking and fracture.
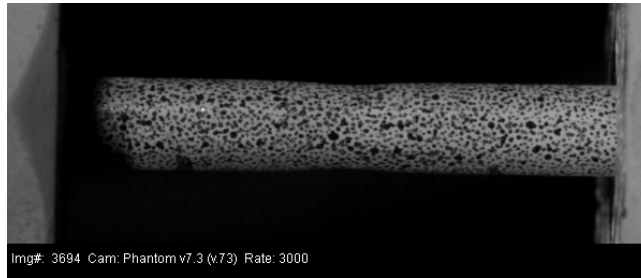
(a) as-built 300M at necking
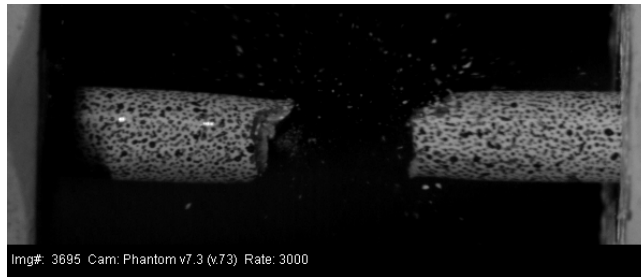
(b) as built 300M at fracture
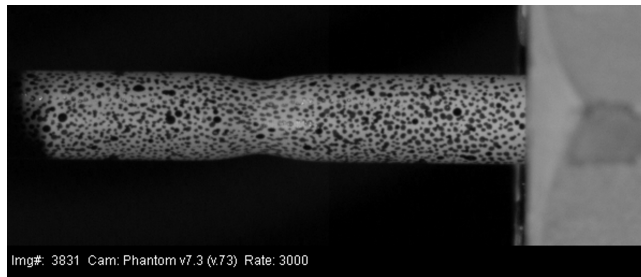
(c) heat treated 300M at necking
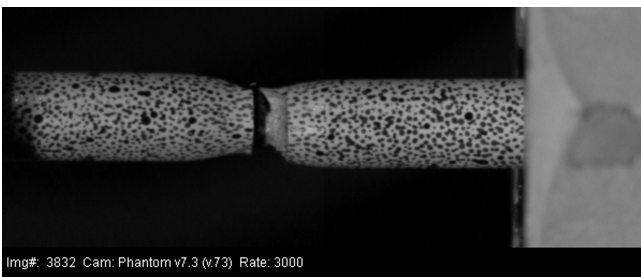
(d) heat treated 300M at fracture

Figure 5.7: High-speed camera images of 300M specimen at necking and fracture.

Optical microscope images of tested specimens are shown in Figure 5.8 and 5.9 for the 316L and 300M materials, respectively. For the as-built specimens, a circular void where the the fusion defect was manufactured can be clearly seen in Figures 5.8a and 5.9a for the 316L and 300M materials, respectively. For the heat treated specimens, the circular shape of the defect can be seen but there is no longer a void. Signs of porosity are seen in the as-built 316L, heat treated 316L and heat treated M300 material as seen in Figures 5.8c and 5.9c, respectively. Porosity is not visibly seen in microscope image of the 300M specimen. Fracture surfaces for the 316L material show a more jagged texture indicative of ductile fracture which is shown in Figure 5.8. Around the edges of the specimen the microscope images show an uneven surface that is created due to necking which is seen in the as-built 316L, heat treated 316L and the heat treated 300M. These specimens showed visible signs of area reduction during necking from high speed camera images. The as-built 300M did not show significant signs of necking from high speed camera images or the fracture surface image as shown in Figures 5.9a, which had a flatter surface indicative of brittle fracture.

DIC contours images before facture occurs in QS experiments for 316L and 300M are shown in Figure 5.10 which show large strain localization occurring at the center. At QS loading a 5% and 4% difference between virtual extensometer failure strain from DIC and laser extensometers measurements is observed for 316L and 300M experiments, respectively. Next, the strain history from virtual extensometer is plotted in Figures 5.11a and 5.11b for the three different loading rates 10^{-3}, 10^{-1}, and 10^0 s^{-1}. The 316L and 300M experiments with as-built specimens are plotted with dashed lines and heat treated specimens are plotted with solid lines. From Figure 5.11a and 5.15a it can be seen that at intermediate loading the failure strain decreases by 24% and 14% compared to QS static experiments for as-built and heat treated 316L material, respectively. For as-built 300M increasing the strain rate leads to little changes (1%) in the failure strain, whereas, for the heat treated 300M failure

144
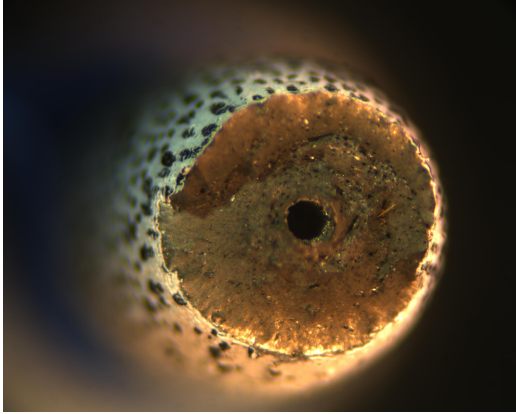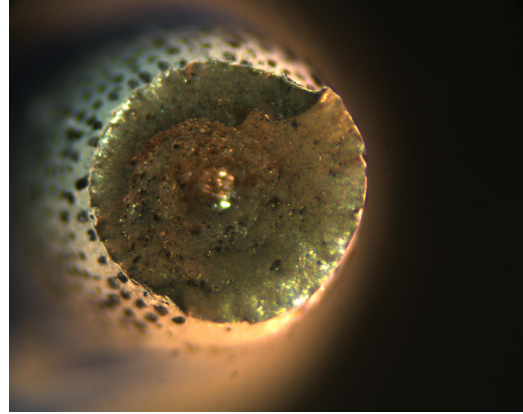
(a) as-built 316L

(b) as-built 316L
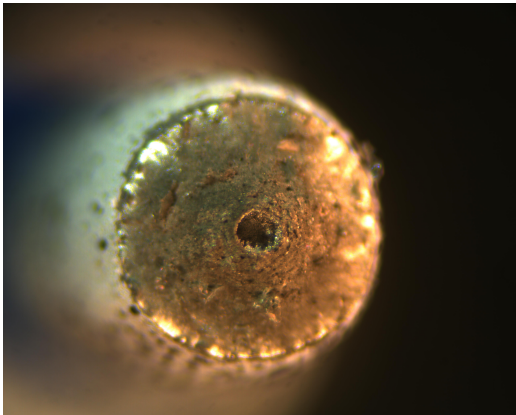
(c) heat treated 316L
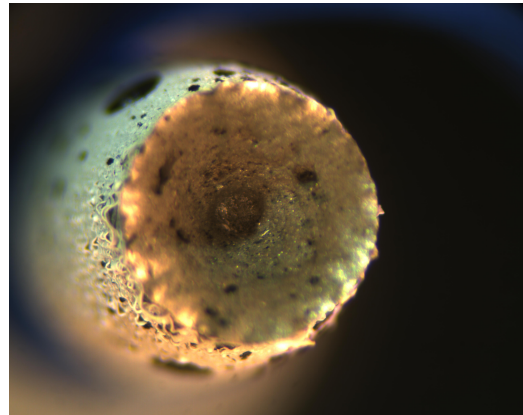
(d) heat treated 316L

Figure 5.8: Optical microscope images of fracture surfaces of 316L tested specimens. Prior to testing specimen diameter 6.35 mm.
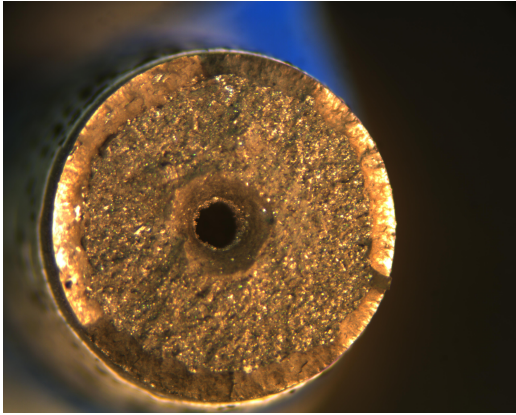
(a) as-built 300M
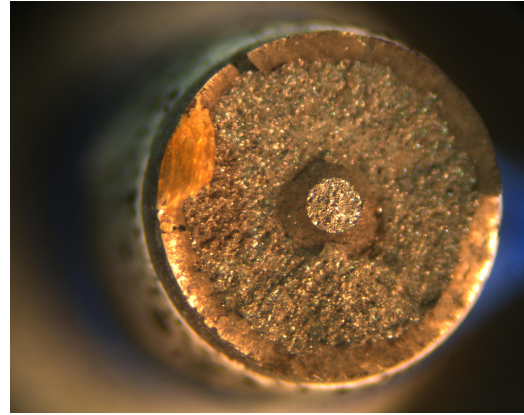
(b) as-built 300M
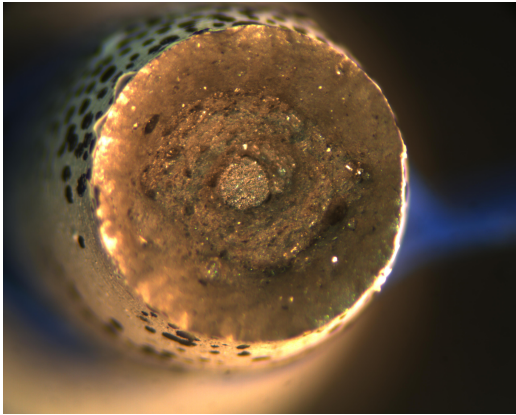
(c) heat treated 300M
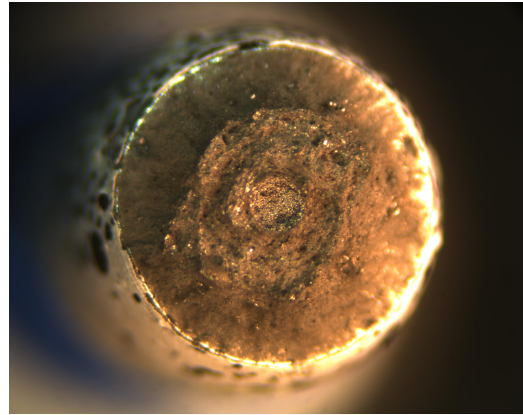
(d) heat treated 300M

Figure 5.9: Optical microscope images of fracture surfaces of 300M tested specimens. Prior to testing specimen diameter 6.35 mm.

strains are observed to be larger at intermediate loading. It was noted that during QS experiments of heat treated 300M specimens error from load frame controller (as seen in Figure 5.12b) is observed which can explain a lower failure strain at QS loading compared to intermediate loading.
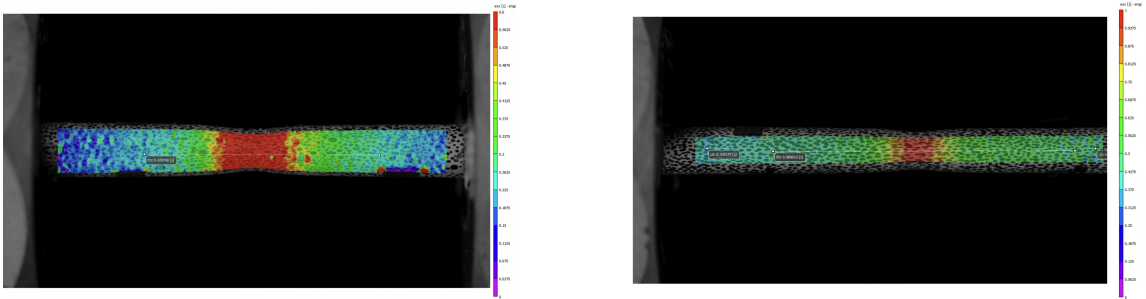
(a) as-built 316L

(b) heat treated 316L
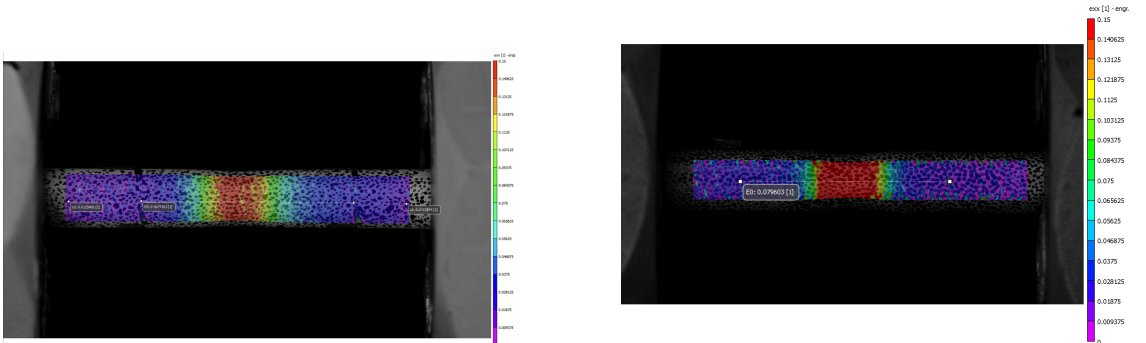
(c) as-built 300M

(d) heat treated 300M

Figure 5.10: Engineering strain, ε_{xx}, contours before fracture.
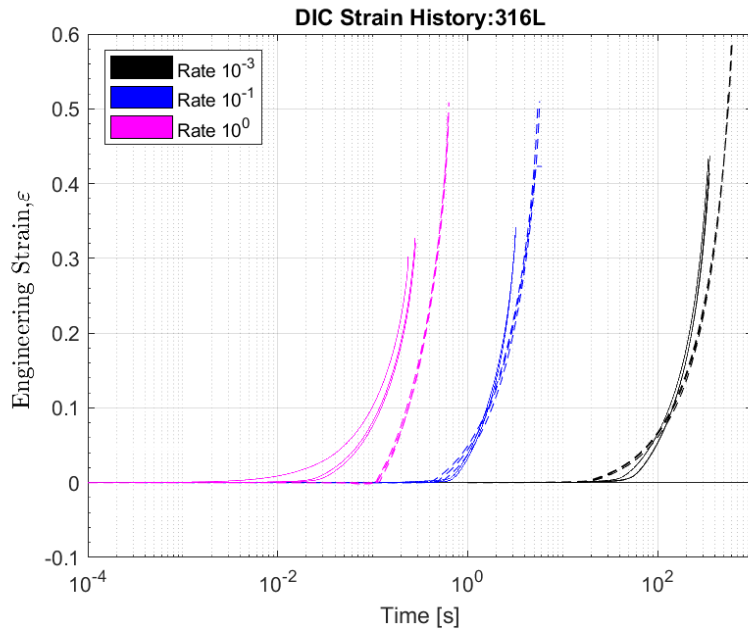
(a)
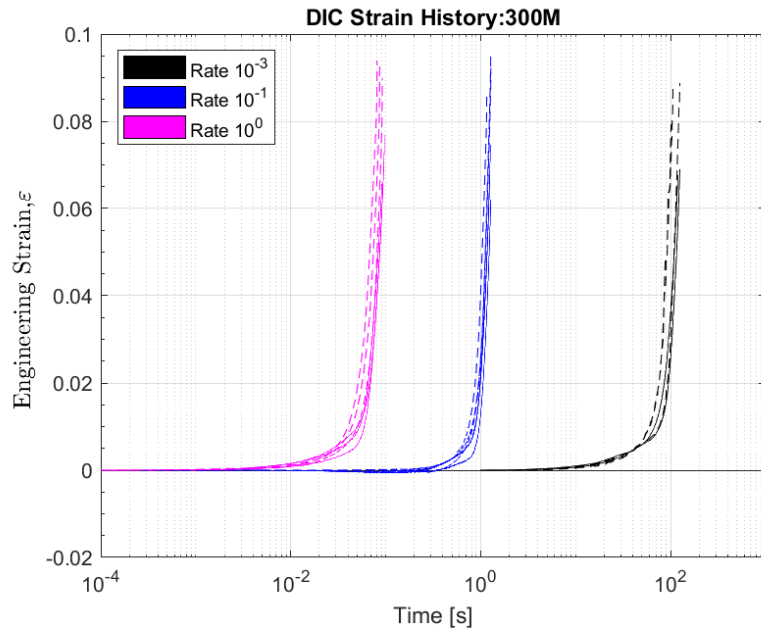
(b)

Figure 5.11: Digital Image Correlation strain history at different loading rates for (a) 316L and (b) 300M materials

Additionally, the virtual extensomter from DIC analysis is used with local force measurements to determine stress-strain curves as shown in Figure 5.12. The heat treated 316L specimens showed a decrease in yield and ultimate strength compared to the as-built specimens as seen in Figure 5.13. Similarly, the heat treated M300 specimens are observed to have a lower yield and ultimate strength compared to the as-built specimens as seen in Figure 5.14. For the 316L specimens, the yield strength increases by 9% and 24% at intermediate loading rates compared to QS loading for the as-built and heated specimens, respectively. The ultimate strength increases by 6% for the as-built 316L specimens, whereas, the heat treated 316L experiments show a 2% increase.

5.3   Discussion

Experiments from this study provide techniques to characterize AM metals with defects. Uniaxial tension experiments performed in this study of AM metals with fusion defects tested at intermediate loading rates show that the fracture and strength properties of AM metals are strongly dependent on heat treatment. For 316L the combined effect of heat treatment and loading rate showed an decrease in the strength and failure strain compared to as-built specimens. High speed camera and optical microscope images show that heat treatment increases the ductility when compared to the as-built for both steels. For M300, heat treatment changed the the fracture behavior from brittle to ductile.
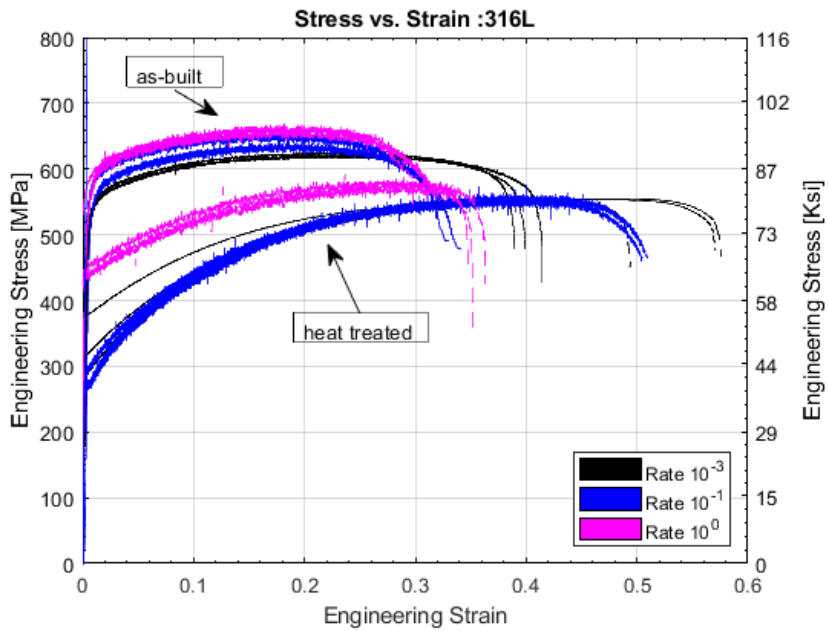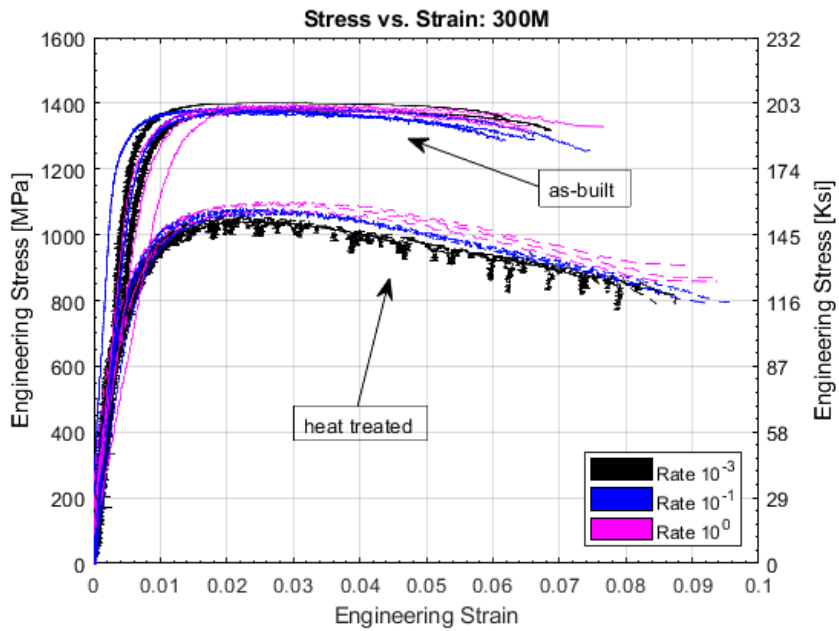
Figure 5.12: Stress-strain curves for (a) 316L and (b) 300M materials

150
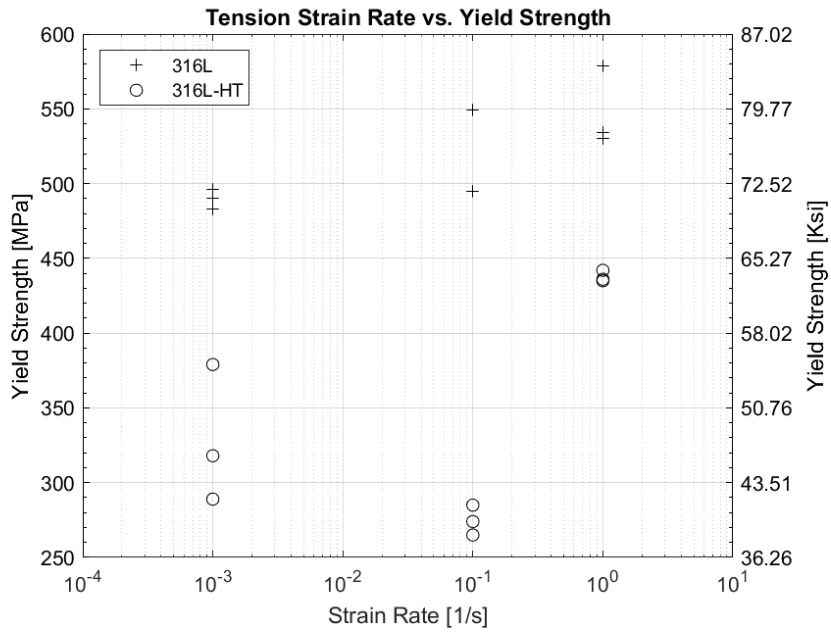
(a)
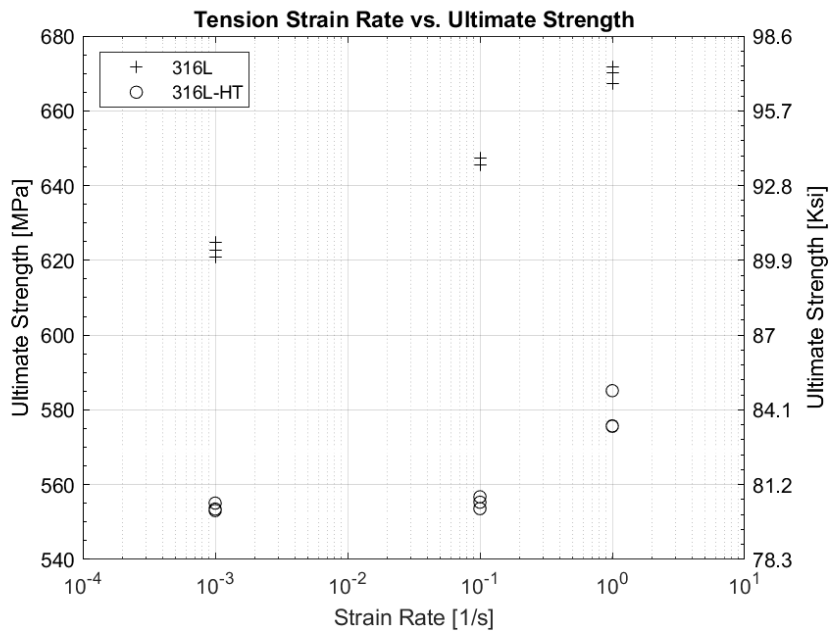
(b)

Figure 5.13: 316L strain rate effects of (a)yield strength and (b) ultimate strength

151
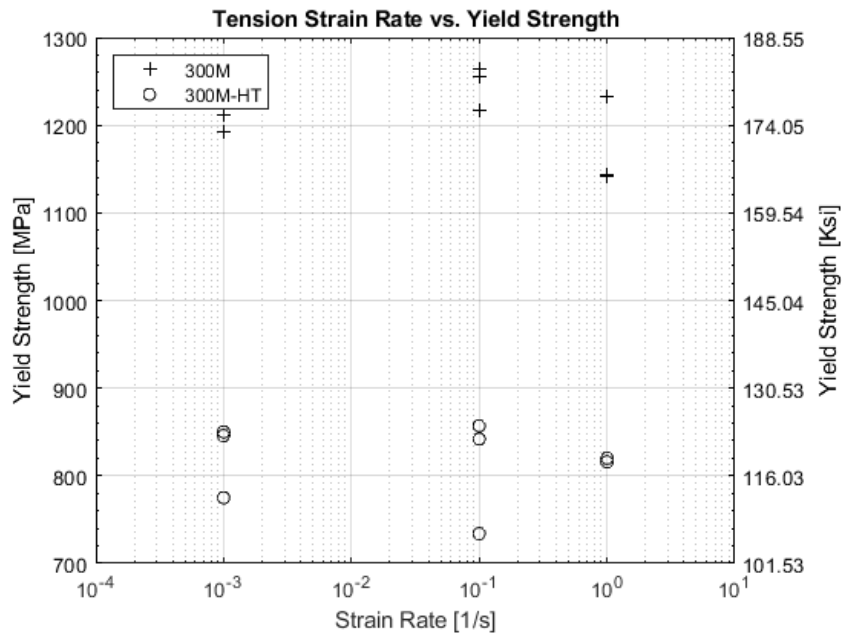
(a)
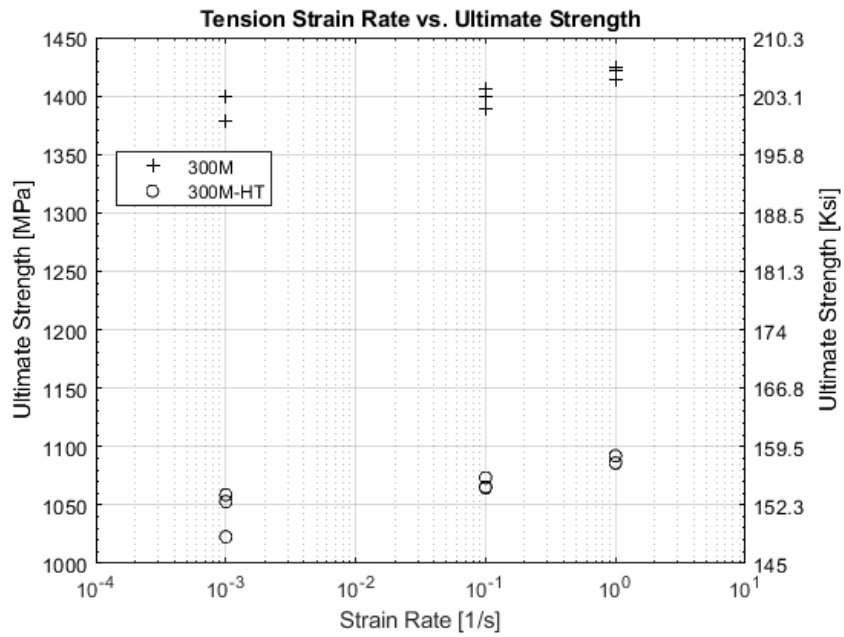
(b)

Figure 5.14: 300M strain rate effects of (a) yield strength and (b) ultimate strength
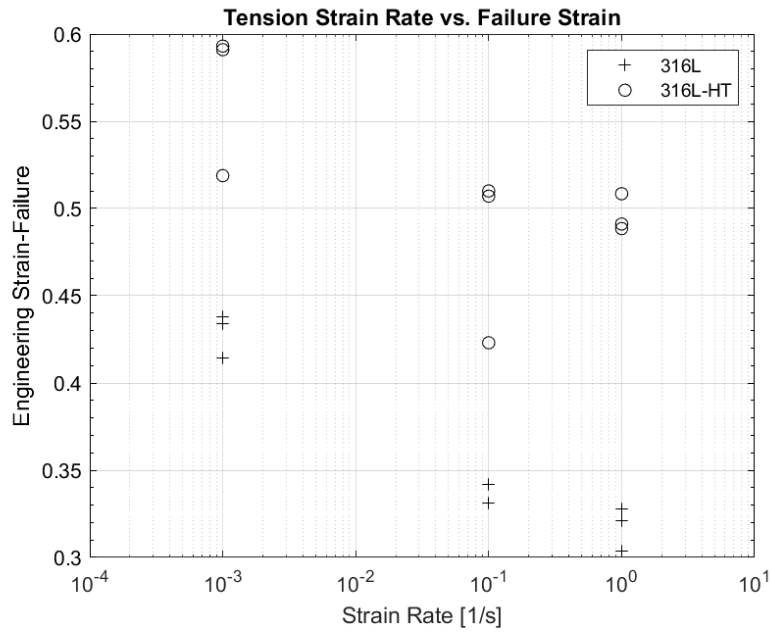
(a)
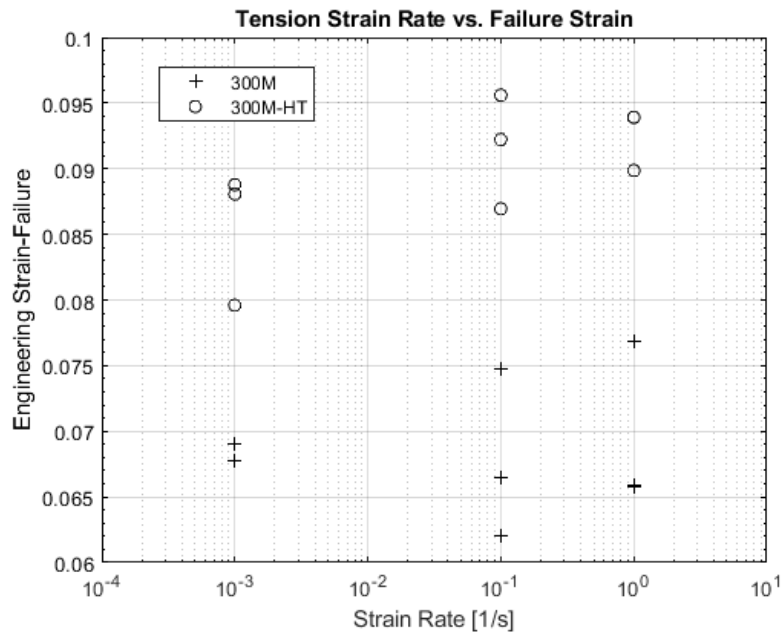
(b)

Figure 5.15: Strain rate effects on failure strain of (a) 316L and (b) 300M

Chapter 6

Conclusions

This dissertation investigated the stress-strain behavior of woven polymer matrix composites and additively manufactured metals under intermediate loading rates. In Chapter 3, a comprehensive characterization of two woven polymer matrix composites is discussed. At quasi-static loading rates high resolution images are analyzed using digital image correlation to capture displacements fields. Inhomogeneous strain fields were observed due to progressive mesoscale damage in the fiber tow bundles before peak stress. This corroborates previous works on triaxially braided textile composites [60]. Additionally, for woven composites, a non-standard shear fixture and specimen were designed to capture the rate-dependent in-plane shear stress-strain response. In-plane shear experiments at intermediate loading rates showed an increase in strength and modulus compared to quasi-static loading. Results from high speed camera images help to observe the specimen behavior at peak load, but raises new questions about the load carrying capacity past peak load.

In Chapter 4, a hybrid experimental-numerical methodology was developed that efficiently characterized the 3D response of woven composites. The repeating unit cell is found to influence the behavior of the material. Results from micromechanics analysis compared well with available experimental data, however, simplification of

154

the mesoscale undulation angle limits evolution of damage that occurs in experiments. While detailed characterization of the repeating unit cell was not done, the approach taken demonstrates an efficient method to develop comprehensive material databases. Verification and validations studies of the characterization methodology developed in this dissertation is performed for 3k and 12k plain weave materials using MAT213 in LS-DYNA. Simulation results showed good agreement with experimental data. Additionally, a validation study showed the ability to use MAT213 to model of low-velocity impact on a wingbox structure. Results from wingbox study show good agreement with the change in momentum observed in the experiment, however, the impulse from the simulation was under-predicted compared to the experiment. This highlights the need for damage characterization that occurs in woven composites before peak stress.

The stress-strain behavior in additively manufacture metals with fusion defects discussed is presented in Chapter 5. The stress-strain behavior dependency on heat treatment and loading rate are captured using digital image correlation. Results from characterization using high speed camera and optical microscopy images showed that as-built specimens with defects behave less ductile and stronger compared to specimens that received heat treatment.

This work expanded on previous studies by Littel [60] and Khaled et al. [2]. Littel performed research on the macromechanical shear behavior of a single fiber architecture at quasi-static rates. The work shown in Chapter 3 expands the understanding of the effect that the fiber architecture has on the shear response by investigating two woven materials that were loading at multiple rates. Khaled et al. [2] performed research on the experimental and numerical characterization for MAT213 only on unidirectional composites. The work presented in this dissertation establishes experimental and numerical techniques to extract stress-strain inputs for woven composites.

6.1 Future Research Directions

This work highlights several areas of improvement and research directions. For woven composites, further characterization of the fiber architecture with improved meso-scale models that better capture the variation in the tow are needed. In particular, the effects of the tow undulation and interaction between tows are aspects that need more detailed focus. Further development of the shear fixture to better asses the damage that occurs before peak stress would allow for low cycle fatigue experiments to capture stiffness reduction due to damage accumulation. Additionally, to better model impact on composites structures, development of interlaminar fracture experiments that can be robustly used with MAT213 should be considered.

For AM defects, further characterization of the fracture surfaces using scanning electron microscopy would allow better understanding the microstructure around the defect. Additionally, work in this dissertation only investigated specimens manufactured in the build direction (z axis), further investigation into different orientations should be looked at to better understand the the role of defects and manufacturing induced variations.

Bibliography

[1] A. Standard, "ASTM F2792-12a: standard terminology for additive manufacturing technologies," *ASTM International*, vol. 63, pp. 4–11, 2013.

[2] B. Khaled, L. Shyamsunder, C. Hoffarth, S. D. Rajan, R. K. Goldberg, K. S. Carney, P. DuBois, and G. Blankenhorn, "Experimental characterization of composites to support an orthotropic plasticity material model," *Journal of Composite Materials*, vol. 52, no. 14, pp. 1847–1872, 2018.

[3] C. Hoffarth, S. D. Rajan, R. K. Goldberg, D. Revilock, K. S. Carney, P. DuBois, and G. Blankenhorn, "Implementation and validation of a three-dimensional plasticity-based deformation model for orthotropic composites," *Composites Part A: Applied Science and Manufacturing*, vol. 91, pp. 336–350, 2016.

[4] L. Shyamsunder, B. Khaled, S. D. Rajan, R. K. Goldberg, K. S. Carney, P. DuBois, and G. Blankenhorn, "Implementing deformation, damage, and failure in an orthotropic plastic material model," *Journal of Composite Materials*, vol. 54, no. 4, pp. 463–484, 2020.

[5] K. E. Jackson, R. K. Goldberg, T. M. Ricks, R. T. Haluza, and J. Buenrostro, "Application of a developmental composite material model to predict the crush response of two energy absorbers," tech. rep., 2021.

[6] J. Harrington, C. Hoffarth, S. D. Rajan, R. K. Goldberg, K. S. Carney, P. DuBois, and G. Blankenhorn, "Using virtual tests to complete the description of a three-dimensional orthotropic material," *Journal of Aerospace Engineering*, vol. 30, no. 5, p. 04017025, 2017.

[7] J. Aboudi, S. M. Arnold, and B. A. Bednarcyk, *Micromechanics of composite materials: a generalized multiscale analysis approach*. Butterworth-Heinemann, 2013.

[8] B. N. Cox and G. Flanagan, "Handbook of analytical methods for textile composites," tech. rep., 1997.

[9] D30 Committee, "ASTM D3039/D3039M: Standard Test Method for Tensile Properties of Polymer Matrix Composite Materials," *Annual Book of ASTM Standards*, pp. 1–13, 2014.

[10] D30 Committee, "ASTM D6641/D6641M-16e1: Standard Test Method for Compressive Properties of Polymer Matrix Composite Materials," *ASTM International*, vol. 03, no. 2008, pp. 1–13, 2016.

[11] D20 Committee, "ASTM D695: Standard Test Method for Compressive Properties of Rigid Plastics," *ASTM International*, 2010.

[12] A. Makeev, Y. He, P. Carpentier, and B. Shonkwiler, "A method for measurement of multiple constitutive properties for composite materials," *Composites Part A: Applied Science and Manufacturing*, vol. 43, no. 12, pp. 2199–2210, 2012.

[13] J. D. Littell, W. K. Binienda, G. D. Roberts, and R. K. Goldberg, "Characterization of damage in triaxial braid composites under tensile loading," tech. rep., 2009.

[14] A. Gilat and J. D. Seidt, "Compression, tension and shear testing of fibrous composite with the split Hopkinson bar technique," in *EPJ Web of Conferences*, vol. 183, p. 02006, EDP Sciences, 2018.

[15] R. E. Chavez Morales, *Dynamic Response of Polymeric Materials Subject to Extreme Environments Under Dynamic Fracture and Impact Conditions*. PhD thesis, UC San Diego, 2020.

[16] L. W. Kohlman, *Evaluation of Test Methods for Triaxial Braid Composites and the Development of a Large Multiaxial Test Frame For Validation using Braided Tube Specimens*. The University of Akron, 2012.

[17] W. Wijaya, M. Ali, R. Umer, K. Khan, P. Kelly, and S. Bickerton, "An automatic methodology to ct-scans of 2d woven textile fabrics to structured finite element and voxel meshes," *Composites Part A: Applied Science and Manufacturing*, vol. 125, p. 105561, 2019.

[18] I. Verpoest and S. V. Lomov, "Virtual textile composites software wisetex: Integration with micro-mechanical, permeability and structural analysis," *Composites Science and Technology*, vol. 65, no. 15-16, pp. 2563–2574, 2005.

[19] H. Lin, L. P. Brown, and A. C. Long, "Modelling and simulating textile structures using texgen," in *Advanced Materials Research*, vol. 331, pp. 44–47, Trans Tech Publ, 2011.

[20] B. A. Bednarcyk and S. M. Arnold, "Micromechanics-based modeling of woven polymer matrix composites," *AIAA journal*, vol. 41, no. 9, pp. 1788–1796, 2003.

[21] K. Liu, *Micromechanics based multiscale modeling of the inelastic response and failure of complex architecture composites.* Arizona State University, 2011.

[22] C. Sorini, A. Chattopadhyay, and R. K. Goldberg, "An improved plastically dilatant unified viscoplastic constitutive formulation for multiscale analysis of polymer matrix composites under high strain rate loading," *Composites Part B: Engineering*, vol. 184, p. 107669, 2020.

[23] I. M. Daniel, O. Ishai, I. M. Daniel, and I. Daniel, *Engineering mechanics of composite materials*, vol. 1994. Oxford university press New York, 2006.

[24] T. Ishikawa and T.-W. Chou, "One-dimensional micromechanical analysis of woven fabric composites," *AIAA journal*, vol. 21, no. 12, pp. 1714–1721, 1983.

[25] J. O. Hallquist *et al.*, "LS-DYNA keyword user's manual," *Livermore Software Technology Corporation*, vol. 970, pp. 299–800, 2007.

[26] D. Systèmes, "Abaqus analysis user's guide," *Solid (Continuum) Elements*, vol. 6, p. 2019, 2014.

[27] S. W. Tsai and E. M. Wu, "A general theory of strength for anisotropic materials," *Journal of composite materials*, vol. 5, no. 1, pp. 58–80, 1971.

[28] R. Krueger, "An approach for assessing delamination propagation capabilities in commercial finite element codes," 2007.

[29] K. Song, C. G. Dávila, and C. A. Rose, "Guidelines and parameter selection for the simulation of progressive delamination," in *2008 ABAQUS User"s Conference*, 2008.

[30] D30 Committee, *ASTM D5528-13 Standard Test Method for Mode I Interlaminar Fracture Toughness of Unidirectional Fiber-reinforced Polymer Matrix Composites.* 2007.

[31] D30 Committee, "ASTM D7905/D7905M-19e1 standard test method for determination of the mode ii interlaminar fracture toughness of unidirectional fiber-reinforced polymer matrix composites," *ASTM Standard*, 2014.

[32] J. R. Reeder and J. H. Crews Jr, "Mixed-mode bending method for delamination testing," *AIAA Journal*, vol. 28, no. 7, pp. 1270–1276, 1990.

[33] J. Reeder, "An evaluation of mixed-mode delamination failure criteria," tech. rep., 1992.

[34] A. ISO, "Iso/astm 52900: 2015 additive manufacturing–general principles–terminology," *ASTM F2792-10e1*, vol. 1, pp. 1–19, 2015.

[35] M. Grasso and B. M. Colosimo, "Process defects and in situ monitoring methods in metal powder bed fusion: A review," *Measurement Science and Technology*, vol. 28, no. 4, p. 044005, 2017.

[36] A. Sola and A. Nouri, "Microstructural porosity in additive manufacturing: The formation and detection of pores in metal parts fabricated by powder bed fusion," *Journal of Advanced Manufacturing and Processing*, vol. 1, no. 3, p. e10021, 2019.

[37] P. Edwards, A. O'conner, and M. Ramulu, "Electron beam additive manufacturing of titanium components: Properties and performance," *Journal of Manufacturing Science and Engineering*, vol. 135, no. 6, 2013.

[38] K. Kempen, L. Thijs, E. Yasa, M. Badrossamay, W. Verheecke, and J.-P. Kruth, "Microstructural analysis and process optimization for selective laser melting of alsi10mg," in *Solid Freeform Fabrication Symposium Proceedings*, 2011.

[39] C. Weingarten, D. Buchbinder, N. Pirch, W. Meiners, K. Wissenbach, and R. Poprawe, "Formation and reduction of hydrogen porosity during selective laser melting of alsi10mg," *Journal of Materials Processing Technology*, vol. 221, pp. 112–120, 2015.

[40] N. Kurgan, "Effect of porosity and density on the mechanical and microstructural properties of sintered 316l stainless steel implant materials," *Materials & Design*, vol. 55, pp. 235–241, 2014.

[41] Y. M. Wang, T. Voisin, J. T. McKeown, J. Ye, N. P. Calta, Z. Li, Z. Zeng, Y. Zhang, W. Chen, T. T. Roehling, *et al.*, "Additively manufactured hierarchical stainless steels with high strength and ductility," *Nature materials*, vol. 17, no. 1, pp. 63–71, 2018.

[42] A. S. Wu, D. W. Brown, M. Kumar, G. F. Gallegos, and W. E. King, "An experimental investigation into additive manufacturing-induced residual stresses in 316l stainless steel," *Metallurgical and Materials Transactions A*, vol. 45, no. 13, pp. 6260–6270, 2014.

[43] J.-P. Kruth, G. Levy, F. Klocke, and T. Childs, "Consolidation phenomena in laser and powder-bed based layered manufacturing," *CIRP annals*, vol. 56, no. 2, pp. 730–759, 2007.

[44] A. Gilat, V.-T. Kuokkala, J. D. Seidt, and J. L. Smith, "Full-field measurement of strain and temperature in quasi-static and dynamic tensile tests on stainless steel 316l," *Procedia engineering*, vol. 207, pp. 1994–1999, 2017.

[45] B. A. Gama, S. L. Lopatnikov, and J. W. Gillespie Jr, "Hopkinson bar experimental technique: a critical review," *Appl. Mech. Rev.*, vol. 57, no. 4, pp. 223–250, 2004.

[46] A. Kidane, H. Gowtham, and N. K. Naik, "Strain rate effects in polymer matrix composites under shear loading: a critical review," *Journal of Dynamic Behavior of Materials*, vol. 3, no. 1, pp. 110–132, 2017.

[47] D30 Committee, "ASTM D6856 03: Standard Guide for Testing Fabric Reinforced Textile Composite Materials," *ASTM International, USA*, 2008.

[48] A. Gilat, R. Goldberg, and G. Roberts, "High strain rate response of epoxy in tensile and shear loading," in *Journal de Physique IV (Proceedings)*, vol. 110, pp. 123–127, EDP sciences, 2003.

[49] R. Goldberg, G. Roberts, and A. Gilat, "Anayltical modeling of the high strain rate deformation of polymer matrix composites," in *44th AIAA/ASME/ASCE/AHS/ASC Structures, Structural Dynamics, and Materials Conference*, p. 1754, 2003.

[50] R. K. Goldberg, G. D. Roberts, and A. Gilat, "Implementation of an associative flow rule including hydrostatic stress effects into the high strain rate deformation analysis of polymer matrix composites," tech. rep., 2003.

[51] A. Gilat, R. K. Goldberg, and G. D. Roberts, "Experimental study of strain-rate-dependent behavior of carbon/epoxy composite," *Composites Science and Technology*, vol. 62, no. 10-11, pp. 1469–1476, 2002.

[52] T. Vogler and S. Kyriakides, "Inelastic behavior of an as4/peek composite under combined transverse compression and shear," *Part I: experiments. International Journal of Plasticity*, vol. 15, no. 8, p. 783–806.

[53] H. Koerber, J. Xavier, and P. Camanho, "High strain rate characterisation of unidirectional carbon-epoxy im7-8552 in transverse compression and in-plane shear using digital image correlation," *Mechanics of Materials*, vol. 42, no. 11, pp. 1004–1019, 2010.

[54] J. Fitoussi, F. Meraghni, Z. Jendli, G. Hug, and D. Baptiste, "Experimental methodology for high strain-rates tensile behaviour analysis of polymer matrix composites," *Composites Science and Technology*, vol. 65, no. 14, pp. 2174–2188, 2005.

[55] H. Kolsky, "An investigation of the mechanical properties of materials at very high rates of loading," *Proceedings of the physical society. Section B*, vol. 62, no. 11, p. 676, 1949.

[56] B. Hopkinson, "X. a method of measuring the pressure produced in the detonation of high, explosives or by the impact of bullets," *Philosophical Transactions of the Royal Society of London. Series A, Containing Papers of a Mathematical or Physical Character*, vol. 213, no. 497-508, pp. 437–456, 1914.

[57] R. Davies, "A critical study of the hopkinson pressure bar," *Philosophical Transactions of the Royal Society of London. Series A, Mathematical and Physical Sciences*, vol. 240, no. 821, pp. 375–457, 1948.

[58] T. Yokoyama and K. Nakai, "Determination of the impact tensile strength of structural adhesive butt joints with a modified split hopkinson pressure bar," *International Journal of Adhesion and Adhesives*, vol. 56, pp. 13–23, 2015.

[59] K. Xia and W. Yao, "Dynamic rock tests using split hopkinson (kolsky) bar system–a review," *Journal of Rock Mechanics and Geotechnical Engineering*, vol. 7, no. 1, pp. 27–59, 2015.

[60] J. Littell, *The experimental and analytical characterization of the macrome-chanical response for triaxial braided composite materials.* The University of Akron, 2008.

[61] K. A. Brown, R. Brooks, and N. A. Warrior, "The static and high strain rate behaviour of a commingled e-glass/polypropylene woven fabric composite," *Composites Science and Technology*, vol. 70, no. 2, pp. 272–283, 2010.

[62] D30 Committee, "ASTM D5379/D5379M: Standard test method for shear properties of composites materials by the v-notched beam method," *ASTM International, West Conshohocken, PA*, 2005.

[63] D30 Committee, "ASTM D7078/D7078M-12 standard test method for shear properties of composite materials by v-notched rail shear method," *ASTM Book of Standards*, vol. i, pp. 1–15, 2012.

[64] M. Arcan, Z. Hashin, , and A. Voloshin, "A method to produce uniform plane-stress states with applications to fiber-reinforced materials," *Experimental mechanics*, vol. 18, no. 4, pp. 141–146, 1978.

[65] S.-C. Yen, J. Craddock, and K. Teh, "Evaluation of a modified arcan fixture for the in-plane shear test of materials," *Experimental techniques*, vol. 12, no. 12, pp. 22–25, 1988.

[66] I. Ud Din, P. Hao, S. Panier, K. Khan, M. Aamir, G. Franz, and K. Akhtar, "Design of a new arcan fixture for in-plane pure shear and combined normal/shear stress characterization of fiber reinforced polymer composites," *Experimental Techniques*, vol. 44, no. 2, pp. 231–240, 2020.

[67] S. Avril, M. Bonnet, A.-S. Bretelle, M. Grédiac, F. Hild, P. Ienny, F. Latourte, D. Lemosse, S. Pagano, E. Pagnacco, *et al.*, "Overview of identification methods of mechanical parameters based on full-field measurements," *Experimental Mechanics*, vol. 48, no. 4, pp. 381–402, 2008.

[68] E. M. Jones, M. A. Iadicola, *et al.*, "A good practices guide for digital image correlation," *International Digital Image Correlation Society*, vol. 10, 2018.

[69] B. Pan, K. Qian, H. Xie, and A. Asundi, "Two-dimensional digital image correlation for in-plane displacement and strain measurement: a review," *Measurement science and technology*, vol. 20, no. 6, p. 062001, 2009.

[70] P. Reu, "All about speckles: aliasing," *Experimental Techniques*, vol. 38, no. 5, pp. 1–3, 2014.

[71] P. Lava, F. Pierron, P. Reu, and L. Lamberson, "Matchid digital image correlation course-philadelphia," June 2018.

[72] P. Reu, "Virtual strain gage size study," *Experimental Techniques*, vol. 39, no. 5, pp. 1–3, 2015.

[73] B. A. Bednarcyk and M.-J. Pindera, "Inelastic response of a woven carbon/copper composite, part i: experimental characterization," *Journal of composite materials*, vol. 33, no. 19, pp. 1807–1842, 1999.

[74] B. A. Bednarcyk and M.-J. Pindera, "Inelastic response of a woven carbon/copper composite—part ii: Micromechanics model," *Journal of Composite Materials*, vol. 34, no. 4, pp. 299–331, 2000.

[75] N. Naik and V. Ganesh, "Failure behavior of plain weave fabric laminates under on-axis uniaxial tensile loading: I—analytical predictions," *Journal of Composite Materials*, vol. 30, no. 16, pp. 1779–1822, 1996.

[76] R. K. Goldberg, K. S. Carney, P. DuBois, C. Hoffarth, J. Harrington, S. Rajan, and G. Blankenhorn, "Development of an orthotropic elasto-plastic generalized composite material model suitable for impact problems," *Journal of Aerospace Engineering*, vol. 29, no. 4, p. 04015083, 2016.

[77] C. Sun and J. Chen, "A simple flow rule for characterizing nonlinear behavior of fiber composites," *Journal of Composite materials*, vol. 23, no. 10, pp. 1009–1020, 1989.

[78] A. S. Khan and S. Huang, *Continuum theory of plasticity.* John Wiley & Sons, 1995.

[79] B. Khaled, L. Shyamsunder, C. Hoffarth, S. D. Rajan, R. K. Goldberg, K. S. Carney, P. DuBois, and G. Blankenhorn, "Damage characterization of composites to support an orthotropic plasticity material model," *Journal of Composite Materials*, vol. 53, no. 7, pp. 941–967, 2019.

[80] L. Shyamsunder, B. Khaled, S. D. Rajan, and G. Blankenhorn, "Improving failure sub-models in an orthotropic plasticity-based material model," *Journal of Composite Materials*, vol. 55, no. 15, pp. 2025–2042, 2021.

[81] S. M. MEHRDAD, L. B. Lessard, and A. Golubovic, "Adhesively bonded carbon/titanium joints under in-plane and bending loads," 2007.

[82] E. Marques and L. F. da Silva, "Joint strength optimization of adhesively bonded patches," *The Journal of Adhesion*, vol. 84, no. 11, pp. 915–934, 2008.

[83] D30 Committee, "ASTM D2344/D2344M-22: Standard Test Method for Short-Beam Strength of Polymer Matrix Composite Materials," *Annual Book of ASTM Standards*, vol. 00, no. Reapproved 2006, pp. 1–8, 2011.

[84] J. Aboudi, S. M. Arnold, and B. A. Bednarcyk, *Practical micromechanics of composite materials.* Butterworth-Heinemann, 2021.

[85] P. L. Murthy, P. Naghipour Ghezeljeh, and B. A. Bednarcyk, "Development and application of a tool for optimizing composite matrix viscoplastic material parameters," tech. rep., 2018.

[86] R. Goldberg, G. Roberts, and A. Gilat, "Implementation of an associative flow rule including hydrostatic stress effects into the high strain rate deformation analysis of polymer matrix composites," *Journal of Aerospace Engineering*, vol. 18, no. 1, p. 18–27.

[87] R. K. Goldberg, G. D. Roberts, and A. Gilat, "Incorporation of mean stress effects into the micromechanical analysis of the high strain rate response of polymer matrix composites," *Composites Part B: Engineering*, vol. 34, no. 2, pp. 151–165, 2003.

[88] M. Karayaka and P. Kurath, "Deformation and failure behavior of woven composite laminates," 1994.

[89] S. Ogihara and K. L. Reifsnider, "Characterization of nonlinear behavior in woven composite laminates," *Applied composite materials*, vol. 9, no. 4, pp. 249–263, 2002.

[90] T. Belytschko and L. P. Bindeman, "Assumed strain stabilization of the eight node hexahedral element," *Computer Methods in Applied Mechanics and Engineering*, vol. 105, no. 2, pp. 225–260, 1993.

[91] L. E. Schwer, S. W. Key, T. Pucik, and L. P. Bindeman, "An assessment of the ls-dyna hourglass formulations via the 3d patch test," in *5th European LS-DYNA users conference*, 2005.

[92] M. K. Hazzard, R. S. Trask, U. Heisserer, M. Van Der Kamp, and S. R. Hallett, "Finite element modelling of dyneema® composites: from quasi-static rates to ballistic impact," *Composites Part A: Applied Science and Manufacturing*, vol. 115, pp. 31–45, 2018.

[93] K. Krishnan, S. Sockalingam, S. Bansal, and S. Rajan, "Numerical simulation of ceramic composite armor subjected to ballistic impact," *Composites Part B: Engineering*, vol. 41, no. 8, pp. 583–593, 2010.

[94] B. Wade, *Capturing the energy absorbing mechanisms of composite structures under crash loading*. PhD thesis, 2014.

[95] S. Bala and J. Day, "General guidelines for crash analysis in ls-dyna," *Livermore Software Technology Corporation*, 2012.

[96] M. P. Delaney, S. Y. Fung, and H. Kim, "Dent depth visibility versus delamination damage for impact of composite panels by tips of varying radius," *Journal of Composite Materials*, vol. 52, no. 19, pp. 2691–2705, 2018.

[97] D. Whisler and H. Kim, "Effect of impactor radius on low-velocity impact damage of glass/epoxy composites," *Journal of composite Materials*, vol. 46, no. 25, pp. 3137–3149, 2012.

[98] T. Achstetter, *Development of a Composite Material Shell-Element Model for Impact Applications*. PhD thesis, George Mason University, 2019.

[99] X. Xiao, M. E. Botkin, and N. L. Johnson, "Axial crush simulation of braided carbon tubes using mat58 in ls-dyna," *Thin-Walled Structures*, vol. 47, no. 6-7, pp. 740–749, 2009.

[100] K. Kaware and M. Kotambkar, "Effect of impactor velocity and boundary condition on low velocity impact finite element modelling of cfrp composite laminates," in *IOP Conference Series: Materials Science and Engineering*, vol. 1004, p. 012018, IOP Publishing, 2020.

[101] B. M. Khaled, "Experimental characterization and finite element modeling of composites to support a generalized orthotropic elasto-plastic damage material model for impact analysis," tech. rep., Arizona State University, 2019.

[102] R. K. Goldberg and D. C. Stouffer, "Strain rate dependent analysis of a polymer matrix composite utilizing a micromechanics approach," *Journal of composite materials*, vol. 36, no. 7, pp. 773–793, 2002.

166

[103] W. W. Feng and W. H. Yang, "General and specific quadratic yield functions," *Journal of Composites, Technology and Research*, vol. 6, no. 1, pp. 19–21, 1984.

[104] S. Kleszczynski, J. zur Jacobsmühlen, J. T. Sehrt, and G. Witt, "Error detection in laser beam melting systems by high resolution imaging," in *Proceedings of the Twenty Third Annual International Solid Freeform Fabrication Symposium*, 08 2012.

[105] B. A. Bednarcyk and S. M. Arnold, "Mac/gmc 4.0 user's manual: Keywords manual," tech. rep., 2002.

[106] K. E. Jackson, E. L. Fasanella, and J. D. Littell, "Impact testing and simulation of a sinusoid foam sandwich energy absorber," in *American Society for Composites Technical Conference*, no. NF1676L-20678, 2015.

[107] I. G. Ian Gibson, *Additive manufacturing technologies 3D printing, rapid prototyping, and direct digital manufacturing.* Springer, 2015.

[108] M. Bruyneel, "Modeling and simulating progressive failure in composite structures for automotive applications," 04 2014.

[109] A. Gilat, R. K. Goldberg, and G. D. Roberts, "Strain rate sensitivity of epoxy resin in tensile and shear loading," tech. rep., 2005.

[110] A. Matzenmiller, J. Lubliner, and R. L. Taylor, "A constitutive model for anisotropic damage in fiber-composites," *Mechanics of materials*, vol. 20, no. 2, pp. 125–152, 1995.

[111] J. Tomblin, J. Mckenna, Y. Ng, and K. S. Raju, "Advanced general aviation transport experiments: B-basis design allowables for wet layup / field repair fiber reinforced composite material systems: Agate-wp3.3-033051-115," Tech. Rep. August, 2001.

[112] J. Tomblin, J. Mckenna, Y. Ng, and K. S. Raju, "Advanced general aviation transport experiments a-basis and b-basis design allowables for epoxy-based prepreg agate-wp3.3-033051-131.," Tech. Rep. September, 2002.

[113] J. Tomblin, J. Mckenna, Y. Ng, and K. S. Raju, "Advanced general aviation transport experiments b-basis design allowables for epoxy – based prepreg agate-wp3.3-033051-095," Tech. Rep. September, 2001.

[114] W. S. Johnson, "Stress analysis of the cracked-lap-shear specimen: an astm round-robin," *Journal of testing and evaluation*, vol. 15, no. 6, pp. 303–324, 1987.

[115] G. Jing and Z. Wang, "Defects, densification mechanism and mechanical properties of 300m steel deposited by high power selective laser melting," *Additive Manufacturing*, vol. 38, p. 101831, 2021.

[116] K. Katnam, A. Comer, D. Roy, L. Da Silva, and T. Young, "Composite repair in wind turbine blades: an overview," *The Journal of Adhesion*, vol. 91, no. 1-2, pp. 113–139, 2015.

[117] A. Gilat, R. K. Goldberg, and G. D. Roberts, "Strain rate sensitivity of epoxy resin in tensile and shear loading," *Journal of Aerospace Engineering*, vol. 20, no. 2, p. 75–89.

[118] A. Gilat and J. Seidt, "Compression, tension and shear testing of fibrous composite with the split hopkinson bar technique," in *EPJ Web of Conferences*, vol. 183, p. 02006, EDP Sciences.

[119] K. Raju, S. Dandayudhapani, and C. Thorbole, "Characterization of in-plane shear properties of laminated composites at high strain rates," *Journal of aircraft*, vol. 45, no. 2, pp. 493–497, 2008.

[120] R. K. Goldberg, K. S. Carney, P. DuBois, C. Hoffarth, B. Khaled, S. Rajan, and G. Blankenhorn, "Analysis and characterization of damage using a generalized composite material model suitable for impact problems," *Journal of Aerospace Engineering*, vol. 31, no. 4, p. 04018025, 2018.

[121] O. Okoli and G. Smith, "High strain rate characterization of a glass/epoxy composite," *Journal of Composites, Technology and Research*, vol. 22, no. 1, p. 3–11.

[122] Y. Deshpande, "Quasi-static and dynamic mechanical response of t800/f3900 composite in tension and shear."

[123] V. Ganesh and N. Naik, "±45) degree off-axis tension test for shear characterization of plain weave fabric composites," *Journal of Composites, Technology and Research*, vol. 19, no. 2, p. 77–85.

[124] S.-Y. Hsu, T. Vogler, and S. Kyriakides, "Inelastic behavior of an as4/peek composite under combined transverse compressionand shear. part ii: modeling," *International Journal of Plasticity*, vol. 15, no. 8, p. 807–836.

[125] C. Hoffarth, J. Harrington, S. D. Rajan, R. K. Goldberg, K. S. Carney, and P. Dubois, "Verification and Validation of a Three-Dimensional Generalized Composite Material Model," *Proceedings of the 13th International LS-DYNA User Conference*, no. January 2015, 2015.

[126] R. Vaziri, M. D. Olson, and D. L. Anderson, "A Plasticity-Based Constitutive Model for Fibre-Reinforced Composite Laminates," *Journal of Composite Materials*, vol. 25, no. 5, pp. 512–535, 1991.

[127] S. Chaterjee, D. Adams, and D. Oplinger, "Test methods for composites: shear test methods," vol. III, no. June, p. 196, 1993.

[128] C. Hoffarth, B. Khaled, L. Shyamsunder, S. Rajan, R. Goldberg, K. S. Carney, P. DuBois, and G. Blankenhorn, "Verification and validation of a three-dimensional Orthotropic Plasticity constitutive model using a unidirectional composite," *Fibers*, vol. 5, no. 1, 2017.

[129] M. E. Foley and D. C. Hart, "Guidelines for Developing and Inserting Material Properties into the Code 65 Composite Material Database by," *Naval Surface Warfare Center Carderock Division*, no. December, 2011.

[130] S. T. Methods, "Standard Test Methods for Constituent Content of Composite Prepreg 1," vol. 97, no. December, pp. 1–6, 2010.

[131] M. H. Hassan, A. R. Othman, and S. Kamaruddin, "Void content determination of fiber reinforced polymers by acid digestion method," *Advanced Materials Research*, vol. 795, pp. 64–68, 2013.

[132] R. K. Goldberg, G. D. Roberts, and A. Gilat, "Incorporation of mean stress effects into the micromechanical analysis of the high strain rate response of polymer matrix composites," *Composites Part B: Engineering*, vol. 34, no. 2, pp. 151–165, 2003.

[133] M. May and S. R. Hallett, "Analysis of damage evolution in unidirectional carbon/epoxy samples under Shear fatigue loading," *ICCM International Conferences on Composite Materials*, no. July, 2009.

[134] J. Littell, "the Experimental and Analytical Characterization of the," 2008.

169

[135] F. Rosselli and M. H. Santare, "_ I," pp. 587–594, 1997.

[136] C. R. Siviour and J. L. Jordan, "High Strain Rate Mechanics of Polymers: A Review," *Journal of Dynamic Behavior of Materials*, vol. 2, no. 1, pp. 15–32, 2016.

[137] K. Krabbenhøft, "Basic Computational Plasticity," *Technical University of Denmark*, no. June, pp. 1–40, 2002.

[138] A. Makeev, P. Carpentier, and B. Shonkwiler, "Methods to measure interlaminar tensile modulus of composites," *Composites Part A: Applied Science and Manufacturing*, vol. 56, pp. 256–261, 2014.

[139] J. R. Xiao, B. A. Gama, and J. W. Gillespie, "Progressive Damage and Delamination in Plain Weave S-2 Glass/SC-15 Composites under Quasi-static Punch-shear Loading," *Composite Structures*, vol. 78, no. 2, pp. 182–196, 2007.

[140] B. Chandra Ray and D. Rathore, "A Review on Mechanical Behavior of FRP Composites at Different Loading Speeds," *Critical Reviews in Solid State and Materials Sciences*, vol. 40, no. 2, pp. 119–135, 2015.

[141] O. I. Okoli and G. Smith, "High strain rate characterization of a glass/epoxy composite," *Journal of Composites, Technology and Research*, vol. 22, no. 1, pp. 3–11, 2000.

[142] Y. Deshpande, *Quasi-static and Dynamic Mechanical Response of T800/F3900 Composite in Tension and Shear*. PhD thesis, The Ohio State University, 2018.

[143] V. Ganesh and N. Naik, "(±45) degree off-axis tension test for shear characterization of plain weave fabric composites," *Journal of Composites, Technology and Research*, vol. 19, no. 2, pp. 77–85, 1997.

[144] S.-Y. Hsu, T. Vogler, and S. Kyriakides, "Inelastic behavior of an as4/peek composite under combined transverse compressionand shear. part ii: Modeling," *International Journal of Plasticity*, vol. 15, no. 8, pp. 807–836, 1999.

[145] M. Javanbakht, E. Salahinejad, and M. Hadianfard, "The effect of sintering temperature on the structure and mechanical properties of medical-grade powder metallurgy stainless steels," *Powder technology*, vol. 289, pp. 37–43, 2016.

[146] N. Lavery, J. Cherry, S. Mehmood, H. Davies, B. Girling, E. Sackett, S. Brown, and J. Sienz, "Effects of hot isostatic pressing on the elastic modulus and tensile properties of 316l parts made by powder bed laser fusion," *Materials Science and Engineering: A*, vol. 693, pp. 186–213, 2017.

Appendix A

Appendix

A.1 Digital Image Correlation Setup

A.1.1 MTS Setup

It was found that turning on half press and pre-focus off produced a consistent 1 fps image trigger. Turning off half press lead to larger that 1 fps due to Esper box offset from full triggering.

A.1.2 Camera

Sony alpha6000 has multiple image resolution options: 1920 px. × 1080 px., 6000 px × 4000 px (3:2), and 6000 px. × 3376 px (16:9). In video mode, 1920 px × 1080 px, images are captured at 60 fps. In picture mode, it is recommended if storage is available to save images as RAW files and convert using Sony Imaging Edge software. JPG images get compressed so information can be lost but data size is reduced. Starting with a JPG or TIFF image from camera, the image is then pre-processed to grayscale, rotate or crop image then save as .TIFF file using MATLAB Image Processing Toolbox. This pre-processing is done to avoid issues loading images
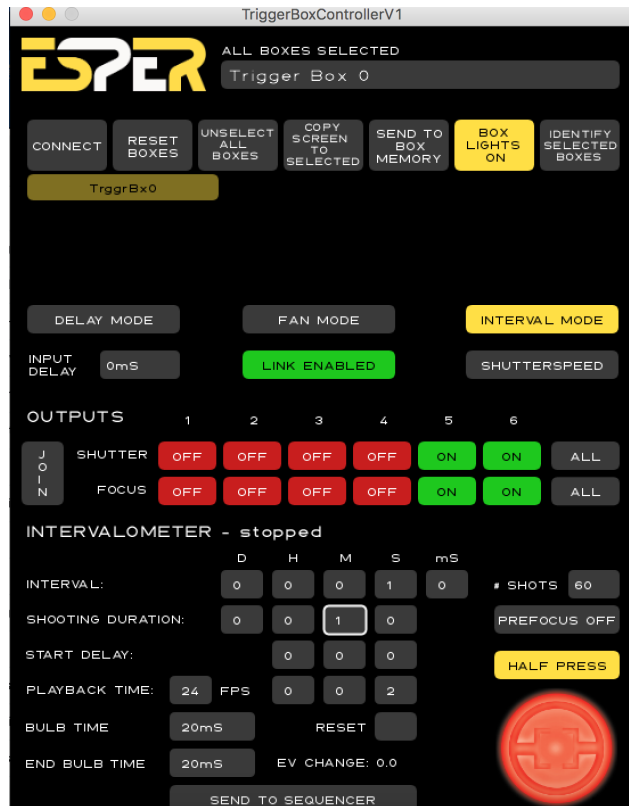
Figure A.1: Esper Triggerbox Controller Software settings for 2 output channels at 1 fps for 1 minute shooting duration.

to Vic2D. An example MATLAB code is attached below.

```matlab
1  clear; clc; close all
2  %% DIC Pre processing
3  %
4  %Read Images to grayscale, rotate, or crop then convert to .
       tiff
5  % User defined inputs
6  %
7  input_folder = 'SPECIMEN_IMAGES';
8  output_folder = 'DIC_Input';
9  output_format = '.tiff' ;%name of output file extension
10 starting_directory = pwd; %get starting directory
11 folder_list = dir(input_folder);%get directory list in input
        folder
12 folder_length = length(folder_list)-2;%note, hidden files
       might change this
13 %
14 %%
15 cd(input_folder)
16 for  k = 1:folder_length
17     folder_name = folder_list(2+k).name; %only read the
           image file,note,hidden files might change this
18     cd(folder_name)
19     specimen_folder_list = dir(pwd);%
20     specimen_folder_length = length(specimen_folder_list)-2;
21     %Make output directory for processed image with same
           folder name as
22     %input
```

174

```matlab
23         [status, msg, msgID] = mkdir(strcat(starting_directory,'
               \',output_folder,'\',folder_name,'\'));
24       for  j = 1:specimen_folder_length
25           filename = specimen_folder_list(2+j).name; %only
                  read the image file
26           [filepath,name,ext] = fileparts(filename);
27           [img,map] = imread(filename);%read image
28           img_gray = rgb2gray(img);%convert to gray scale
29           img_90 = imrotate(img_gray,90);
30 %           img_crop=imcrop(img_gray,[750,1050,4350,1700]);%
       tension region~
31 %           img_crop=imcrop(img,[2925,1900,1700,1700]);%
32           img_crop=imcrop(img_90,[1275,1235,730,4000]);%
                  Compression region~6mmx34mm
33         %            imshow(img_90)
34           picture_output = strcat(starting_directory,'\',
                  output_folder,'\',folder_name,'\',name,
                  output_format);
35           imwrite(img_90, picture_output);%save gray image to
                  new location/extnesion
36       end
37       cd ..
38   end
39   cd ..
40 %
```

A.2 Shear Fixture Drawings

B

.48

Components	Description
1	L-Clamp
2	V-Notch Specimen
3	FR4 Tabs
4	Gripping Plate

B

.38

UNLESS OTHERWISE SPECIFIED:		Contact: Javier Buenrostro

DIMENSIONS ARE IN INCHES
TOLERANCES:
FRACTIONAL ±
ANGULAR: MACH ±   BEND ±
TWO PLACE DECIMAL   ± 0.01
THREE PLACE DECIMAL   ± 0.005

jbuenros@eng.ucsd.edu

MATERIAL
Aluminum 6061-T6

TITLE:
V-Notch Shear Fixture

FINISH

COMMENTS:
Quanity: 1

SIZE **A**   DWG. NO.
Shear Fixture Assembly

REV

DO NOT SCALE DRAWING

SCALE: 1:1   WEIGHT: SHEET 1 OF 5

1.300

8.50

.75

7.00

2.80

UNLESS OTHERWISE SPECIFIED:

DIMENSIONS ARE IN INCHES
TOLERANCES:
FRACTIONAL ±
ANGULAR: MACH ±   BEND ±
TWO PLACE DECIMAL   ± 0.01
THREE PLACE DECIMAL ± 0.005

FINISH

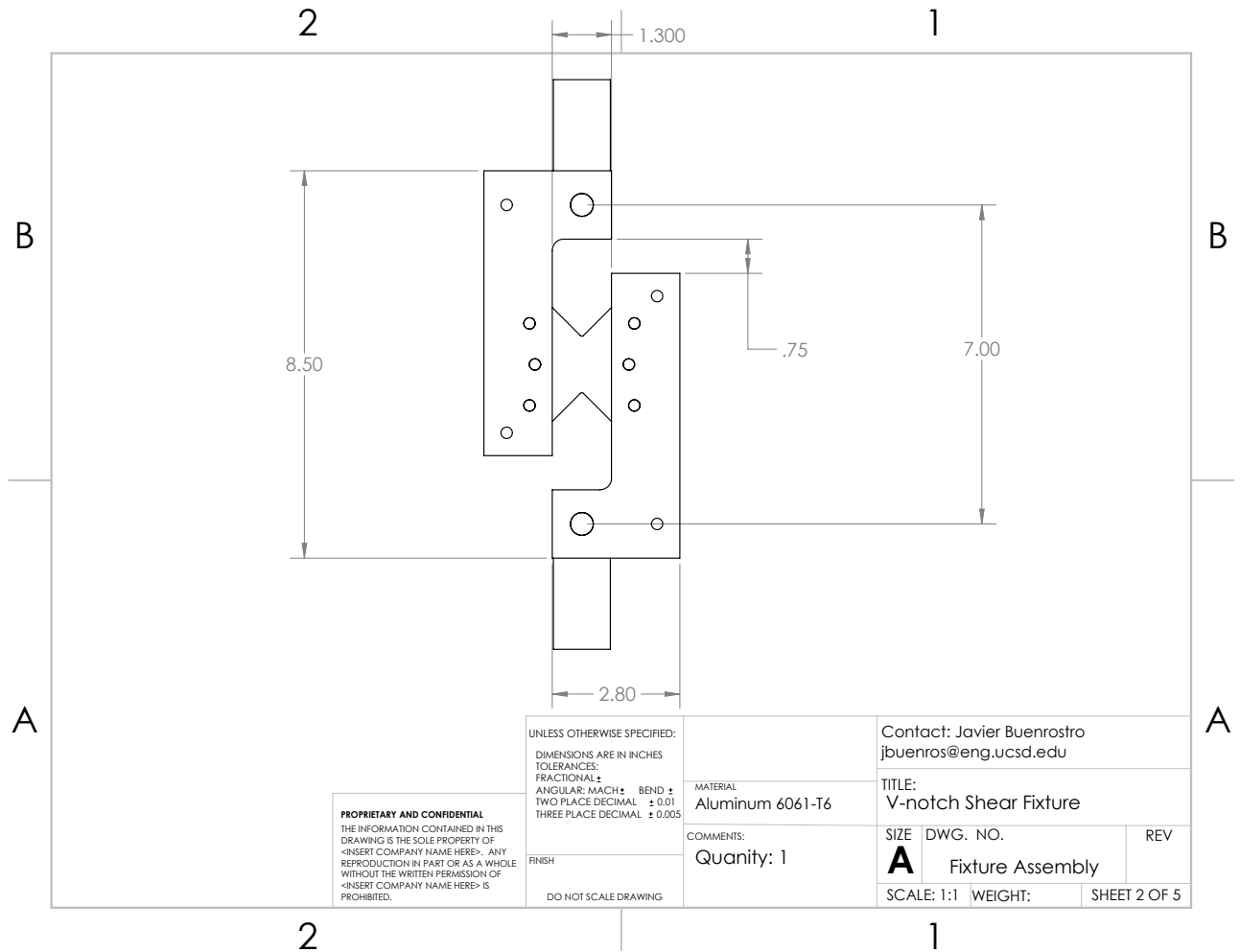DO NOT SCALE DRAWING

MATERIAL
Aluminum 6061-T6

COMMENTS:
Quanity: 1

Contact: Javier Buenrostro
jbuenros@eng.ucsd.edu

TITLE:
V-notch Shear Fixture

SIZE **A**   DWG. NO.
Fixture Assembly

REV

SCALE: 1:1   WEIGHT: SHEET 2 OF 5

Ø .251

.95

90°

B

.10

.35

.90

2.500

1.200

.90

.650

R.05

3.200

UNLESS OTHERWISE SPECIFIED:

DIMENSIONS ARE IN INCHES
TOLERANCES:
FRACTIONAL ±
ANGULAR: MACH ±   BEND ±
TWO PLACE DECIMAL   ± 0.01
THREE PLACE DECIMAL ± 0.005

MATERIAL
Aluminum 6061-T6

COMMENTS:
Quanity: 1

FINISH

DO NOT SCALE DRAWING

Contact: Javier Buenrostro
jbuenros@eng.ucsd.edu

TITLE:
V-notch Shear Fixture

SIZE DWG. NO.
A   V-notch Specimen

REV

SCALE: 1:1   WEIGHT: SHEET 3 OF 5
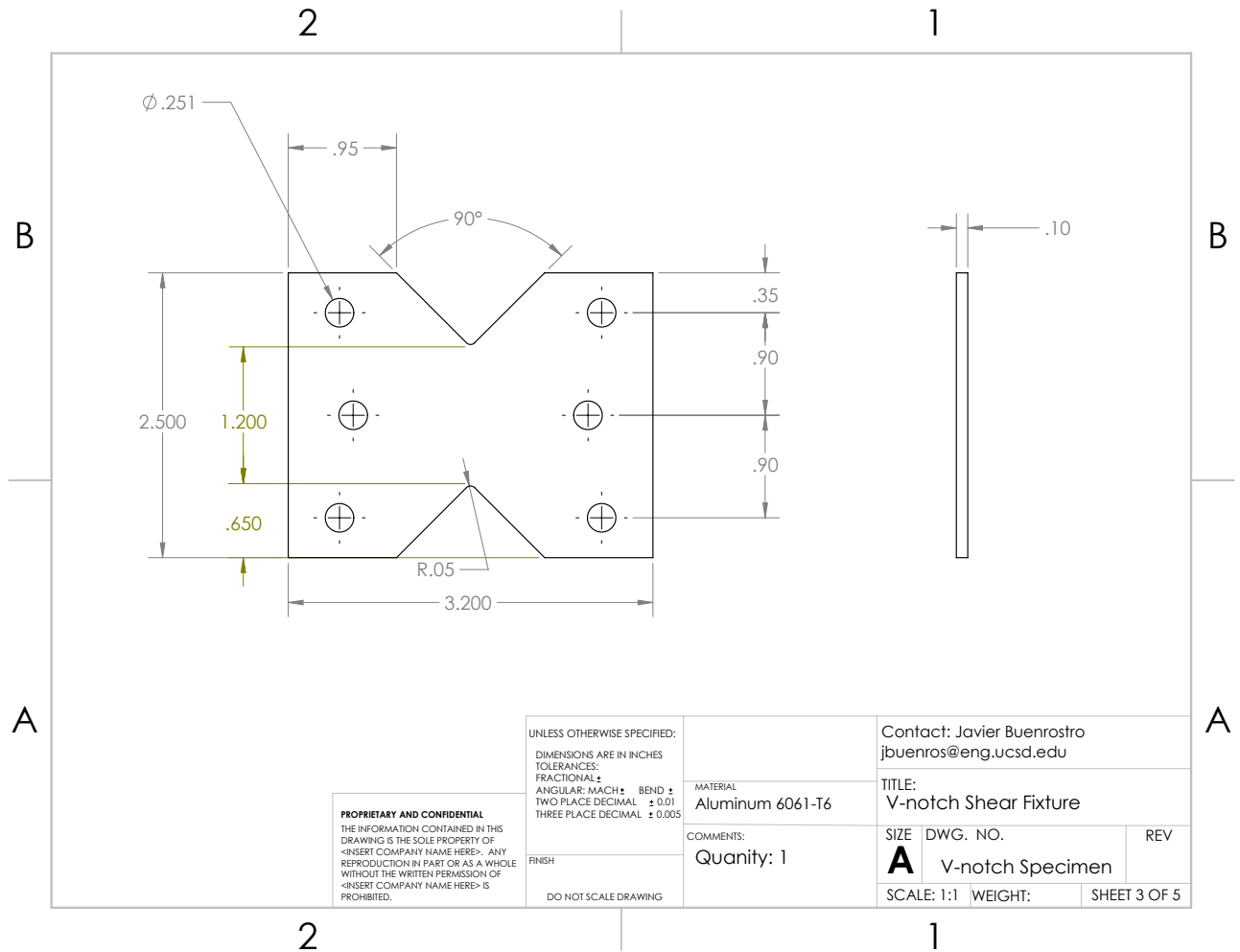
2   1

2.800

2.150

.500

Ø .5156 (33/64") THRU

.250

B   B

1.50

R.250

Ø .251 THRU

6.250   5.500

1.00

1.125

2.90

1.00

2.00

.500

1.100

.500

1.50

Note: A pair should match up perfectly

Note:
Break Corners All Edges and Holes

UNLESS OTHERWISE SPECIFIED:

DIMENSIONS ARE IN INCHES
TOLERANCES:
FRACTIONAL ±
ANGULAR: MACH±   BEND ±
TWO PLACE DECIMAL   ± 0.01
THREE PLACE DECIMAL   ± 0.005

MATERIAL

A2 Tool Steel; Fully Hardened

FINISH

DO NOT SCALE DRAWING

COMMENTS:

Quanity: 4

Contact: Javier Buenrostro
jbuenros@eng.ucsd.edu

TITLE:
V-notch Shear Fixture

SIZE	DWG. NO.		REV
A	L-Clamp		
SCALE: 1:1	WEIGHT:		SHEET 4 OF 5
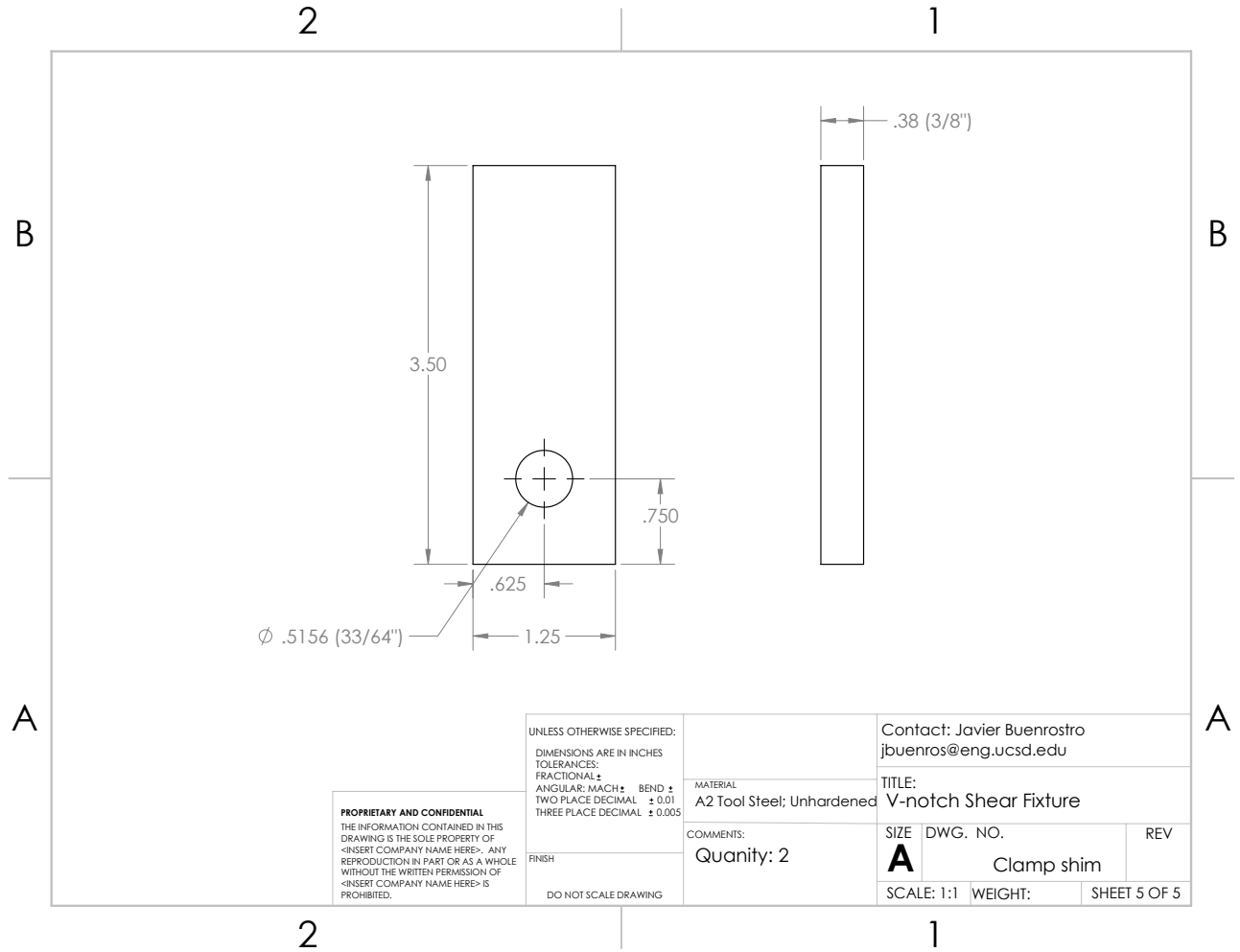
180

B   B

.38 (3/8")

3.50

.750

.625

Ø .5156 (33/64")

1.25

A   A

UNLESS OTHERWISE SPECIFIED:

DIMENSIONS ARE IN INCHES
TOLERANCES:
FRACTIONAL ±
ANGULAR: MACH ±   BEND ±
TWO PLACE DECIMAL   ± 0.01
THREE PLACE DECIMAL ± 0.005
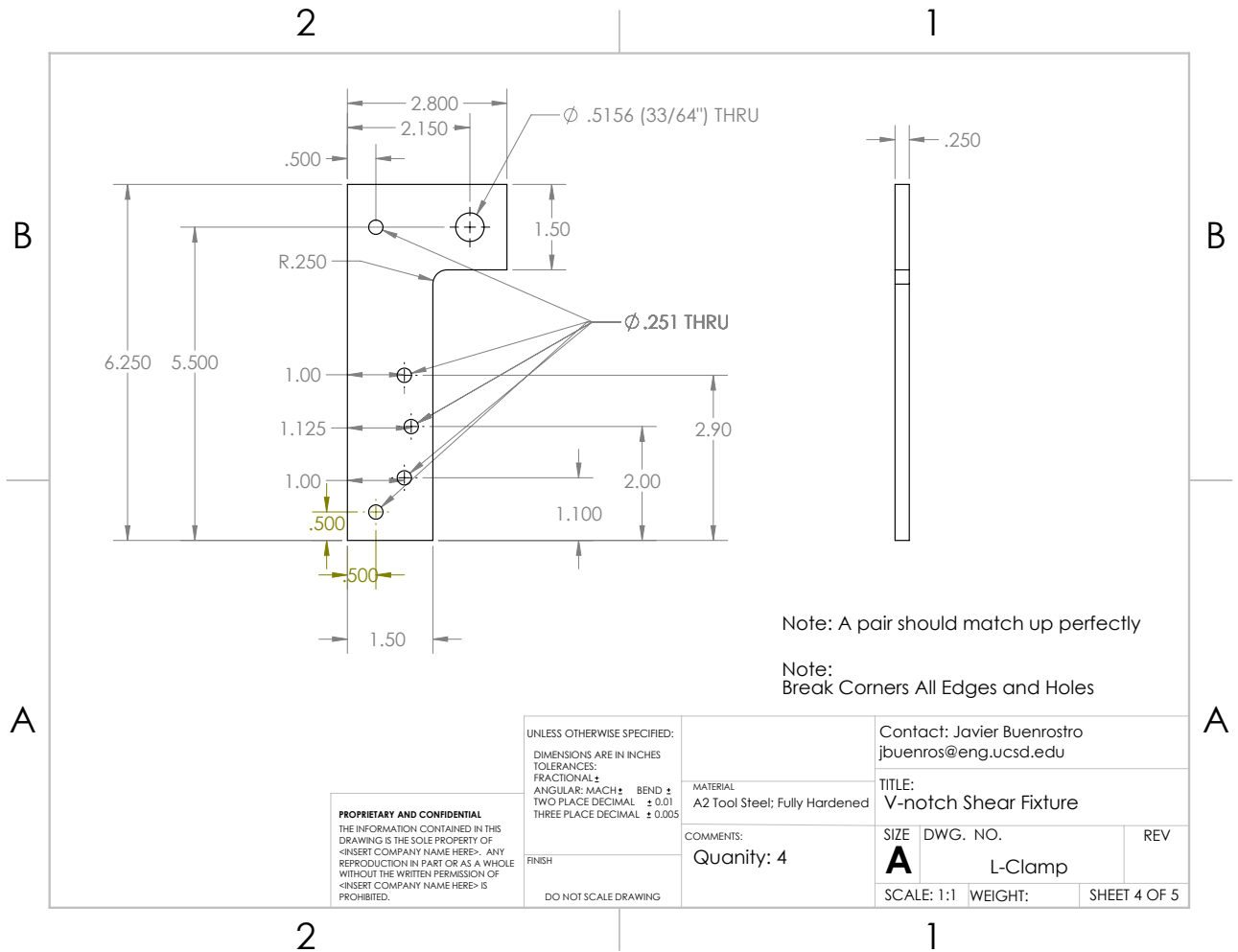
FINISH

DO NOT SCALE DRAWING

MATERIAL

A2 Tool Steel; Unhardened

COMMENTS:

Quanity: 2

Contact: Javier Buenrostro
jbuenros@eng.ucsd.edu

TITLE:

V-notch Shear Fixture

SIZE	DWG. NO.		REV
A	Clamp shim		
SCALE: 1:1	WEIGHT:	SHEET 5 OF 5	

B

B

Item	Description	Quantity
1	Circular Bar Adapter	1
2	Connecting Plate	1

A

A

UNLESS OTHERWISE SPECIFIED:

DIMENSIONS ARE IN INCHES
TOLERANCES:
FRACTIONAL ±
ANGULAR: MACH ±   BEND ±
TWO PLACE DECIMAL   ± 0.01
THREE PLACE DECIMAL ± 0.005

MATERIAL

FINISH

DO NOT SCALE DRAWING

COMMENTS:
Quanity: 1

Contact: Javier Buenrostro
jbuenros@eng.ucsd.edu

TITLE:
Shear Fixture Assembly

SIZE	DWG. NO.		REV
A			

SCALE: 1:2   WEIGHT: SHEET 1 OF 3

Top

1.25

Ø 3.00

.375

Bottom

5/8"-18 UNF ▽ .75

Front

.375

2.00

R.250

1.00

Side

1.25

.625

Ø .50 THRU ALL

.750

R.250

UNLESS OTHERWISE SPECIFIED:

DIMENSIONS ARE IN INCHES
TOLERANCES:
FRACTIONAL ±
ANGULAR: MACH ±   BEND ±
TWO PLACE DECIMAL   ± 0.01
THREE PLACE DECIMAL ± 0.005

FINISH

DO NOT SCALE DRAWING

MATERIAL
Aluminum 7075

COMMENTS:
Quanity: 1

Contact: Javier Buenrostro
jbuenros@eng.ucsd.edu

TITLE:
Connecnting Plate

SIZE | DWG. NO. | REV
A

SCALE: 1:2 | WEIGHT: | SHEET 2 OF 3

183

B B

4.00

.40

.40

2.00

.50

4X ⌀ .266 THRU ALL
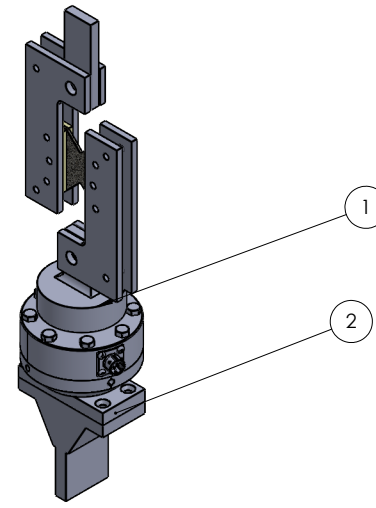⌄ ⌀ .51 X 82°

5/8''-18 UNF THRU ALL

A A

UNLESS OTHERWISE SPECIFIED:

DIMENSIONS ARE IN INCHES
TOLERANCES:
FRACTIONAL ±
ANGULAR: MACH ±   BEND ±
TWO PLACE DECIMAL   ± 0.01
THREE PLACE DECIMAL ± 0.005

MATERIAL
A2 Tool Steel

COMMENTS:
Quanity: 1

FINISH

DO NOT SCALE DRAWING

Contact: Javier Buenrostro
jbuenros@eng.ucsd.edu

TITLE:
Connecnting Plate

SIZE	DWG. NO.		REV
A			

SCALE: 1:2	WEIGHT:	SHEET 3 OF 3

184

A.3 Comparison of Polymer Matrix Plain Weave Carbon Fabric Material Properties

Table A.1: Material properties summary of 3k material from quasi-static experiments.

Manufacturing	Wet Layup [111]	Pre-Preg [113]	VARTM Experimental
E_{1T}, Warp tensile modulus, GPa	-	66.32	-
E_{1C}, Warp compressive modulus, GPa	-	54.53	55.27 ±2.14
E_{2T}, Fill tensile modulus, GPa	47.23	-	57.44 ± 1.25
E_{2C}, Fill compressive modulus, GPa	43.85	-	59.10±2.38
E_3, Through thickness modulus, GPa	-	-	-
G_{12}, In-plane shear modulus, GPa	2.34	4.27	3.35±0.33
G_{13}, Interlaminar shear modulus, GPa	-	-	2.86±0.38
G_{23}, Interlaminar shear modulus, GPa	-	-	2.58±0.30
F_1^{UT}, Warp tensile strength, GPa	-	620.18	-
F_2^{UT}, Fill tensile strength, GPa	467.67	-	791.61±12.90
F_1^{UC}, Warp compressive strength, GPa	-	477.32	489.92±30.97
F_2^{UC}, Fill compressive strength, GPa	-	-	551.98±18.07
F_{12}, In-plane shear strength, GPa	105.97	129.76	90.07±6.36
F_{13}, Interlaminar shear strength, GPa	60.6	73.63	52.65±0.54
F_{23}, Interlaminar shear strength, GPa	-	-	53.93±0.98
ν_{21}, Poisson's ratio	0.74	0.058	0.044±0.005
ν_{13}, Poisson's ratio	-	-	0.504±0.02
ν_{23}, Poisson's ratio	-	-	0.528±0.02

Table A.2: Material properties summary of 12k material from quasi-static experiments.

| Manufacturing	Pre-Preg [112]	VARTM Experimental
E_{1T}, Tensile warp modulus, GPa	56.26	51.41±1.93
E_{1C}, Compressive warp modulus, GPa	55.74	47.24±
E_{2T}, Tensile fill modulus, GPa	54.87	56.81±1.15
E_{2C}, Compressive fill modulus, GPa	53.55	51.28±
G_{12}, In-plane shear modulus, GPa	4.21	3.18±0.1
G_{13}, Interlaminar shear modulus, GPa	-	2.73±0.08
G_{23}, Interlaminar shear modulus, GPa	-	2.79±0.42
F_1^{UT}, Warp tensile strength, GPa	917.62	858.44±9.05
F_2^{UT}, Fill tensile strength, GPa	775.38	789.77±22.65
F_1^{UC}, Warp compressive strength, GPa	708.78	461.49±17.67
F_2^{UC}, Fill compressive strength, GPa	702.98	486.33±6.98
F_{12}, In-plane shear strength, GPa	132.59	77.71±4.27
F_{13}, Interlaminar shear strength, GPa	59.92	53.06±0.40
F_{23}, Interlaminar shear strength, GPa	-	54.13±0.5
ν_{21}, Poisson's ratio	-	0.0668±0.007
ν_{13}, Poisson's ratio	-	0.500±0.024
ν_{23}, Poisson's ratio	-	0.505±0.012
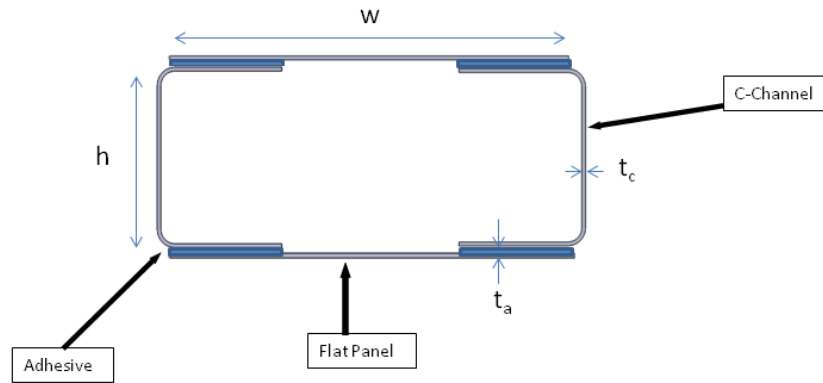
Figure A.2: Rectangular wingbox cross section

A.4   Wingbox impact experimental summary
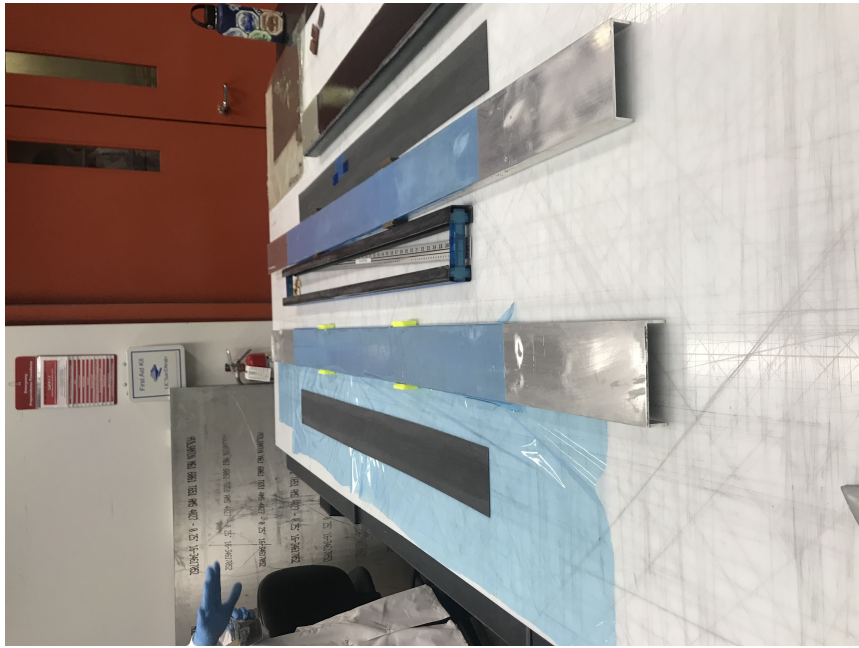
(a)
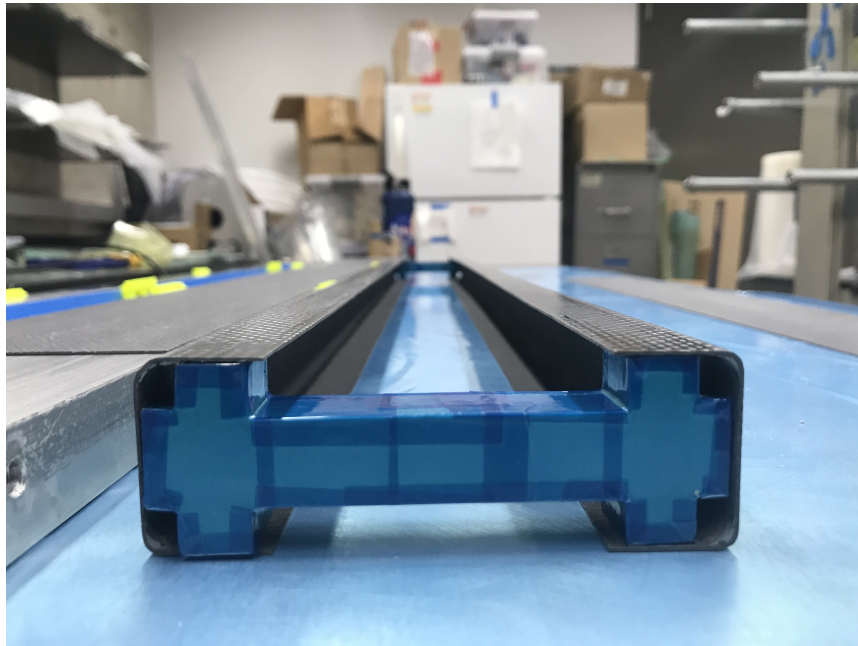
(b)

Figure A.3: Wingbox manufacturing

Table A.3: Pendulum Impact Experimental Results Summary

Specimen ID	WBIM-1	WBIM-2	WBIM-3	WBIM-4
Equivalent Mass ,kg	5.028	5.028	5.028	5.028
Theory Potential Energy, J	5	10	20	10
Theory Velocity, m/s	-1.410	-1.994	-2.821	-1.994
Photogate in-velocity, m/s	-1.347	-1.943	-2.727	-1.953
Photogate out-velocity, m/s	1.585	1.3503	1.803	1.384
Exp. Kinetic Energy, J	4.565	9.490	18.698	9.585
Peak force, kN	1.30	1.54	1.37	1.35
Exp. Change in momentum, kg m/s,	14.8	16.6	22.8	16.8
Exp. Impulse force, N sec	13.4	16.8	22.9	17.7

A.5   AM Metals Failure Parameters Summary

Table A.4: Material properties from 316L experiments

Specimen ID	Peak Force (kN)	Strength (MPa)	Failure Strain(%) Laser	Failure Strain (%) DIC
316L-R1-1-HT	17.5786	555.069	0.57607	0.59308
316L-R1-1	19.7226	622.7673	0.41473	0.41447
316L-R1-2-HT	17.5281	553.4731	0.57116	0.59102
316L-R1-2	19.7853	624.7481	0.38976	0.43804
316L-R1-3-HT	17.5153	553.0708	0.49355	0.51884
316L-R1-3	19.6625	620.8699	0.39935	0.43406
316L-R2-2	20.4428	645.5088	-	0.34208
316L-R2-3	20.5038	647.4363	-	0.33114
316L-R3-1	21.2756	671.8062	-	0.30368
316L-R3-2	21.2276	670.2922	-	0.32083
316L-R3-3	21.1338	667.3309	-	0.32807

Table A.5: Material properties from M300 experiments

Specimen ID	Peak Force (kN)	Strength (MPa)	Failure Strain(%) Laser	Failure Strain (%) DIC
M300-R1-1	43.6414	1378.0382	0.06834	0.067716
M300-R1-3	44.3375	1400.0201	0.061913	0.069027
M300-R2-1-HT	33.7203	1064.7653	-	0.092234
M300-R2-1	43.9884	1388.9967	-	0.066415
M300-R2-2-HT	33.9957	1073.4621	-	0.095606
M300-R2-2	44.5132	1405.5665	-	0.074705
M300-R2-3-HT	33.7461	1065.581	-	0.086949
M300-R2-3	44.3068	1399.051	-	0.062074
M300-R3-1-HT	34.3911	1085.9475	-	0.093922
M300-R3-1	44.7737	1413.7931	-	0.065885
M300-R3-2-HT	34.5886	1092.1836	-	0.08987
M300-R3-2	45.1213	1424.7695	-	0.065798
M300-R3-3-HT	34.3867	1085.8099	-	0.093907
M300-R3-3	45.0465	1422.405	-	0.076819